Final Report

Analysis of Polarizing Optical Systems for Digital Optical Computing with Symmetric Self Electrooptic Devices

To:

Air Force Office of Scientific Research

From:
Department of Physics
The University of Alabama in Huntsville

Principal Investigator
Dr. Russell A. Chipman

Investigator
J. Larry Pezzaniti

Contract # AFOSR-89-0542

November 4, 1991

REPORT DOCUMENTATION PAGE

Form Approved
OMB No. 0704-0188

1. AGENCY USE ONLY (Leave blank)	2. REPORT DATE	3. REPORT TYPE AND DATES COVERED
	11/4/91	Final 9/1/89-9/30/91

4. TITLE AND SUBTITLE
Analysis of Polarizing Optical Systems for Digital Optical Computing with Symmetric Self Electrooptic Devices

5. FUNDING NUMBERS
2305/B1

6. AUTHOR(S)
Russell Atwood Chipman, Joseph Larry Pezzaniti

7. PERFORMING ORGANIZATION NAME(S) AND ADDRESS(ES)
Polarization & Lens Design Laboratory
University of Alabama in Huntsville

8. PERFORMING ORGANIZATION REPORT NUMBER
AFOSR-TR- 92 0003

9. SPONSORING/MONITORING AGENCY NAME(S) AND ADDRESS(ES)
AFOSR/NE
Building 410
Bolling AFB, DC 20332-6448
Alan Craig

10. SPONSORING/MONITORING AGENCY REPORT NUMBER
AFOSR-89-0543

11. SUPPLEMENTARY NOTES

91-18894

12a. DISTRIBUTION/AVAILABILITY STATEME
Unlimited

12b. DISTRIBUTION CODE

13. ABSTRACT (Maximum 200 words)

This research developed imaging polarimetry to study the propagation of polarized light in polarization based optical interconnects such as the AT&T digital optical computer, and adapted polarization aberration theory and polarization ray tracing, to understand new classes of problems arising in optical systems for digital optical computing.

An imaging polarimeter was constructed and calibrated at UAH under this contract. The output is a Mueller matrix image, a spatial representation of the polarization properties across a wavefront, typically as a function of field of view or pupil coordinate. With the imaging polarimeter, one can simultaneously balance the transmitted polarization between the top and bottom, left and right sides of a wavefront as one rotates tilts, or otherwise adjusts the polarization components. Imaging polarimeter was demonstrated to be a useful alignment tool and was used to characterize many polarizing elements such as polarizing beam splitters, linear retarders, and liquid crystals.
SEE ATTACHED SHEET.

91 1223 125

14. SUBJECT TERMS	15. NUMBER OF PAGES
Polarimetry, polarization, digital optical computing, optical interconnects	76
	16. PRICE CODE

17. SECURITY CLASSIFICATION OF REPORT	18. SECURITY CLASSIFICATION OF THIS PAGE	19. SECURITY CLASSIFICATION OF ABSTRACT	20. LIMITATION OF ABSTRACT
unclass	unclass	unclass	UL

Polarization analysis was performed on AT&T photonic switching network, iteration 3, and several improvements to its existing design were discovered. We discovered that replacing several linear retarders with circular retarders improved the off axis performance.

A high precision single channel polarimeter was constructed to supplement data obtained from the imaging polarimeter.

Executive Summary

The Executive Summary provides a brief synopsis of the contents of AFOSR Final Report, **Analysis of Polarizing Optical Systems for Digital Optical Computing with Symmetric Self Electrooptic Devices**, contract #AFOSR-89-0542.

This research was motivated by the need to develop appropriate metrology to study the propagation of polarized light in optical interconnects such as the AT&T digital optical computer architectures, and to adapt polarization aberration theory and polarization ray tracing, to understand new classes of problems arising in optical systems for digital optical computing.

An imaging polarimeter has been built and calibrated at UAH under this contract. This imaging polarimeter measures polarization properties of a set of ray paths through optical systems and subsystems. The output is a Mueller matrix image, a spatial representation of the polarization properties across a wavefront, typically as a function of field of view or pupil coordinate. The imaging polarimeter provides performance measures of polarization components. Because it provides polarization images over a wavefront, the imaging polarimeter presents an unprecedented view of what occurs during the alignment of optical and polarization components. With an imaging polarimeter, one can simultaneously balance the transmitted polarization between the top and bottom, left and right sides of a wavefront as one rotates, tilts, or otherwise adjusts polarization components. Using this technique, 0.1° alignment error in a quarterwave retarder has been resolved. Phase measuring interferometry in real time had a similar impact on optical alignment. Appendix A contains a paper, "Imaging polarimeters for optical system metrology," which details the construction and operation of the imaging polarimeter.

The most important study performed under this contract with the imaging polarimeter was a comparison between commercially available polarizing beam splitters, specifically to determine their suitability for optical interconnects. Large differences in performance were observed between polarizing beam splitters; most of the cubes polarizing properties were surprisingly poor. Appendix B, a copy of a paper submitted to Applied Optics, summarizes this effort.

A polarized spherical wave exiting a polarizing beamsplitter has an orientation of linear polarization which rotates from top to bottom, a form of polarization aberration. This polarization aberration has been carefully documented, experimentally and theoretically. The variation of orientation of linear polarization results when the angle of incidence lies outside the normal plane (the plane containing the face normals and interface normal, usually a horizontal plane when incident and exiting beams are parallel to an optical table). Figure 1, on the next page, shows the polarization aberration of a horizontally polarized spherical wave focused through a polarizing beam splitter. A fraction of each ray incident out of the normal plane is reflected, due to the rotation of the plane of incidence rays within the spherical wave make with the beam splitting interface, causing a rotation of the linear polarization direction.

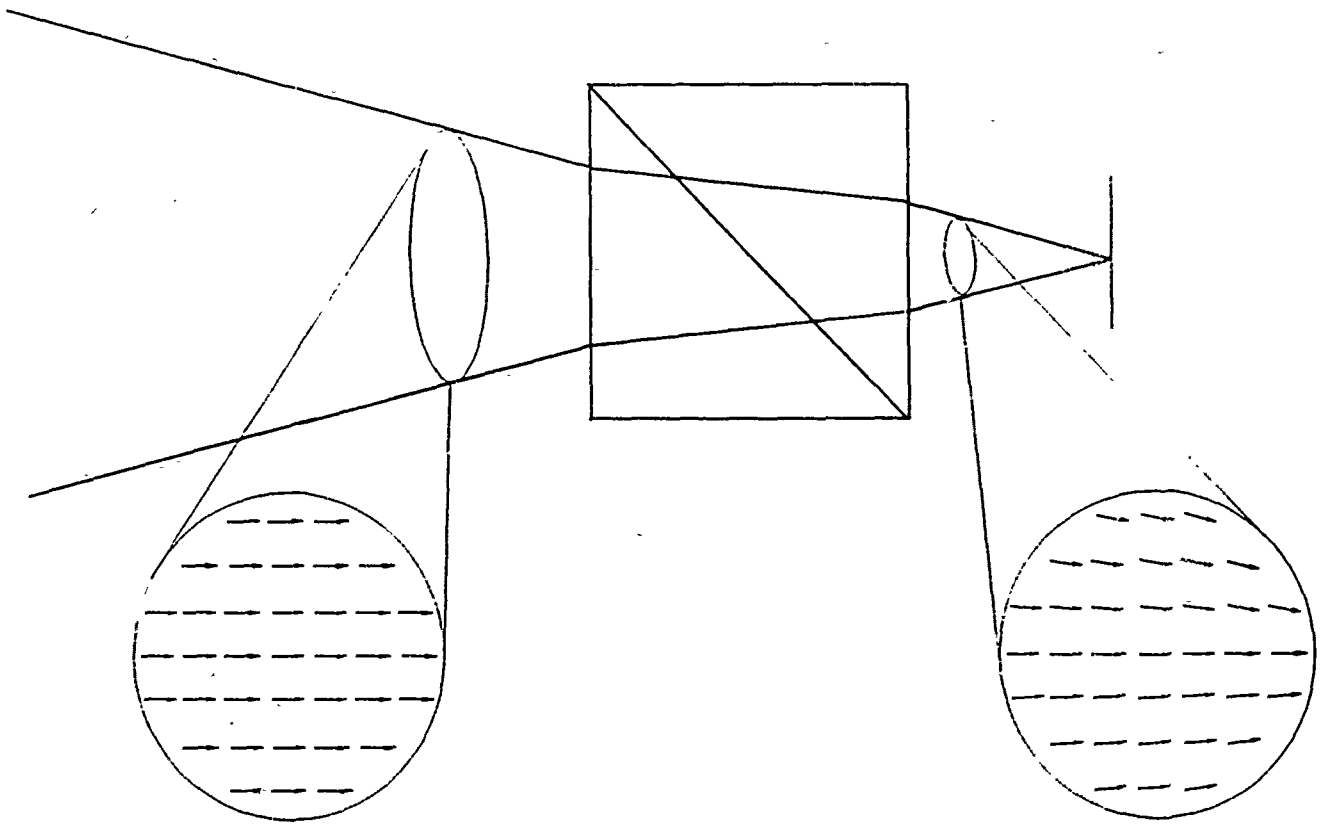

1a 1b.

Figure 1 Polarization aberration introduced into a converging spherical wavefront transmitted through an ideal polarizing beam splitter. A uniform horizontally polarized (within the plane of the page) spherical wave is incident. The transmission axis of the polarizing beam splitter cube is aligned with the p direction a ray makes with the beam splitting interface which varies with ray angle of incidence, causing apodization and a spatially varying orientation of linear polarization in the transmitted wavefront. The polarization of the incident spherical wave is illustrated in Figure 1a and the transmitted wavefront is shown in Figure 1b.

Figure 2 shows how a polarizing beam splitter situated between image planes at infinite conjugate, similar to many optical interconnects configurations, introduces a non-uniformity of intensity in the image plane and a spatial variation of linear polarization across and image. Polarization non-uniformity in the image can reduce the efficiency and throughput of optical interconnects, giving rise to extraneous beams at successive polarization beam splitters. The spatial variation of linear polarization states must be compensated for to allow efficient transmission or reflection at subsequent polarizing beam splitters.

Our analysis of iteration 3, the latest iteration, of the AT&T Photonic Switching Network, uncovered ways to improve the efficiency of polarization optical interconnects. This study proceeds from the supposition that polarizing beam splitters provide the most efficient four port access to the s-SEED, an assumption supported by research described in References [11][12][13][14]. A polarizing beam splitter cube has a spatially varying orientation of linear polarization eigenstates. The goal of this research was to choose polarizing elements and to position them to transform the polarization state of the beams into the correct orientations of linear polarization to match the polarization eigenstate directions at each polarizing beam splitter cube. Existing architectures utilize quarter wave retarders to do this. The design is successful for beams that propagate within the normal plane of the polarizing beam splitter. Outside the normal plane, however, the beams are not rotated into the correct linear polarization state to align with polarization eigenstate directions at the polarizing beam splitter. The misorientation of the linear polarization to the polarization eigenstate directions of the polarizing beam splitter cubes causes a fraction of the beams to be routed incorrectly. Our research shows that at certain locations in the optical interconnect, the linear quarterwave retarder can be replaced with a circular quarterwave retarder to manipulate the linear polarization directions of the beams to align with the polarization eigenstate directions of the polarizing beam splitters. We have suggested replacing several quarterwave linear retarders with circular retarders and have suggested that half wave retarders be inserted in certain locations to manipulate the polarization aberration so that it increases the efficiency of the optical interconnects for beams out of the normal plane.

Two configurations of a polarization beam combining module, one of the principle configurations for polarization based optical interconnects, are shown in Figures 3 and 4. The existing configuration, shown in Figure 3, utilizes a quarterwave retarder, QWR2, in double pass to convert the linearly polarized light transmitted by the polarizing beam splitter (horizontal) into linearly polarized light which will be reflected by the polarizing beam splitter (vertical). The orientation of linear polarization after the second pass through QWR2 does not match the polarization eigenstate directions of the polarizing beam splitter for reflection, compare Figures 3,II and 3,V. The polarizing beam combining module shown in Figure 4 utilizes a circular retarder, CR1, in place of QWR2, resulting in a spatially varying polarization eigenstates which match the polarization eigenstate directions of the polarizing beam splitter cube, increasing the efficiency of the polarizing beam combining module. Circular retarders, rather than linear retarders, help keep light in the correct eigenstates, and minimize losses.

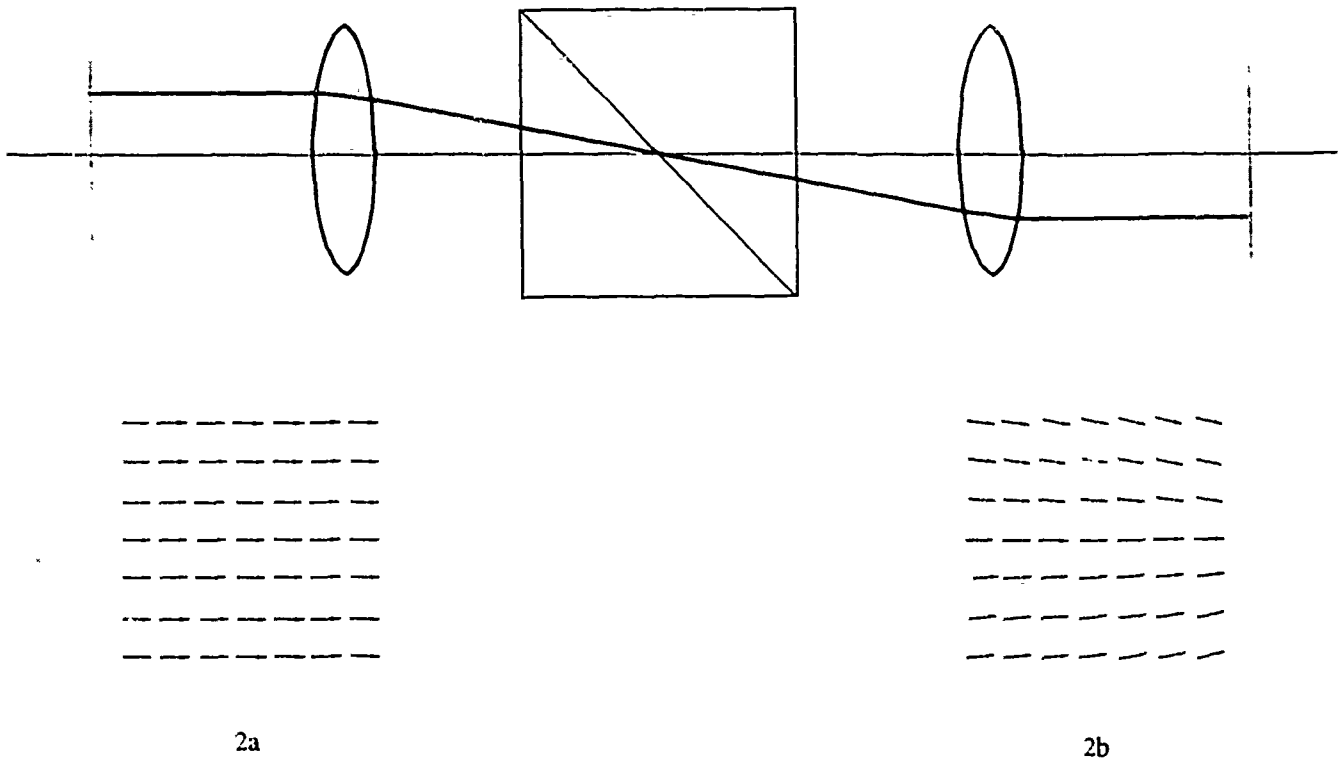

2a

2b

Figure 2 Polarization variation and intensity non-uniformity introduced into an image by an ideal polarizing beam splitter. An ideal polarizing beam splitter is situated in collimated space between conjugate image planes. The intensity non-uniformity and polarization variation of the image is due to the varying orientation of p direction each object beam encounters at the beamsplitting interface. The object polarization directions are shown in Figure 2a and the image polarization directions are shown in Figure 2b.

Beam Combining Module

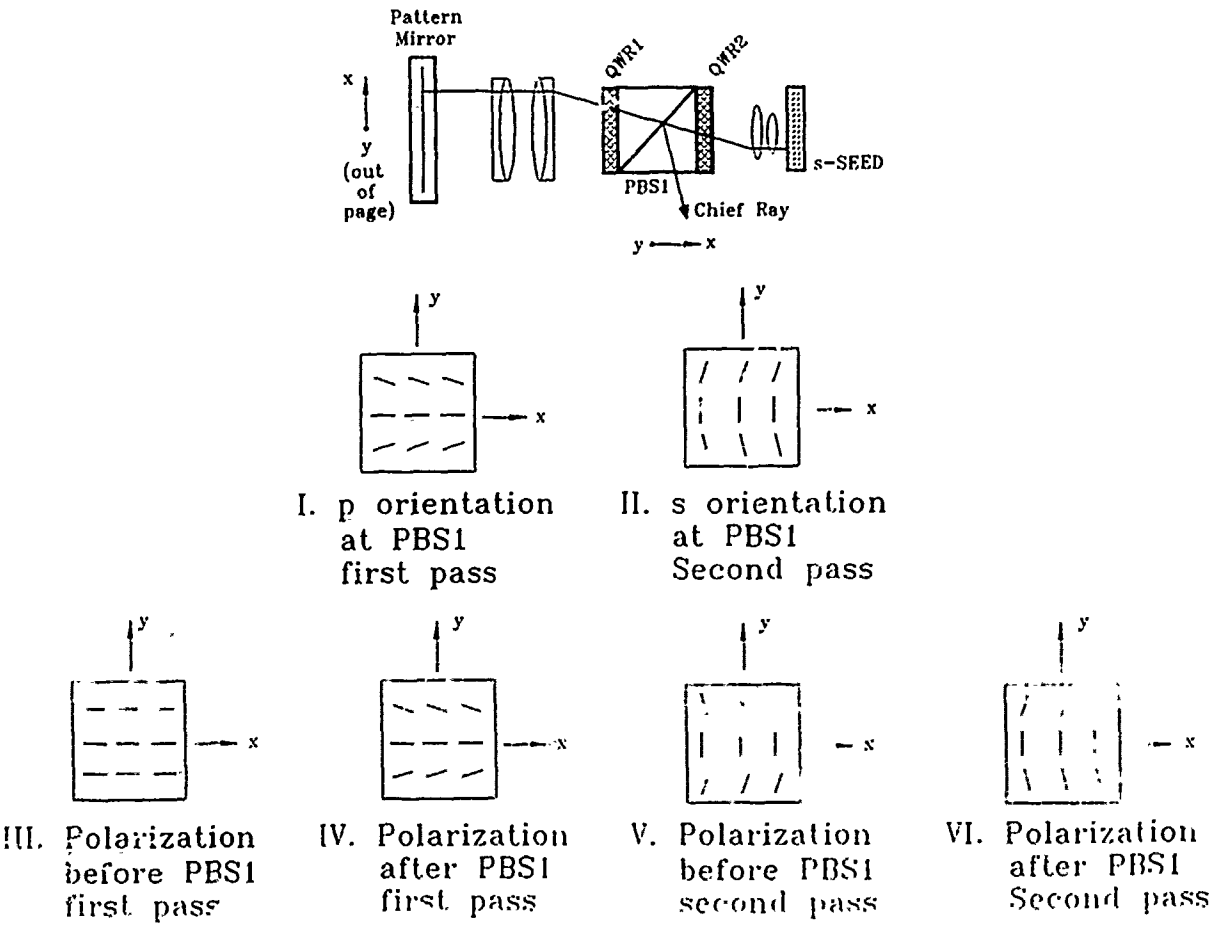

Figure 3 Graphical polarization analysis of a polarizing beam combining module which utilizes a polarizing beam splitter and a quarterwave linear retarder. Figure I illustrates the eigenpolarization directions of the polarizing beam splitter cube in transmission, and Figure II shows the eigenpolarization directions in reflection. Figures III through VI illustrate the polarization changes before and after transmission or reflection from the polarizing beam splitter. The role of the quarterwave retarder in this configuration is to rotate the orientation of linear polarization of the beams transmitted from the polarizing beam splitter, depicted in Figure IV, into the eigenpolarization directions of PBS1 in reflection, illustrated in Figure II. The quarterwave retarder does not rotate the object beams polarization directions, for which y=0, into the correct orientation, causing a fraction of the beams to be reflected by PBS1 in second pass.

Beam Combining Module

(Design Altered)

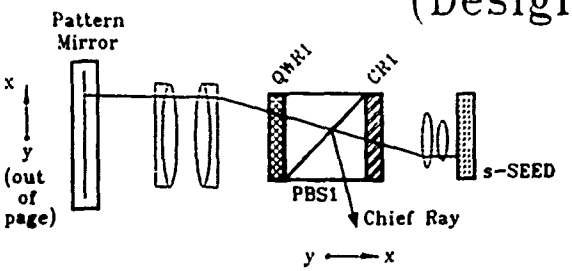

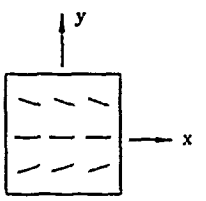

I. p orientation at PBS1 first pass

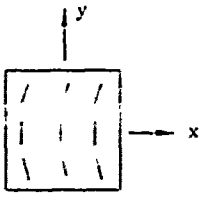

II. s orientation at PBS1 Second pass

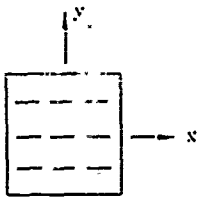

III. Polarization before PBS1 first pass

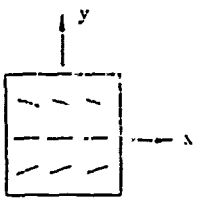

IV. Polarization after PBS1 first pass

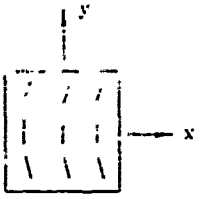

V. Polarization before PBS1 second pass

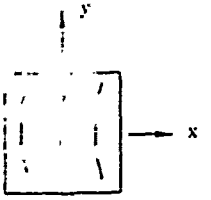

VI. Polarization after PBS1 Second pass

Figure 4 Graphical polarization analysis of a polarizing beam combining module which utilizes a polarizing beam splitter and a circular retarder. Figure I illustrates the eigenpolarization directions of the polarizing beam splitter cube in transmission, and Figure II shows the eigenpolarization directions in reflection. Figures III through VI illustrate the polarization changes before and after transmission or reflection from the polarizing beam splitter. The role of the circular retarder in this configuration is also to rotate the orientation of linear polarization of the beams transmitted from the polarizing beam splitter, depicted in Figure IV, into the eigenpolarization directions of PBS1 in reflection, illustrated in Figure II. The circular retarder rotates all the object beams polarization into the correct eigenpolarization directions of PBS1 in reflection, allowing all the energy to be reflected by PBS1 in second pass.

We will continue to develop general design strategies to boost the performance of various optical interconnects based on polarization beam combining. From the polarization modeling we would like to develop further the formalism to analyze a broader class of polarization based optical interconnect architectures. The unique nature of these systems require novel analysis methods. From the analysis studies, a set of design rules for implementing polarizing optics in polarization based optical interconnects will be developed. Effective use of these polarization configurations requires tools like the imaging polarimeter for alignment.

A highly accurate single channel polarimeter has been constructed to make high precision polarization measurements of thin films liquid crystals, uniaxial and bi-axial crystals and polarizers. The single channel polarimeter will measure depolarization, the polarization scrambling of light, diattenuation, retardance and complete Mueller matrices of samples with a single beam. The single channel polarimeter will also be used to calibrate polarizing optics for the Imaging polarimeter.

Error analysis due to polarimeter misalignment and retardance error in the polarizing elements has been included in the data reduction algorithms. Errors in the retardance and orientation of the retarders in the Imaging Polarimeter produce large errors in the measured Mueller matrix. For example, misorientation of 1° in a retarder can produce a 30% error in one of the Mueller matrix elements. The data reduction algorithms include error correction terms to compensate for these errors.

More work is needed to increase the accuracy of the imaging polarimeter. Presently, the accuracy is limited by the 8-bit A-D conversion of the ccd detector. We plan to increase the accuracy of the imaging polarimeter by upgrading to a scientific grade Photometrics ccd detector array with 12-bit A-D conversion. The upgrade will increase the accuracy by a factor of ten, allowing the verification of polarization aberration theories, measurement of small polarization effects such as depolarization, and accurate measurement of several interesting and scientifically valuable samples, optical systems and subsystems.

Table of Contents

List of Figures

1. Background on Digital Optical Computers

The research described in this report involves the polarization analysis and metrology of polarization based optical interconnects, the foundation of an architectural approach to optical computing pursued by AT&T Bell Labs. AT&T optical computing designs make use of 2-D arrays of SEED modulators interconnected in free space. SEEDs and related electrooptic devices have been proposed as potential components of free space digital optical computers because of their bistability, high speed, and low switching power.[1-5] SEEDs or self electrooptic effect devices exploit the quantum confined Stark effect in quantum well materials to produce optical bistability.[6,7] One version, the symmetric SEED or s-SEED, contains two SEEDs connected together across a fixed voltage, Figure 1 [8]. In this configuration, the s-SEED is optically bistable with two states, (1) SEED 1 is highly reflecting and SEED 2 is poorly reflecting, and (2) SEED 1 is poorly reflecting and SEED 2 is highly reflecting. The device has time sequential gain, such that the state of the device can be set with low power beams, and read out subsequently with high power beams. Because the device operates on the ratio of reflectances, it is insensitive to optical power supply fluctuations if both beams are derived from a single source. The s-SEED is especially promising for digital optical computing applications because it has good input/output isolation being time sequential. It does not require the critical biasing required of most bistable devices.

Spatial light modulators, optical dynamic memory[5], all-optical shift registers[9], and optical set-reset latches have been demonstrated using arrays of s-SEEDs[10]. Optical systems which compute or perform interconnections using arrays of s-SEEDs have been proposed and are under construction[11-12]. The focus of our studies have been on massively parallel optical processors constructed from interconnected or cascaded optical logic modules (COLM). This method of interconnection is based on the use polarizing elements and lenses. The polarization/lens based system allows efficient interconnections between devices.[11] These COLMs can be interconnected to form gates, adders, programmable logic arrays, and other components of conventional electronic computers. Figure 2 is a schematic of a single COLM. The section of the COLM shown separately in Figure 3, is used to clear the s-SEED array. The COLM reads out the s-SEED array, operates on the information, and passes data to another COLM, where another s-SEED array is set. This system has been constructed at AT&T Bell Laboratories. Operational

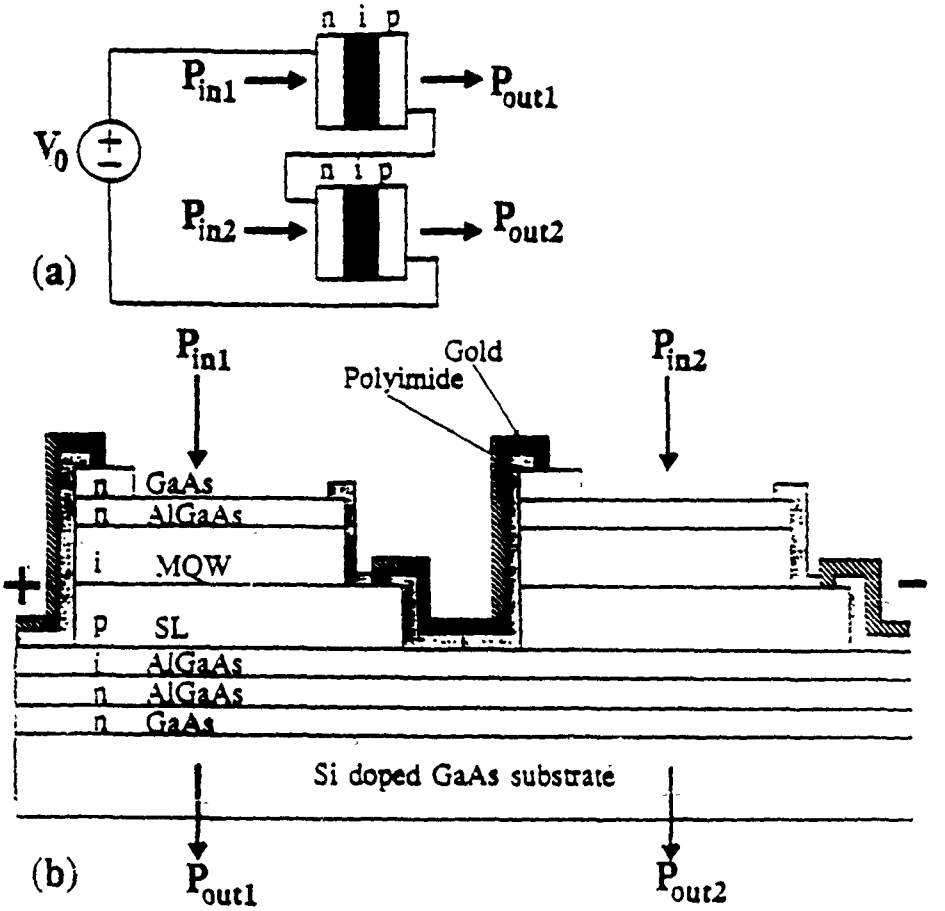

Figure 1 : Structure of symmetric self-electro-optic device.

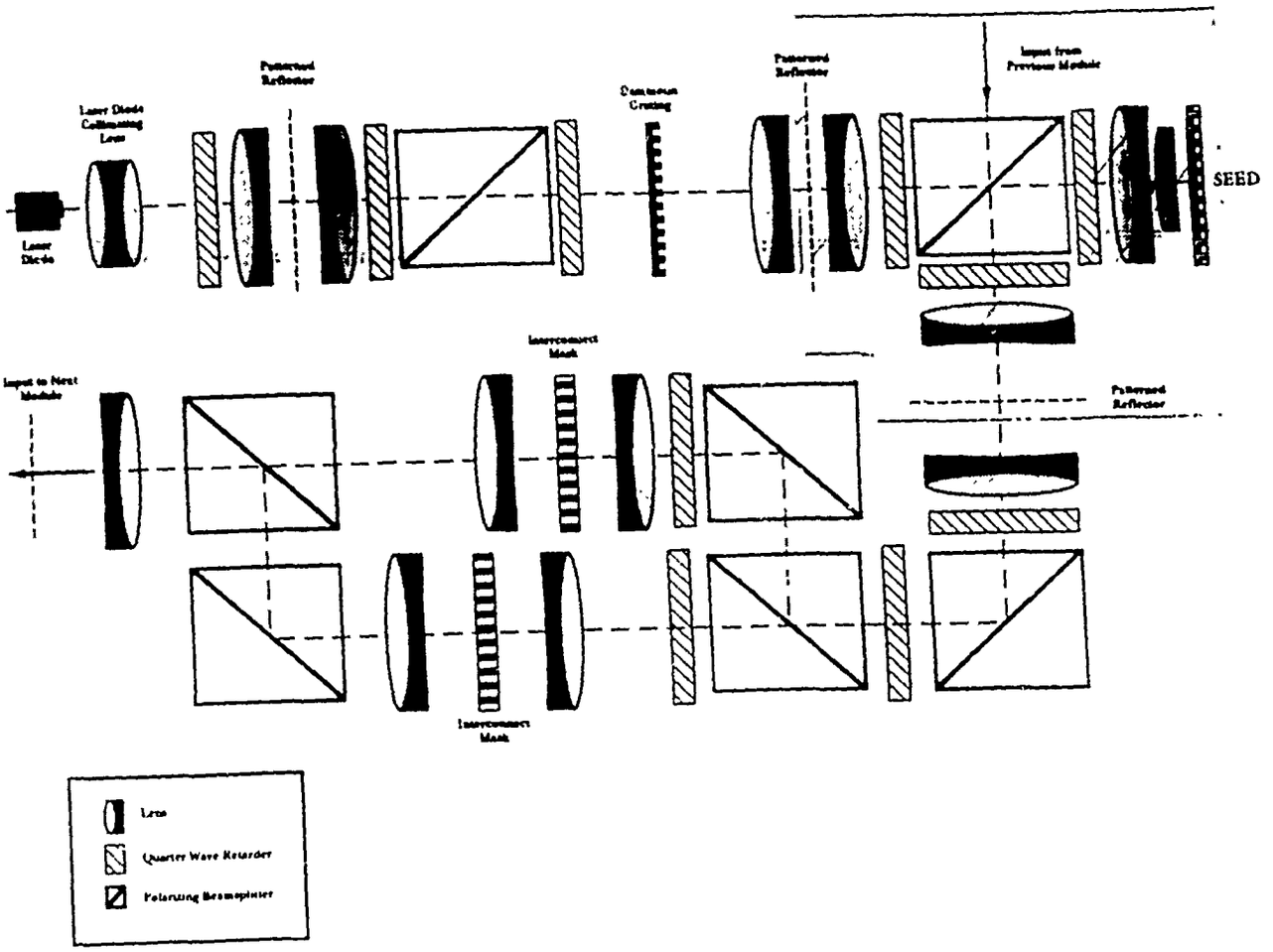

Figure 2 : Architecture of a cascadable optical logic device for a digital optical computer.

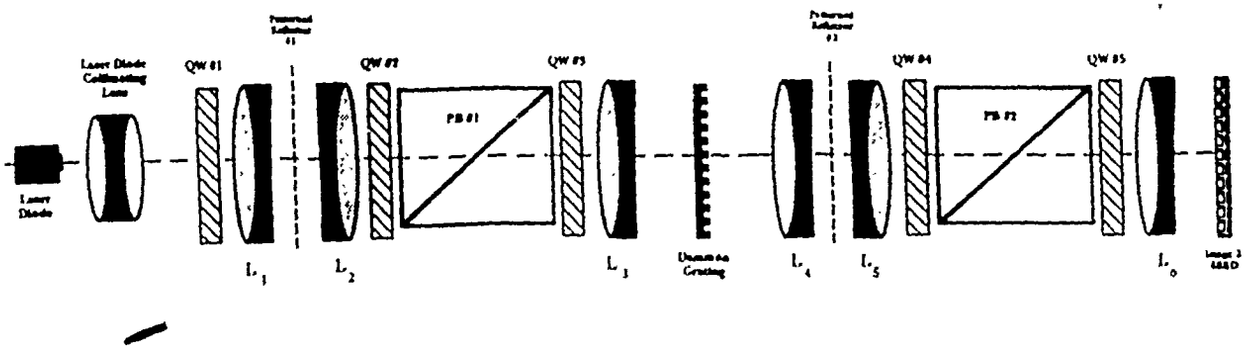

Figure 3 : Portion of the cascadable optical logic module that is used to clear the s-SEED.

details of this optical system are available in References 13,14.

The Cascadable Optical Logic Module depends on the control of polarized light for its operation. If careful control of polarization is not maintained, separate beams will not be properly combined and the computer becomes unreliable. The optical interconnects have large numbers of retarders and polarizing beamsplitters to permit separate beams carrying digital information to be combined and address the appropriate quantum wells on the s-SEED.

Polarization based optical interconnect architectures suffer from substantial amounts of instrumental polarization, the polarization properties associated with ray paths through the system. The polarizing beams splitters are responsible for the majority of the instrumental polarization. This research includes studies done on polarizing beam splitter cube properties to understand how they contribute to instrumental polarization. Two properties of polarizing beam splitters contribute significant instrumental polarization: (1) the polarizing beam splitter cube beamsplitting interface often displays strong angular dependence of s and p transmittance and reflectance, (2) the angular orientation, relative to a global coordinate system, of the s and p directions (linear polarization directions) depends on ray angle of incidence. The first property, the angular dependence of s and p transmittance and reflectance, can be optimized with multilayer design techniques.[15,16] The second property is due to the geometry of the cube. The polarizing axes of the polarizing beam splitter are aligned with the p direction a ray makes with the beamsplitting interface in transmission, and the s direction in reflection. The angular orientations of s and p, however, depend on the angle of incidence of the ray, causing a angular nonuniformity of linear polarization direction. Analysis and measurements made with the Imaging Polarimeter on polarizing beam splitters are detailed in "Angular dependence of Polarizing beam splitters," submitted to Applied Optics, attached to the end of this report.

Quarterwave retarders were analyzed and measured with the Imaging properties. Quartz zero order quarter wave retarders display a much larger angular bandwidth than the polarizing beam splitters. However, several properties can degrade their performance, such as crystal axis misorientation, thickness variations, and misalignment of the fast axis in the optical system.

The first half of this report analyzes optical interconnect architectures, and suggestions for improvements to existing architectures. The second part describes the instrumentation developed for metrology of polarizing optical systems, and measurements.

Sections 2.1 and 2.2 provides polarization analysis on the polarizing components of polarization based optical interconnects. Section 2.3 models the polarizing properties of Iteration 3 Photonic Switching Network, and makes several suggestions to improve its off axis efficiency.

The major thrust of this research has been in the development of polarimetric instrumentation to measure the polarizing properties of polarization based imaging systems. The motivation for the development of this instrumentation was the need for a metrology tool to study the large instrumental polarization of polarization based optical interconnects. Before this research, the needed instrumentation did not exist. Section 3 describes the Mueller Matrix Imaging Polarimeter, built and calibrated under this contract, which measures polarization for a set of ray paths through an optical system, i.e., it measures the Mueller matrix of the system as a function of object or pupil coordinate. The Mueller matrix provides information about the diattenuation and retardance over the pupil or field of view.

Section 4 introduces a closely related instrument, also developed under this contract, a Stokes Imaging Polarimeter which measures polarization properties across a wavefront. The output of this instrument supplements information about a wavefront obtainable by from interferometry (wavefront error), it measures the polarization content of a wavefront. Both interments are configured to operate at 633nm and 850nm, the operating wavelength of s-SEED's.

A third instrument was developed to support the first two, a single channel polarimeter. The function of this polarimeter is to align the polarizing optics of the Mueller matrix imaging polarimeter and the Stokes imaging polarimeter. Section 5 provides a brief description of single channel polarimeter and describes the alignment procedure for the polarizing optics.

Section 6 discusses the calibration issues involved in building the imaging polarimeters. Finally concluding remarks are provided in Section 7.

2. Polarization Modeling of Polarization Based Optical Interconnects

This section develops the field of view polarization properties of a single module of the AT&T Iteration 3 Photonic Switching Network. First we describe the angular polarization behavior of the polarizing elements, the polarizing beam splitters and the quarterwave retarders. Next we formulate a polarization model of a single stage of the Photonic Switching Network, and make suggestions to improve its efficiency. The analytical approach used here can be applied to other AT&T polarization based optical interconnects.

2.1 Field of view effects of the polarizing beam splitters

This section describes the field of view properties of polarizing beam splitter cubes. The work presented here helps develop the polarization analysis of the Photonic Switching Network in Section 2.3. A more thorough treatment of polarizing beam splitters, along with measurements made with the Imaging Polarimeter are given in "Angular dependence of polarizing beam splitter cubes," submitted to Applied Optics, in Appendix B.

An ideal polarizing beam splitter cube divides the incident light into s and p polarization states, transmitting the p polarized component and reflecting the s polarized component. Polarizing beam splitters have a limited range of angle of incidence and wavelength for which they are effective. Polarizing beam slitters sold through catalogs are optimized to provide a large spectral range within a small angular field of view. Optical computing architectures typically require the opposite, i.e., a wide field of view with quasimonochromatic light.

The angular performance of the polarizing beam splitter depends on two factors:

1. The transmittance and reflectance of s and p polarization states,
2. The dependence of s and p angular orientations on angle of incidence.

Research has been done to increase the angular range for which p transmittance and s reflectance remain high.[15,16] AT&T Laboratories has designed a polarizing beam splitter to provide a ±7° FOV. Tests performed at AT&T and at UAH agree with predictions of the design. UAH measurements on the AT&T polarizing beam splitter, along with measurements on three other commercially available polarizing beam splitters are presented in the above referenced paper.

The geometry of the polarizing beam splitter causes a spatially varying orientation of

linear polarization in transmitted and reflected wavefronts. The orientation of linear polarization transmitted from a polarizing beam splitter is dependent on the ray angle of incidence. For a spherical wave of unpolarized light is incident on a polarizing beam splitter, the reflected and transmitted beams have a spatially varying linear polarization. Since the orientation of the plane of incidence a ray makes with the beamsplitting interface depends on the angle at which the ray is incident i.e., the s and p directions depend on ray angle of incidence. Since the orientation of linear polarization of a polarizing beam splitter aligns with the p direction in transmission and the s direction in reflection, the orientation of linear polarization of a polarizing beam splitter is a function of ray angle of incidence. Figure 4 introduces a coordinate system for describing polarizing beam splitter cubes. The origin is centered on the entrance face with the z axis normal to the face. The beam splitting interface normal lies in the x-z plane and is 45° from the z axis. The direction of an incident ray is specified by its direction cosines (l, m, n) where $l = \cos\alpha$, $m = \cos\beta$ and $n = \cos\gamma$ and $l^2 + m^2 + n^2 = 1$. α, β, and γ are illustrated in Figure 4. For incident rays with $\beta = 90°$, the p direction is parallel to the x-z plane (we will refer to this as the horizontal plane) and the s direction aligns with the y-z plane (vertical). For angles of incidence in which $\beta > 90°$, the p plane rotates counterclockwise with the respect to the horizontal, while for $\beta < 90°$ it rotates clockwise. Figure 5 illustrates the orientation of s and p directions as functions of the direction cosines of the incident rays. In Figure 5, α increases from 90° in the positive x direction and β increases from 90° in the positive y direction. The thin cross hairs are parallel with the horizontal and vertical planes (x-z and y-z planes in Figure 4). The large circles indicate the zones where the angles of incidence are $\gamma = 5°$ and $\gamma = 10°$. The angle ϕ is the angle between the p direction and the horizontal x-z plane.

In Section 2.3 we explore how the variation of orientation of linear polarization degrades the performance of an optical interconnect. Methods to correct the degradation of the Photonic Switching Network off axis efficiency caused by this effect are described.

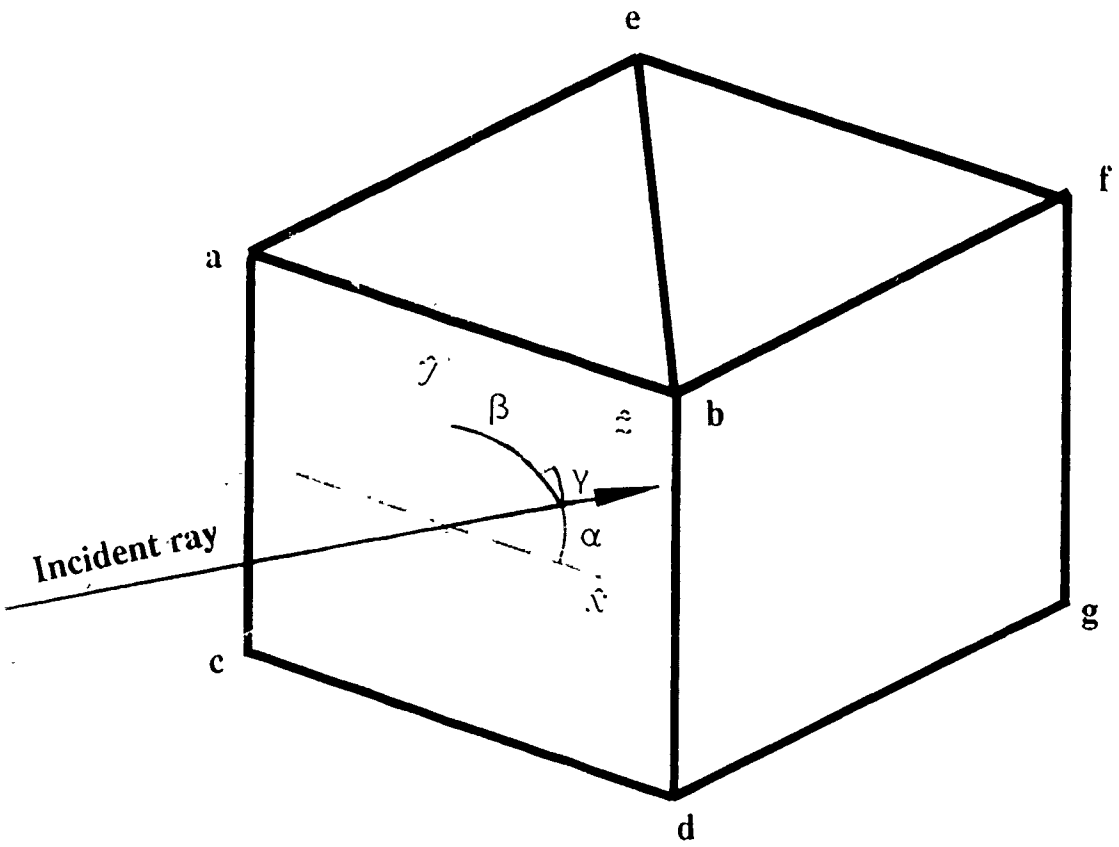

Figure 4 Geometry of a polarizing beam splitter. Side (a,b,c,d) is the entrance face. (a,e,g,d) is the beam splitting interface. The transmitted beam exits the face (f,e,g) while the reflected light exits at (b,e,g,c). An incident ray is identified by its direction cosines (l, m, n) defined as $l = \cos\alpha$, $m = \cos\beta$, and $n = \cos\gamma$. α is the angle between the x axis and the ray. β btween the y axis and the ray, γ between the z axis and the ray. We refer to the x-z plane as the horizontal and the y-z plane is vertical. The origin of the x-y-z coordinate system is located at the center of the entrance face. The cube is placed in the imaging polarimeter with the horizontal plane parallel to the table top.

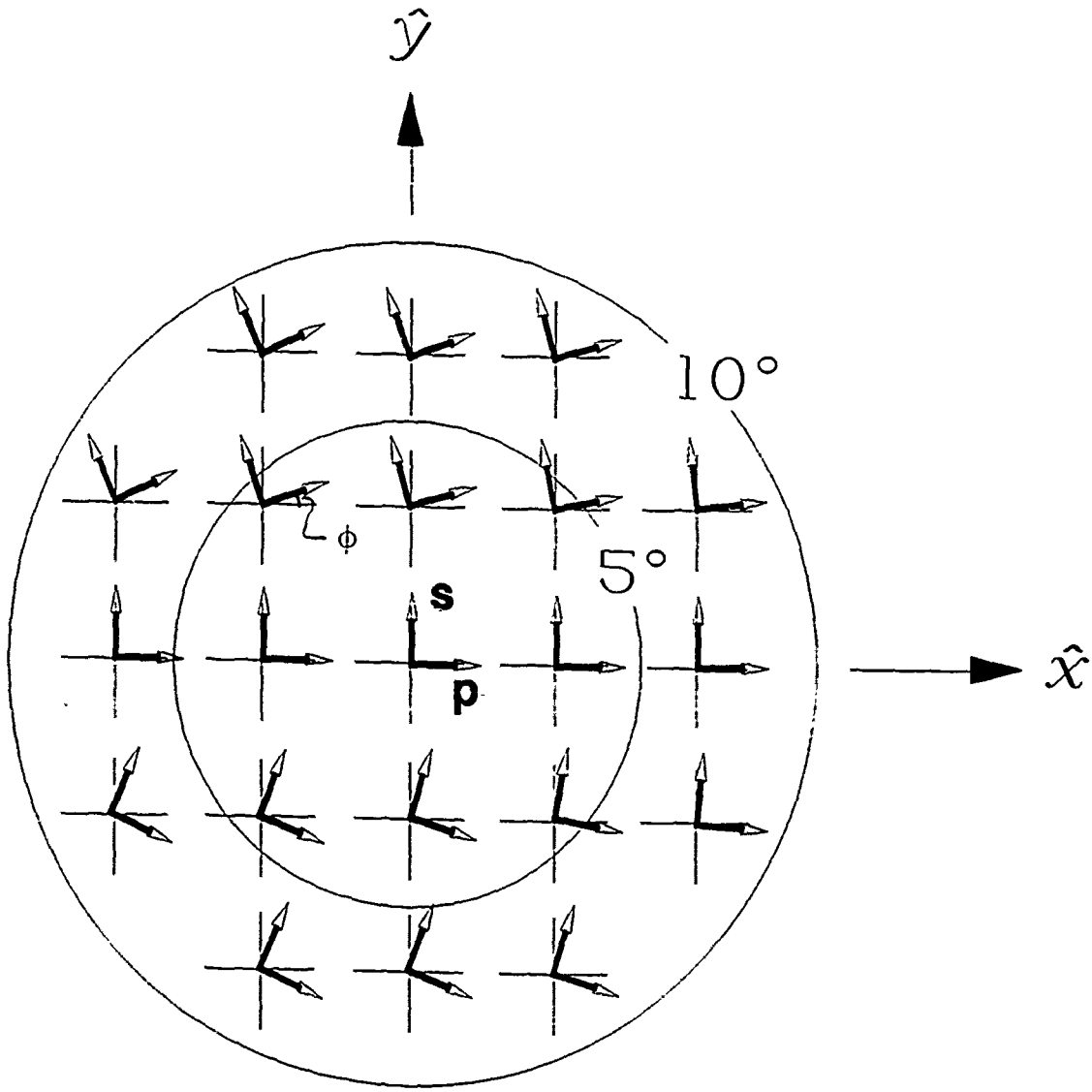

Figure 5 Orientation of the s and p directions on the beamsplitting interface of a polarizing beam splitter plotted as a function of beam angle of incidence on the cube face. The orientation of the beam splitting interface is shown in Figure 1. Figures 1 and 2 share the same coordinate system. α increases from 90° in the positive x direction. β increases from 90° in the positive y, and the large circles indicate the zones where the angles of incidence are $\gamma = 5°$ and $\gamma = 10°$. Incident rays for which $\beta > 90°$ involve a counterclockwise rotation of s-p coordinates and rays in which $\beta < 90°$ the rotation is clockwise. The polarizing axis is parallel to the p direction in transmission and the s direction in reflection. Polarizing beam splitters have a spatially varying orientation of linear polarization.

2.1.1 Throughput of a COLM as a function of transmittance and reflectance from the polarizing beam splitters

Figure 6 is a plot of the fraction of light transmitted through a Cascadable Optical Logic Module as a function of the transmittance of the polarizing beam splitters (reflectance of the polarizing beam splitters are assumed to be 1). For this analysis, the transmittance of each of the polarizing beam splitters varies by the same amount. The light is transmitted through polarizing beam splitters 4 times and reflects 6 times (see Figure 2). The efficiency of the COLM strongly depends on the transmittance of the polarizing beam splitters. If the transmittance of the polarizing beam splitters is reduced to 75%, the efficiency of the COLM is reduced by a half. The dependence is nearly exponential.

Figure 7 shows the fraction of light transmitted through a Cascadable Optical Logic Module as a function of the reflectance of the polarizing beam splitter cubes while the transmittances are held fixed at 1. The COLM throughput is more sensitive to variation of reflectance of the polarizing beam splitters than transmittance because more reflections occur. If the reflectance of the polarizing beam splitters is reduced to 75%, the efficiency of the COLM approaches 0.

The energy lost takes the wrong direction at the polarizing beam splitters, the beams are transmitted when they should reflect or the beams are reflected when they should be transmitted.

2.2 Field of view effects of the retarders

Several characteristics of birefringent retarders introduce polarization aberration in polarization critical systems. First, the thickness of the birefringent material may be wrong or wedged, yielding an incorrect or spatially varying retardance. The crystal axis can be misoriented relative to the faces or the mount. The retarder can be misaligned in the optical system, either tilted or with its fast axis at the wrong orientation.

Three other problems with retarders are more fundamental, angular field dependence, diattenuation, and birefraction.

The angular dependence of a uniaxial crystal is illustrated in Figure 8. For a crystal axis in this orientation, two effects influence its retardance. First, the difference between the extraordinary and ordinary refractive index, or birefringence, decreases quadratically with increasing field angle. This property decreases the amount of retardance the crystal displays. The second effect increases tends to offset the first effect somewhat. This effect

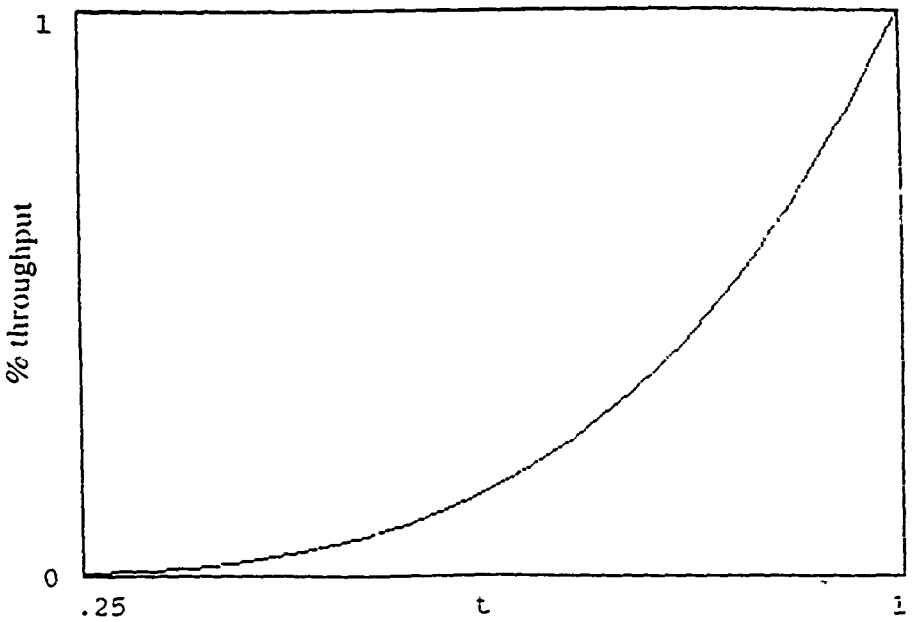

Figure 6 Fraction of transmitted light through a Cascaddable Optical Logic Module, plotted as a function of the transmission coefficients of the polarizing beam splitter cubes. The transmission coefficients of the each of the polarizing beam splitters were varied by the same amount, while the reflection coefficients were held at 1.

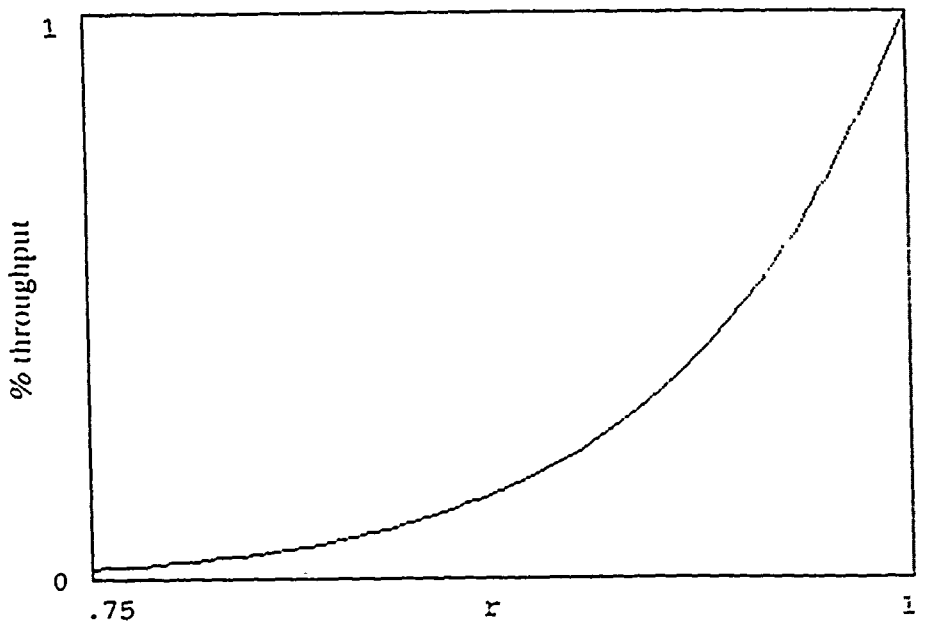

Figure 7 Fraction of transmitted light through a Cascaddable Optical Logic Module. plotted as a function of the reflection coefficients of the polarizing beam splitter cubes. The reflection coefficients of the each of the polarizing beam splitters were varied by the same amount, while the transmission coefficients were held at 1.

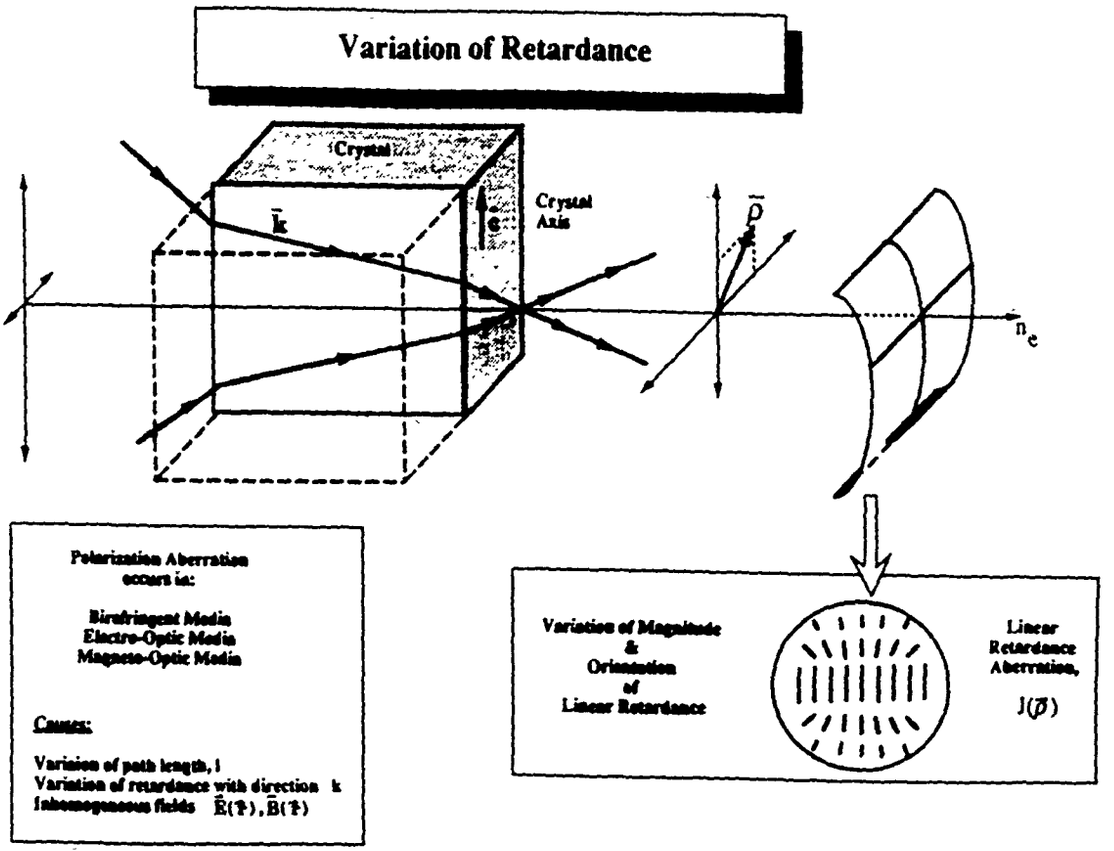

Figure 8 Variation of retardance in a uniaxial crystal. The birefringence varies with angle of incidence according to the index ellipsoid. The retardance varies because of the change in the birefringence and the varying path length with angle of incidence. The magnitude and orientation of linear retardance varies quadratically with angle of incidence.

increases the retardance simply due to the increase in the physical path length with angle.

Figure 9 shows the variation in retardance with field angle in quartz linear retarder. The crystal axis is aligned to the $\hat{y}$ axis. Shown is one quadrant with the lower left corresponding to a ray at normal incidence, and the angle of incidence increasing along the $\hat{x}$ and $\hat{y}$ axes. By symmetry, it is only necessary to view the angular dependence in one quadrant. For an ideal quarter wave retarder, about a 1% variation of retardance is found over a 10 degree field of view. The field of view dependence of quartz quarter wave retarders should not contribute significant errors into AT&T digital optical computing architectures.

Figure 10 contains a plot of the Mueller matrix as a function of angle of incidence, taken with the UAH Imaging Polarimeter over a ±6° FOV, of a visible zero-order quartz quarter wave retarder at 633nm. Each of the Mueller matrix elements are shown and labeled except m_{11}, since we normalize by m_{11} (see Section 3.2). The data of interest lie in the central circular portions. The center of each of the plots represents an axial ray, and the angle of incidence increases in the radial direction out to 6° in each direction. The retarder displays a uniform retardance, within 1%, over the 6° field of view.

2.2.1 Orientation error in the quarter wave retarders

An analytical study has been done to determine the loss of efficiency of the COLM due to misorientation of the quarter wave retarders. Figure 11 shows the percent transmission of light that remains in the correct polarization state as a function of orientation error of the quarter wave retarders. Each retarder received the same amount of orientation error. The percent transmission refers to the percentage of light emitted from the laser diodes that travels through the entire COLM to the next COLM, assuming ideal quarterwave retarders and polarizing beam splitter cubes.

2.3 Polarization analysis of Iteration 3 Photonic Switching Network

Iteration 3 Photonic switching Network utilizes a polarization based imaging system to interconnect 2-D arrays of optical logic devices. It uses polarizing beam splitters, quarter wave retarders and patterned reflectors to interlace input beams onto a modulator and separate output beams reflected from the modulators. Each beam must pass through

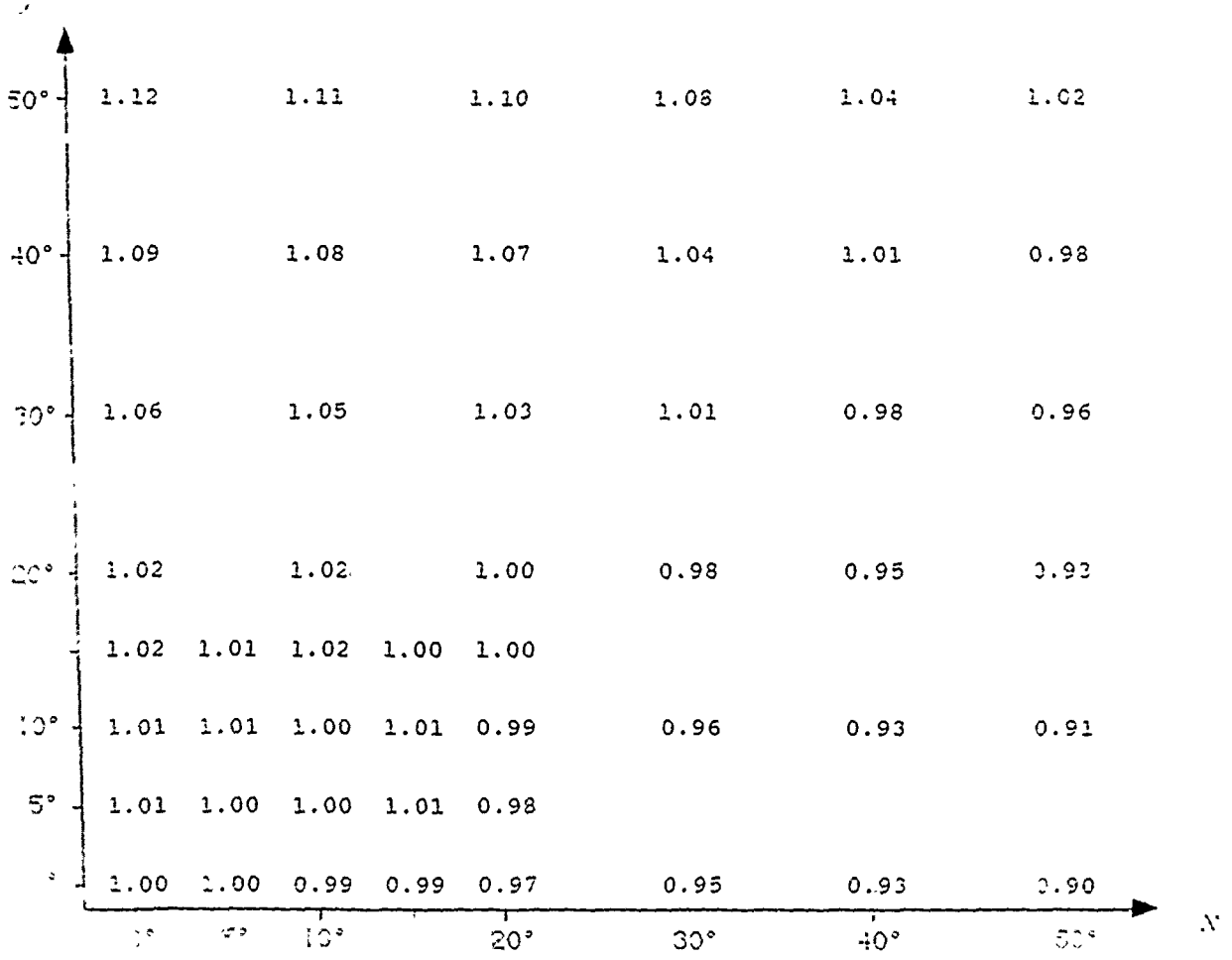

Figure 9 Variation of retardance of a quartz quarter wave retarder. The crystal axis is aligned with the y axis. At 0° angle of incidence the retardance is a quarter wave. The variation of retardance is less than 1% over a ±10° FOV.

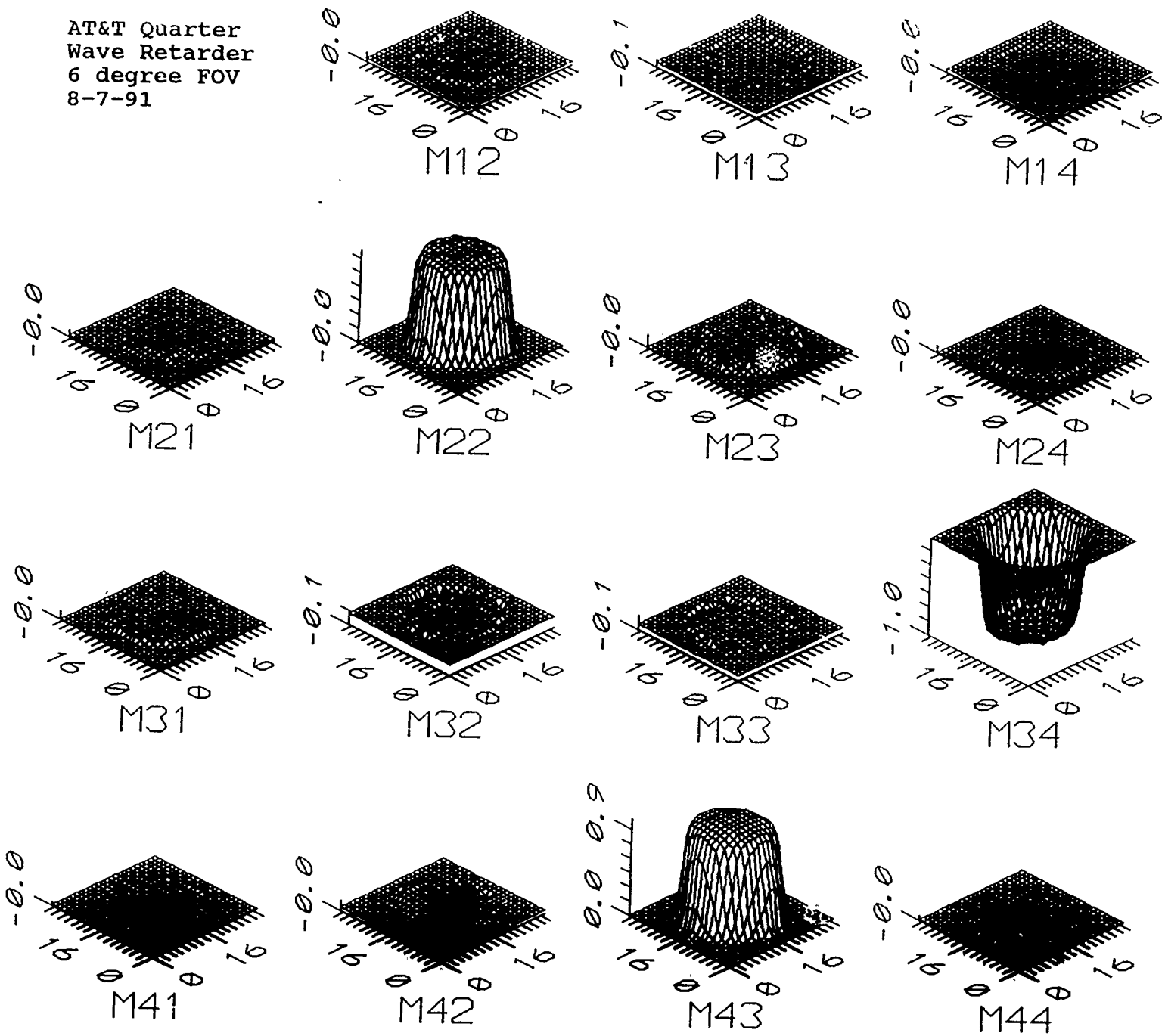
AT&T Quarter
Wave Retarder
6 degree FOV
8-7-91
M12
M13
M14
M21
M22
M23
M24
M31
M32
M33
M34
M41
M42
M43
M44

Figure 10

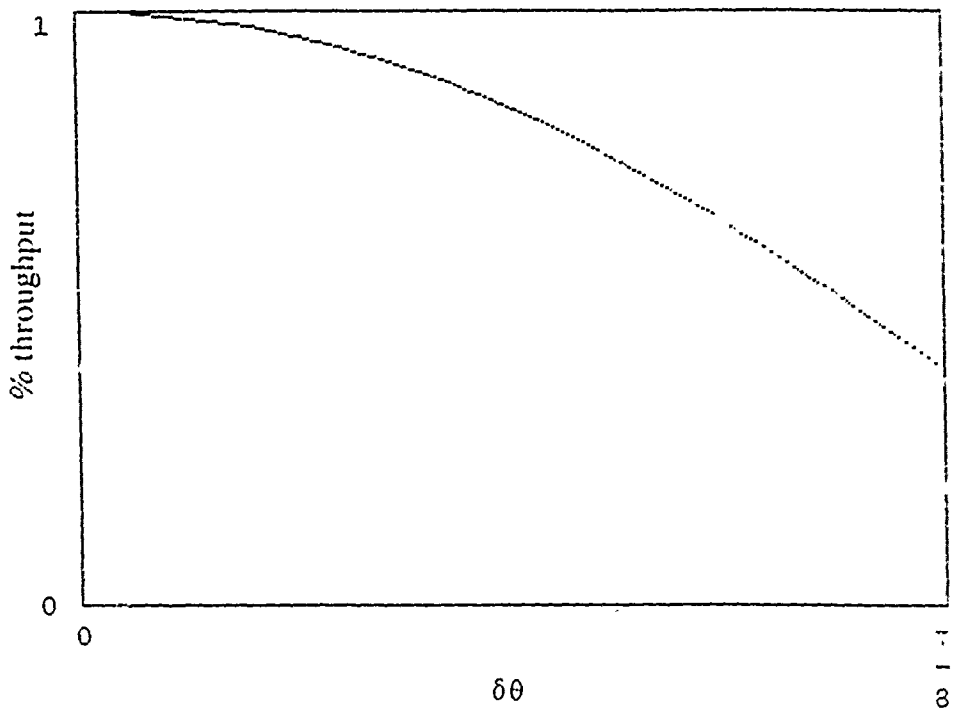

Figure 11 Fraction of transmitted intensity through a Cascadable Optical Logic Module plotted as a function of orientation error of the quarter wave retarders. Each of the quarter wave retarders recieved the same amount of orientation error.

polarizing beam splitters 6 times, quarter wave retarders 10 times and change polarization state 14 times.

Figure 12 shows the configuration of the Photonic Switching Network. The line indicates the path of light propagation. The desired polarization changes of the beam are indicated on the drawing. *H* indicates horizontal polarization (within the plane of the page), *V* indicates vertical polarization, and *R* and *L* indicate right and left circular polarization. The path analyzed is as follows: from the binary phase grating the beam passes through a space of the patterned reflector, through the polarizing beam splitter/quarter wave retarder combination onto the s-SEED in module 1. After reflecting off the s-SEED it reflects off the polarizing beam splitter toward the interconnection unit. The beam reflects off the plane mirror into the interconnection unit and the polarizing beam splitter divides the beam into two equal amplitudes in orthogonal directions. Half the amplitude passes through the polarizing beam splitter to the plane mirror and half reflects toward the retro-reflector. The beam which reflects to the retro-reflector is flipped about the vertex of the retro-reflector and passes back through the polarizing beam splitter into the next module. Both beams either transmit or reflect from the polarizing beamsplitter and reflect from the patterned mirrors shown and are imaged onto the s-SEED in module 2.

Our analysis was done over a ±10° field of view. The assumptions are as follows:

1. The beams are uniformly circularly polarized at the first patterned reflector.
2. The quarter wave retarders have exactly a quarter wave of retardance.
3. The retardance varies insignificantly over the ±10[EQUATION] field of view. (Section 2.2 supports this assumption).
4. The polarizing beam splitters transmit 100% p polarization and reflect 100% s polarization for all angles of incidence. This assumption is also made to simplify interpretation of results and can be readily generalized to the non-ideal case.

Figure 13 shows a chief ray path through this portion of the Photonic switching Network (Iteration 3). The patterned reflectors, mirrors, retro-reflectors and modulators are situated in image planes. The polarizing beam splitters and quarter wave retarders are positioned at or near the pupils. Since the system is doubly telecentric and the image planes are at infinite conjugates, the beams are collimated when they reach the polarizing beam splitters and quarter wave retarders. It is therefore sufficient to trace a set of chief rays through the system to characterize the polarizing behavior associated with each beam.

Iteration 3, s-SEED-based Photonic Switching Network

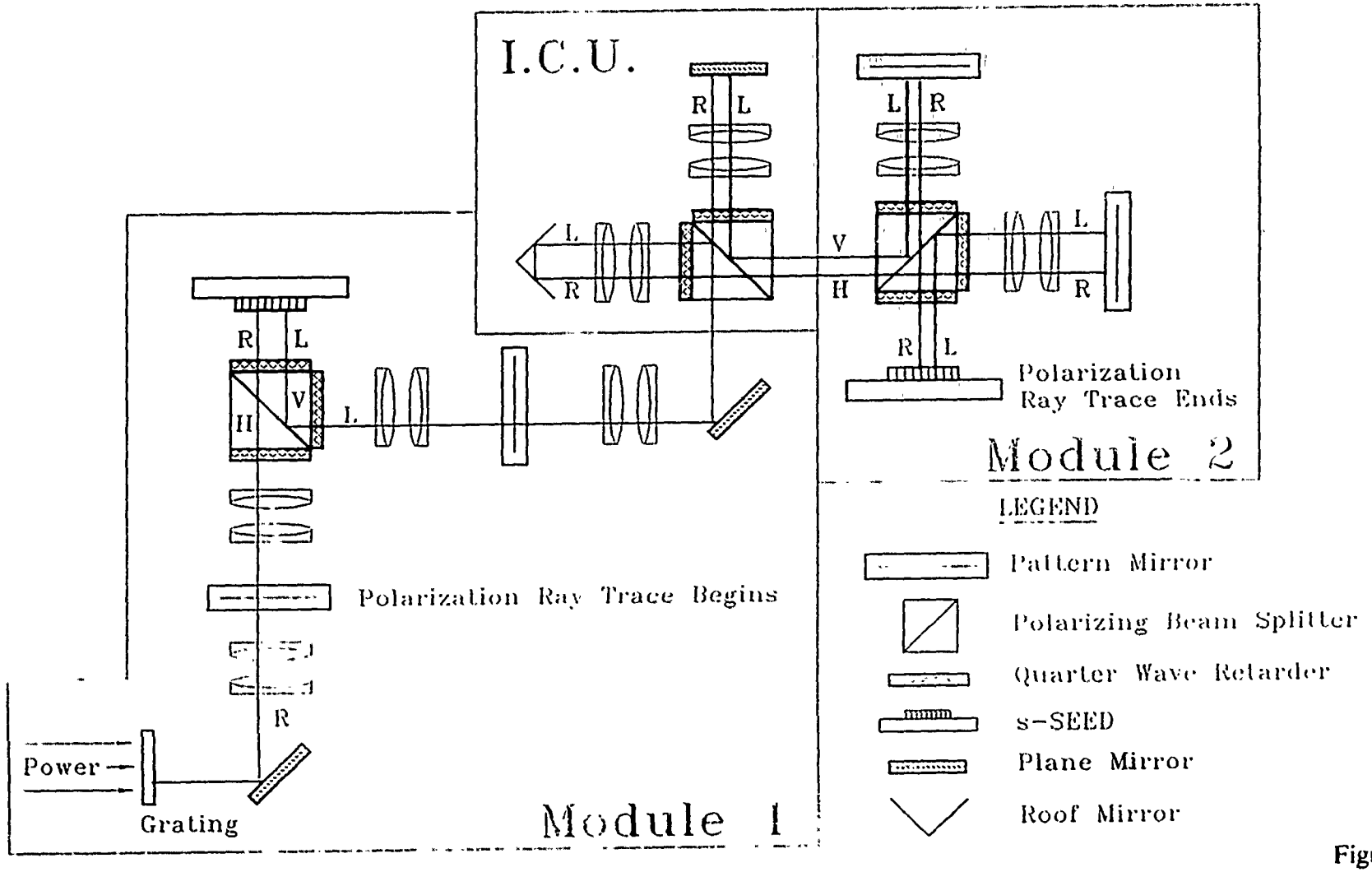

Figure 12

Iteration 3, s-SEED based Photonic Switching Network

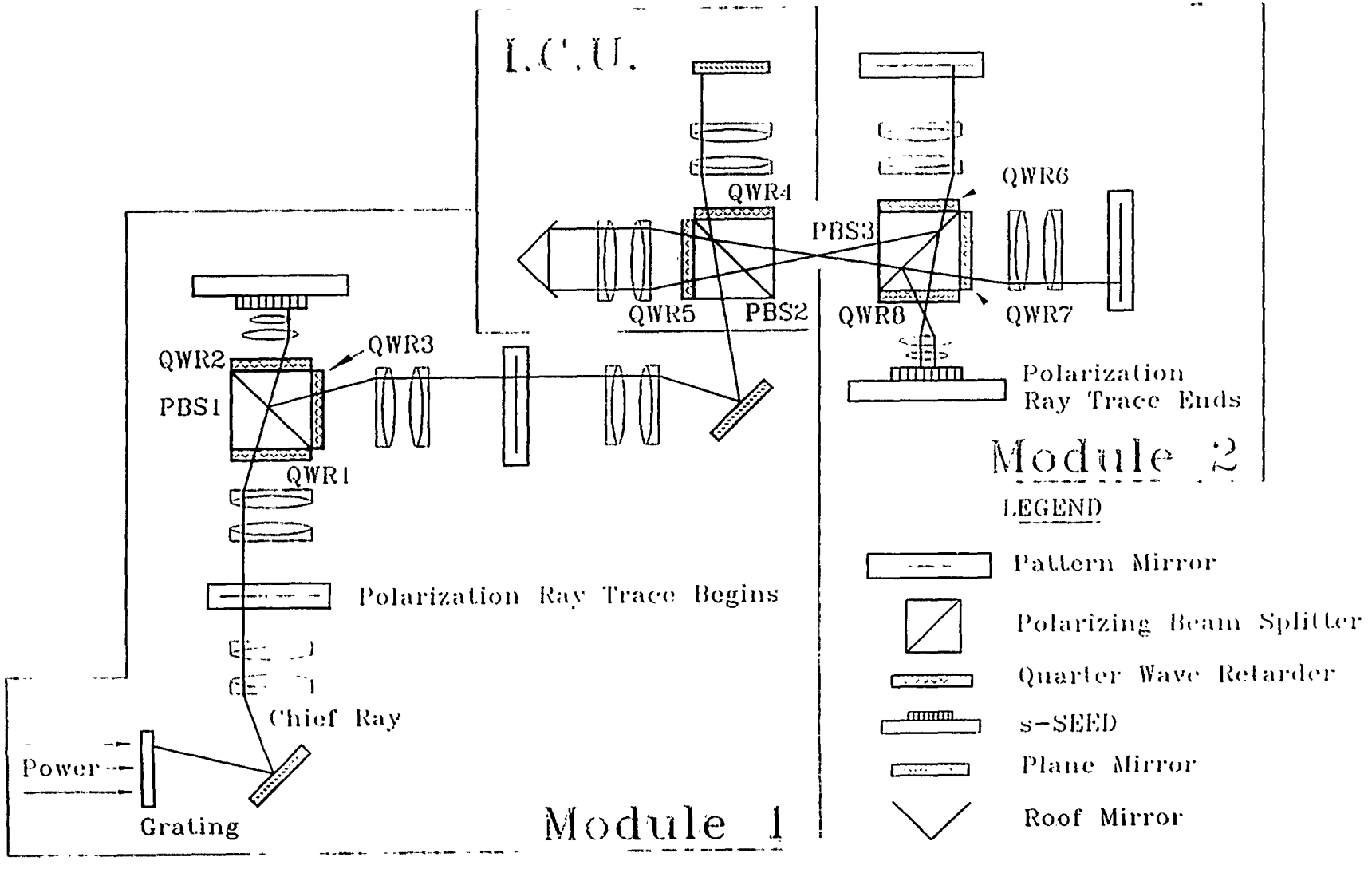

Figure 13

The polarization ray trace begins at the first pattern reflector and ends at the s-SEED array in Module 2. *The results are all given in terms of the object coordinates defined at the first patterned reflector.*

The polarization changes that take place in the Photonic Switching Network are formulated in terms of the Jones Calculus, and are illustrated via a series of graphical maps of polarization. The graphical plots of polarization depict the polarization state of the chief rays. This approach provides an intuitive picture of the changes of polarization of off axis rays.

Figure 14 illustrates the path from the first patterned reflector PR1, through the first polarizing beam splitter PBS1 to the s-SEED which reflects the light back to PBS1 which in turn reflects it toward the Interconnection Unit. The coordinate system for the Chief rays are defined at PR1: the positive x direction is shown at PR1 and y points out of the page. Like positions on each of the plots I-VI, correspond to the same chief ray. The positive x direction on plots I-VI corresponds to the Chief ray path shown on the drawing. The linear polarization states of the Chief rays at the polarizing beam splitter interface are shown because it is easier to interpret linear polarization states than circular and elliptical states found at the image planes.

The circularly polarized beams at PR1 are converted to uniform horizontal linear polarization by QWR1 just before PBS1 (Figure 14-III). Figure 14-I illustrates the variation of orientation of p directions the chief rays make with the beamsplitting interface of PBS1, shown as a function object coordinate of the Chief rays. Chief rays from object points for which $y > 0$ encounter p directions rotated in the clockwise direction and when $y < 0$ the rotation is counter-clockwise. The amount of rotation is denoted $\theta(x, y)$, and is a function of object coordinates. For an ideal polarizing beam splitter, only light polarized in the p direction is transmitted. To determine the fraction of the incident horizontally polarized beams which are transmitted by PBS1, the incident beams polarization state must be decomposed into the local s and p directions at the PBS1 beam splitting interface. For Chief rays in which $y = 0$, the horizontal direction aligns with the p direction, and 100% of these beams are transmitted. For Chief rays in which $y \neq 0$, a fraction of the horizontal polarization lies in the s plane and is reflected. Because a fraction of intensity is reflected out of the incident horizontally polarized beams, the transmitted beams linear polarization direction is rotated by an amount $\theta(x, y)$ to align with the p directions of the PBS1 interface (compare Figures 14-I and 14-IV).

Beam Combining Module

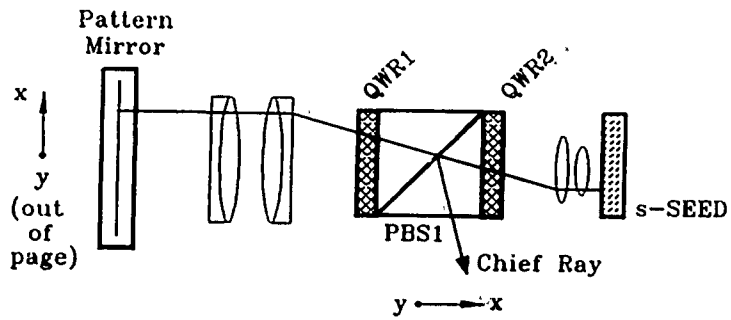

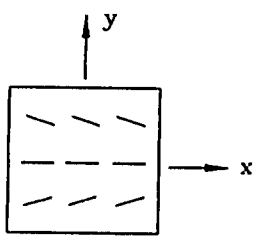

I. p orientation at PBS1 first pass

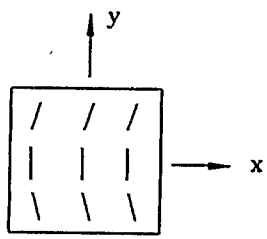

II. s orientation at PBS1 Second pass

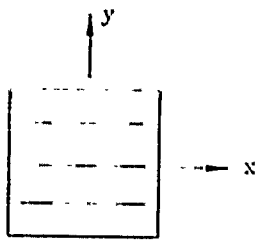

III. Polarization before PBS1 first pass

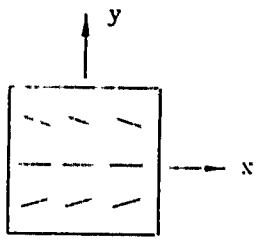

IV. Polarization after PBS1 first pass

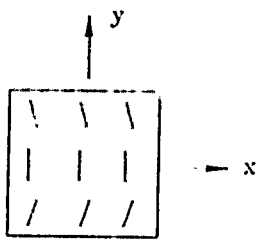

V. Polarization before PBS1 second pass

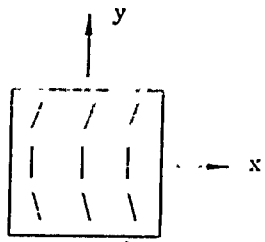

VI. Polarization after PBS1 Second pass

Figure 14

QWR2 converts the linearly polarized beams into right circular and elliptically polarized beams. After reflection, the beams are left circular and elliptically polarized. The second pass through QWR2 converts the left circular and elliptical beams back into linear states. In double pass, the quarter wave retarder acts like a half wave retarder. Figure 15 shows how a quarter wave retarder rotates linear polarization in double pass. The linear polarization of the entering and exiting beams are not orthogonal when $y \neq 0$, but have an angular separation of 2s. Because the s and p directions are orthogonal on a polarizing beam splitter cube, the entering and exiting beams polarization directions must be orthogonal for optimal efficiency. Because the linear polarization directions before the first pass through QWR2 and after the second pass through QWR2 are not orthogonal, i.e., separated by 2s, the polarizing beam combining module does not operate optimally with a quarter wave retarder. Figure 16 shows the fraction of horizontally polarized light which passes through the polarization beam combining module over a $\pm 10^{\circ}$ FOV.

Figure 17 shows the action of a quarter wave circular retarder on incident linearly polarized light. In double pass, the quarter wave circular retarder is equivalent to a half wave circular retarder. The half wave circular retarder rotates incident linear polarization states 90°, independent of incident linear polarization state orientation. The use of a circular retarder in a polarization beam combining scheme allows a more effective means of orienting the linear polarization state into the correct direction for the second pass (the reflection) off the polarizing beam splitter cube. Figure 18 shows the polarization states before and after each pass through the polarizing beam splitter. Note that the orientations of linear polarization for each pass through PBS1 align with the s and p directions of PBS1. Figure 19 shows the fraction of horizontally polarized light passes through the polarization beam combining module over a $\pm 10^{\circ}$ FOV.

Figure 20 gives the difference in the fraction of light that passes through the polarization beam combing module between using a quarter wave linear retarder and a quarter wave circular retarder. The Jones calculus of the above situation is provided in Figures 21 and 22.

The configuration in this situation occurs two other times in the path of our analysis. It occurs in the plane mirror path of the ICU and it also occurs module 2 (refer to Figure 13). Figure 23 shows the locations where it would be beneficial to replace the quarter wave linear retarders with quarter wave circular retarders.

The polarization ray trace proceeds in Figure 24. This Figure represents the path

Action of a Quarter Wave Retarder on Linear polarization in double pass

Quarter Wave Retarder in double pass

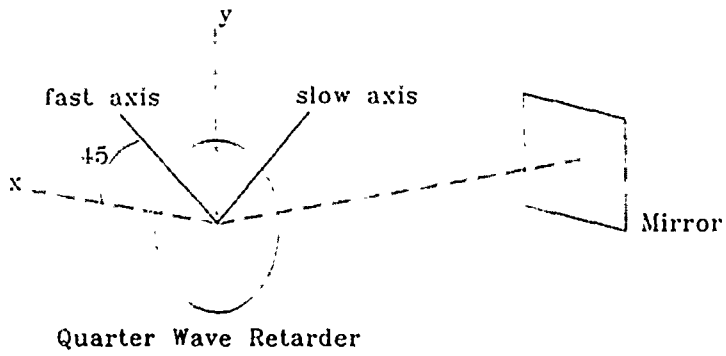

$$J = J_{refl}QWR(-45°)\,J_{refl}QWR(45°)$$

$$J = \begin{pmatrix} -1 & 0 \\ 0 & 1 \end{pmatrix}\frac{1}{\sqrt{2}}\begin{pmatrix} 1 & -i \\ -i & 1 \end{pmatrix}\begin{pmatrix} -1 & 0 \\ 0 & 1 \end{pmatrix}\frac{1}{\sqrt{2}}\begin{pmatrix} 1 & i \\ i & 1 \end{pmatrix} = \begin{pmatrix} 0 & 1 \\ 1 & 0 \end{pmatrix} = HWR(45°)$$

Half Wave Retarder in single pass

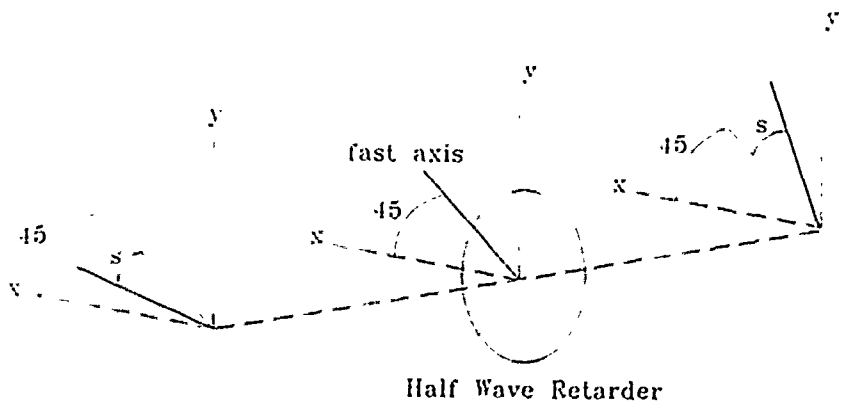

$$\vec{E} = \begin{pmatrix} Cos(s) \\ Sin(s) \end{pmatrix} = J\begin{pmatrix} Sin(s) \\ Cos(s) \end{pmatrix} = J\vec{E}$$

$$<\vec{E}\,|\,\vec{E}> = Cos(2s)$$

Figure 15

Efficiency of a Polarization Beam Combining Module for incident horizontally polarized light

(utilizing quarter wave retarders)

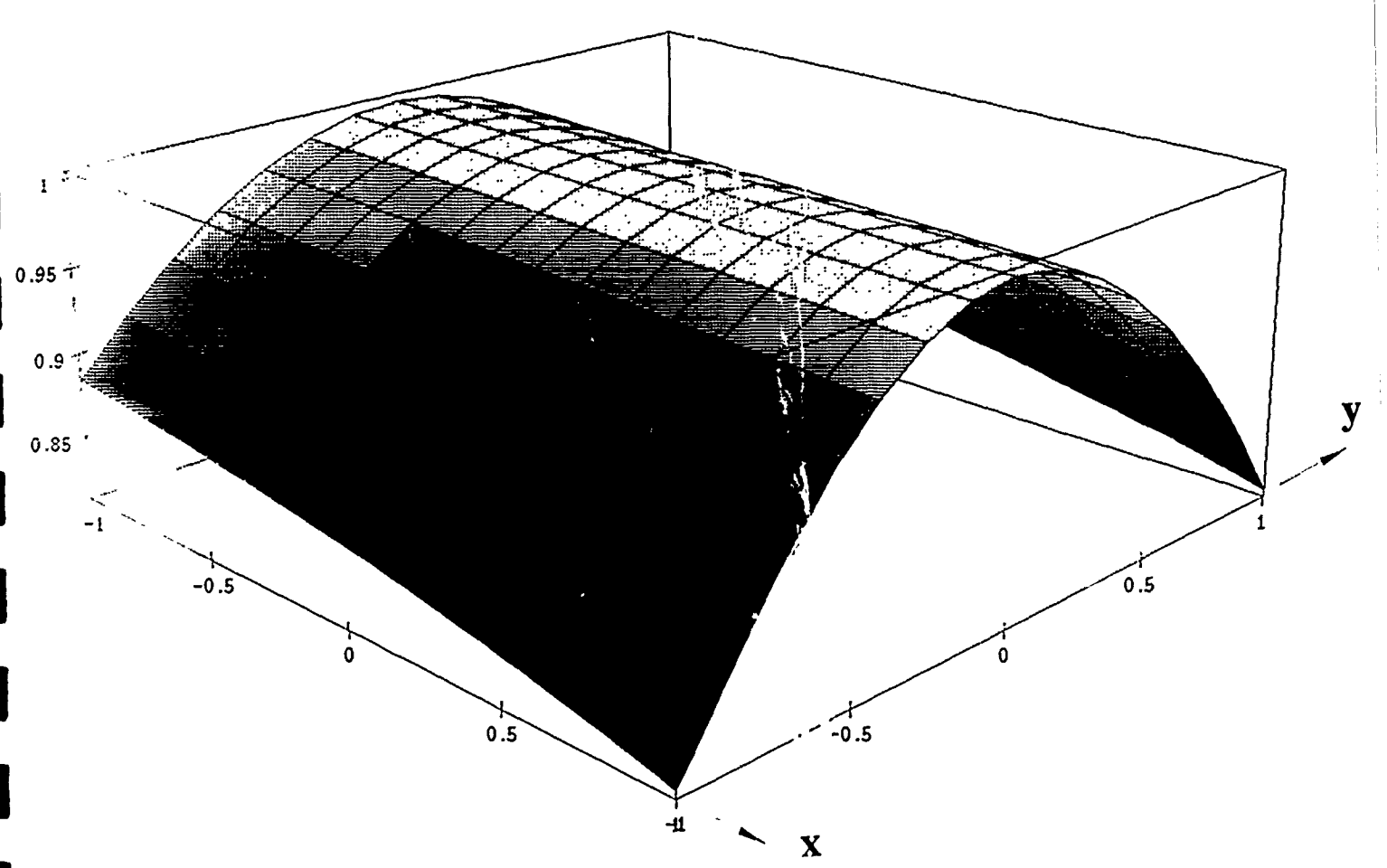

*** Plotted as a function of object coordinate, defined at PR1**

Figure 16

Action of a Circular Retarder on Linear polarization in double pass

Quarter Wave Circular Retarder in double pass

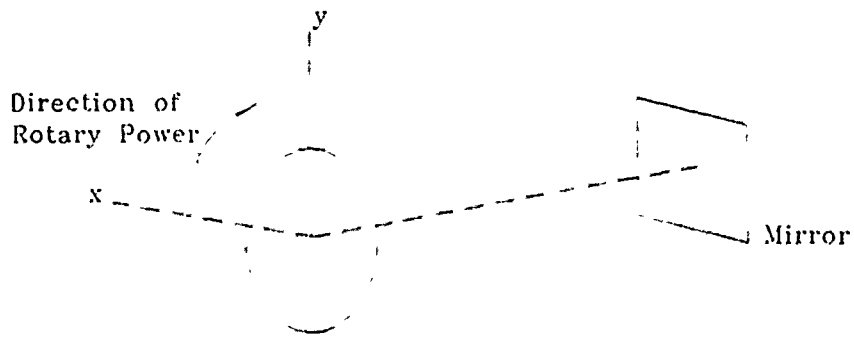

Quarter Wave Circular Retarder

$$J = J_{refl}\,CR\,J_{refl}\,CR$$

$$J = \begin{pmatrix} -1 & 0 \\ 0 & 1 \end{pmatrix} \frac{1}{\sqrt{2}} \begin{pmatrix} 1 & 1 \\ 1 & -1 \end{pmatrix} \begin{pmatrix} -1 & 0 \\ 0 & 1 \end{pmatrix} \frac{1}{\sqrt{2}} \begin{pmatrix} 1 & -1 \\ 1 & 1 \end{pmatrix} = \begin{pmatrix} 0 & -1 \\ 1 & 0 \end{pmatrix} = \text{HWCR}$$

Half Wave Circular Retarder in single pass

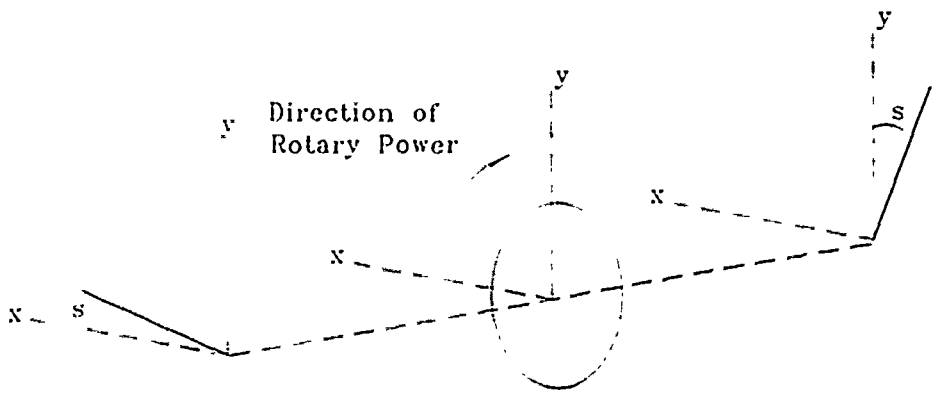

Half Wave Circular Retarder

$$\vec{E}' = \begin{pmatrix} -\text{Cos}(s) \\ \text{Sin}(s) \end{pmatrix} = J \begin{pmatrix} \text{Sin}(s) \\ \text{Cos}(s) \end{pmatrix} = J\vec{E}$$

$$\langle \vec{E}' \mid \vec{E} \rangle = 0$$

Figure 17

Beam Combining Module

(Design Altered)

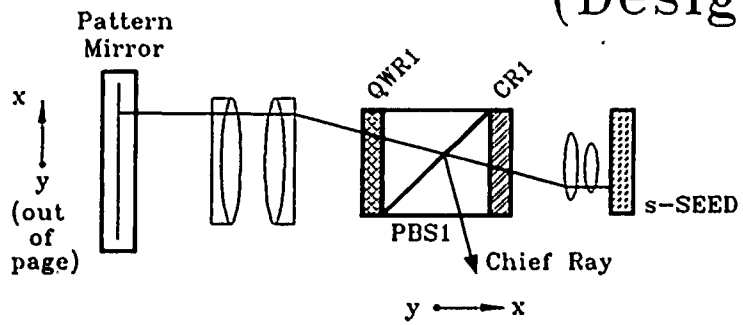

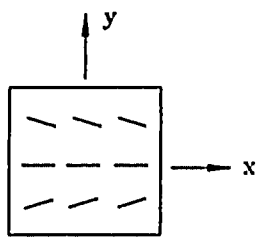

I. p orientation at PBS1 first pass

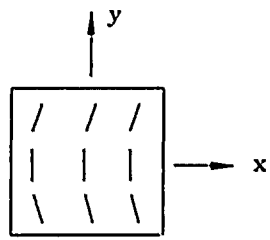

II. s orientation at PBS1 Second pass

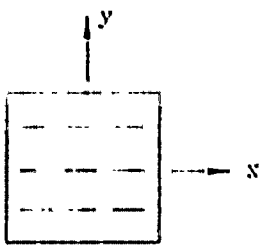

III. Polarization before PBS1 first pass

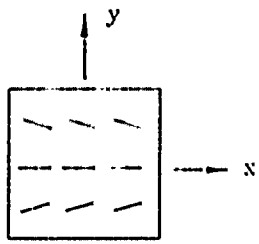

IV. Polarization after PBS1 first pass

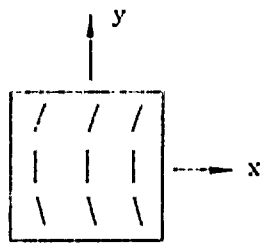

V. Polarization before PBS1 second pass

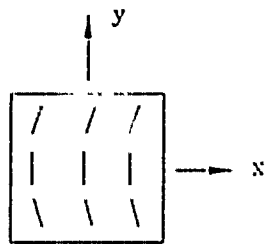

VI. Polarization after PBS1 Second pass

Figure 18

Efficiency of a Polarization Beam Combining Module for incident horizontally polarized light

(utilizing circular retarders)

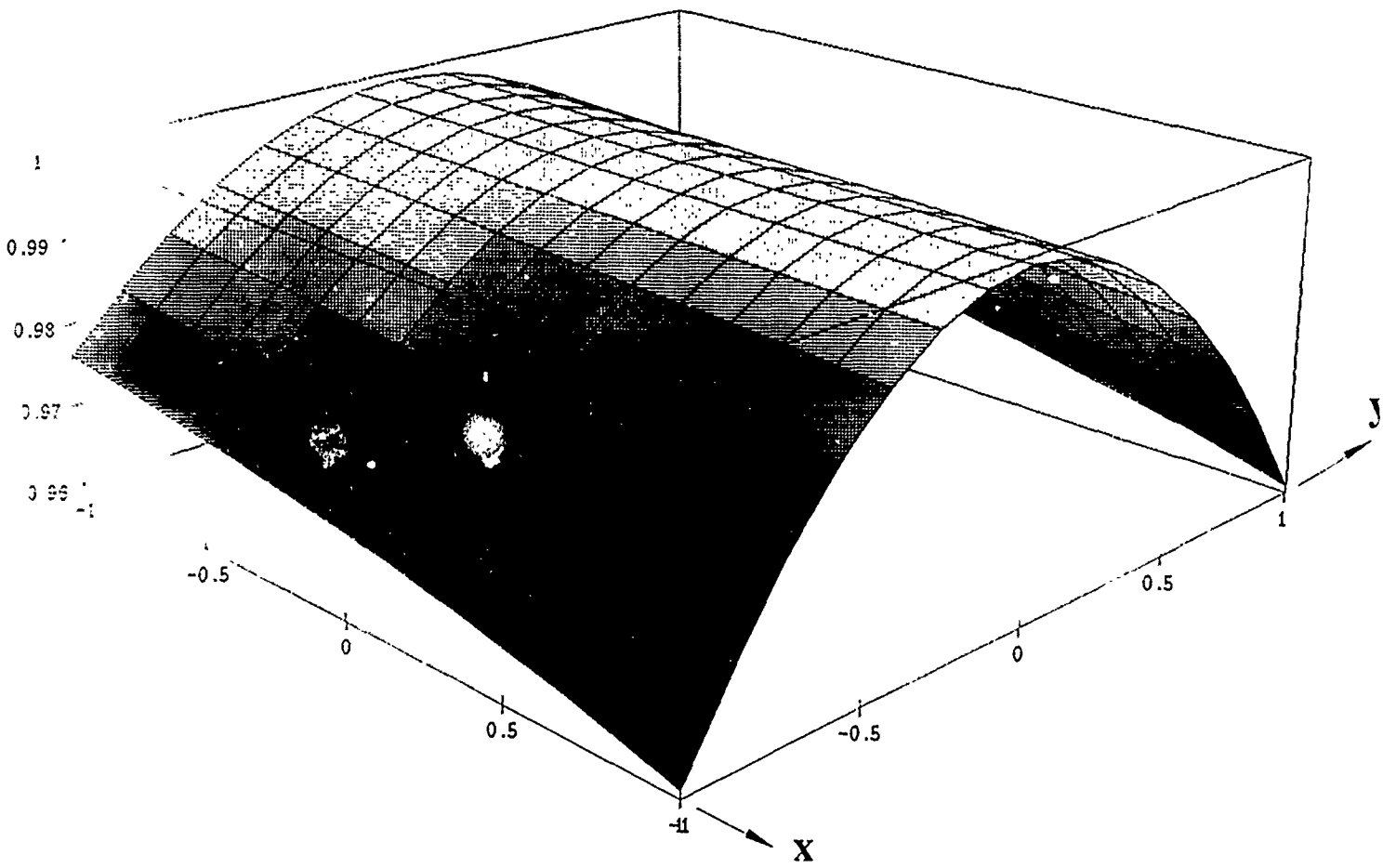

* Plotted as a function of object coordinate, defined at PR1

Figure 19

Efficiency difference between a Polarizing Beam Combining Module which utilizes circular retarders and one which utilizes quarter wave retarders

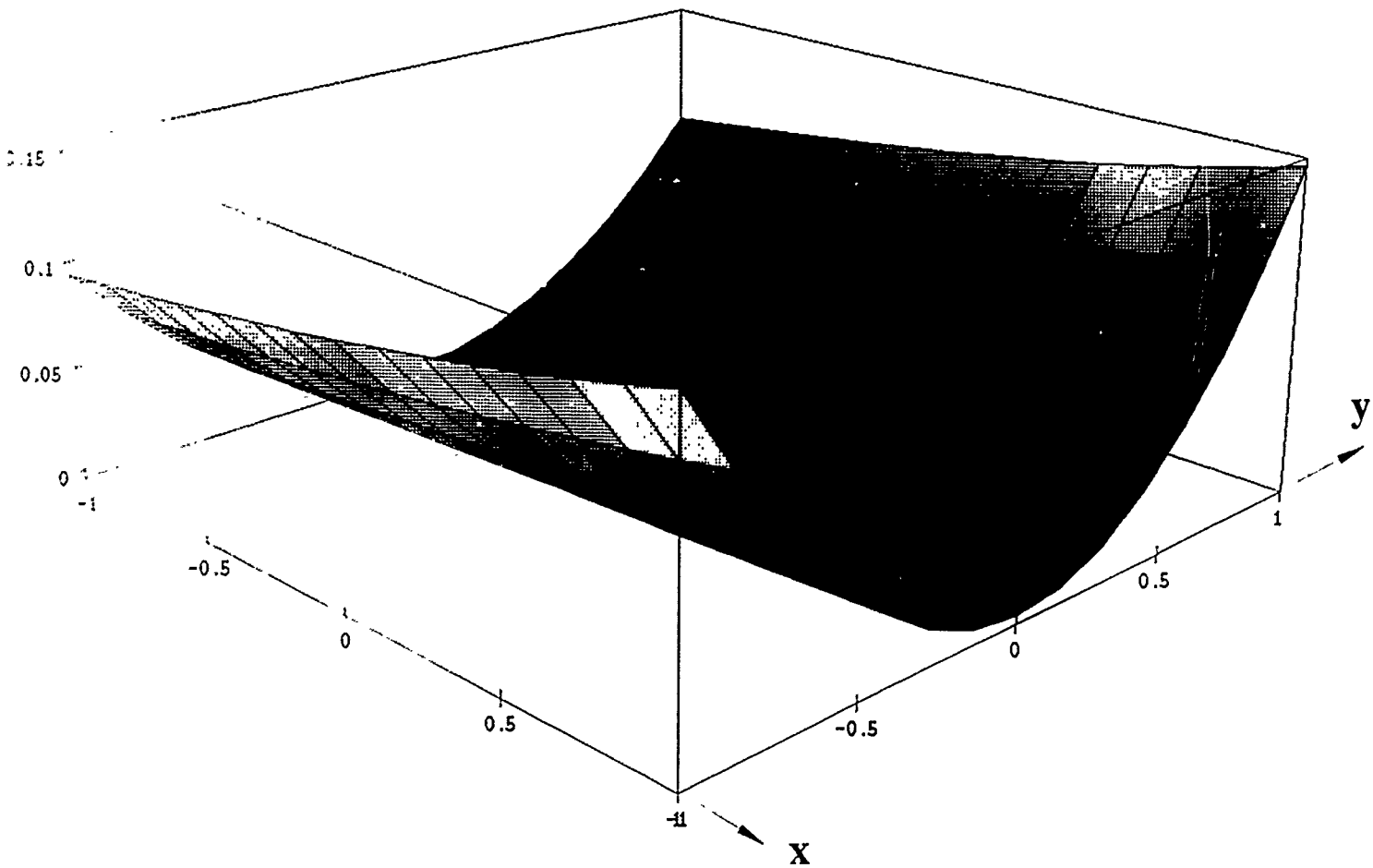

* Plotted as a function of object coordinate, defined at PR1

Figure 20

Jones calculus for a Polarization Beam Combining Module

(utilizing quarter wave retarders)

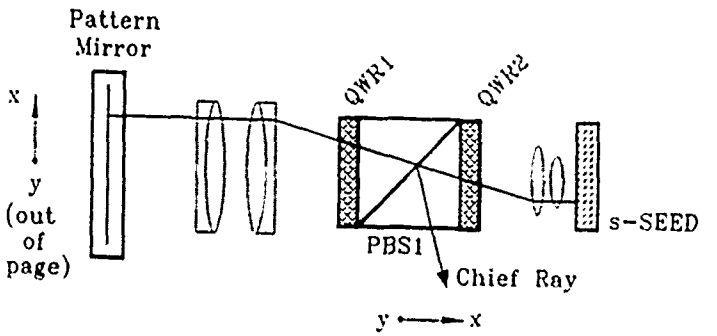

$$J = PBS(\theta)_{out} J_{mirror} QWLR(-45°) J_{mirror} QWLR(45°) PBS(\theta)_{train}$$

$$J = \begin{pmatrix} S^2 & -SC \\ -SC & C^2 \end{pmatrix}\begin{pmatrix} -1 & 0 \\ 0 & 1 \end{pmatrix}\frac{1}{\sqrt{2}}\begin{pmatrix} 1 & -i \\ -i & 1 \end{pmatrix}\begin{pmatrix} -1 & 0 \\ 0 & 1 \end{pmatrix}\frac{1}{\sqrt{2}}\begin{pmatrix} 1 & i \\ i & 1 \end{pmatrix}\begin{pmatrix} C^2 & SC \\ SC & S^2 \end{pmatrix}$$

$$J_1 = (\mathrm{Cos}^2\theta - \mathrm{Sin}^2\theta)\begin{pmatrix} -\mathrm{Sin}\theta\mathrm{Cos}\theta & -\mathrm{Sin}^2\theta \\ \mathrm{Cos}^2\theta & \mathrm{Sin}\theta\mathrm{Cos}\theta \end{pmatrix}$$

$$J_1 = \mathrm{Cos}2\theta\begin{pmatrix} -\mathrm{Sin}\theta\mathrm{Cos}\theta & -\mathrm{Sin}^2\theta \\ \mathrm{Cos}^2\theta & \mathrm{Sin}\theta\mathrm{Cos}\theta \end{pmatrix} = \mathrm{Cos}2\theta J_2$$

Figure 21

Jones calculus for a Polarization Beam Combining Module

(utilizing circular retarders)

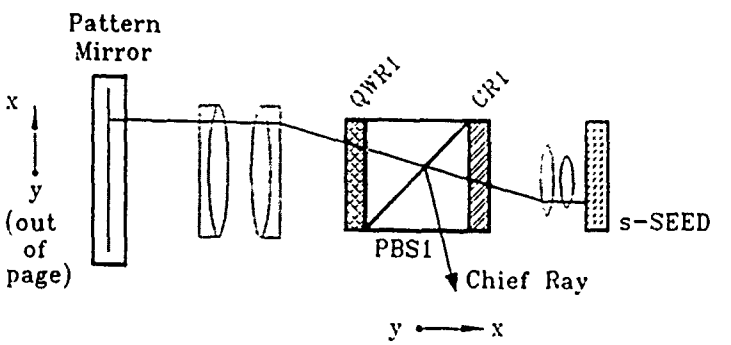

$$J_2 = PBS(\theta)_{refl} J_{mirror} CR \quad J_{mirror} CR \quad PBS(\theta)_{tran}$$

$$J_2 = \begin{pmatrix} S^2 & -SC \\ -SC & C^2 \end{pmatrix} \begin{pmatrix} -1 & 0 \\ 0 & 1 \end{pmatrix} \frac{1}{\sqrt{2}} \begin{pmatrix} 1 & 1 \\ -1 & 1 \end{pmatrix} \begin{pmatrix} -1 & 0 \\ 0 & 1 \end{pmatrix} \frac{1}{\sqrt{2}} \begin{pmatrix} 1 & -1 \\ 1 & 1 \end{pmatrix} \begin{pmatrix} C^2 & SC \\ SC & S^2 \end{pmatrix}$$

$$J_2 = \begin{pmatrix} -\mathrm{Sin}\,\theta\,\mathrm{Cos}\,\theta & -\mathrm{Sin}^2\theta \\ \mathrm{Cos}^2\theta & \mathrm{Sin}\,\theta\,\mathrm{Cos}\,\theta \end{pmatrix}$$

Figure 22

Photonic Switching Network

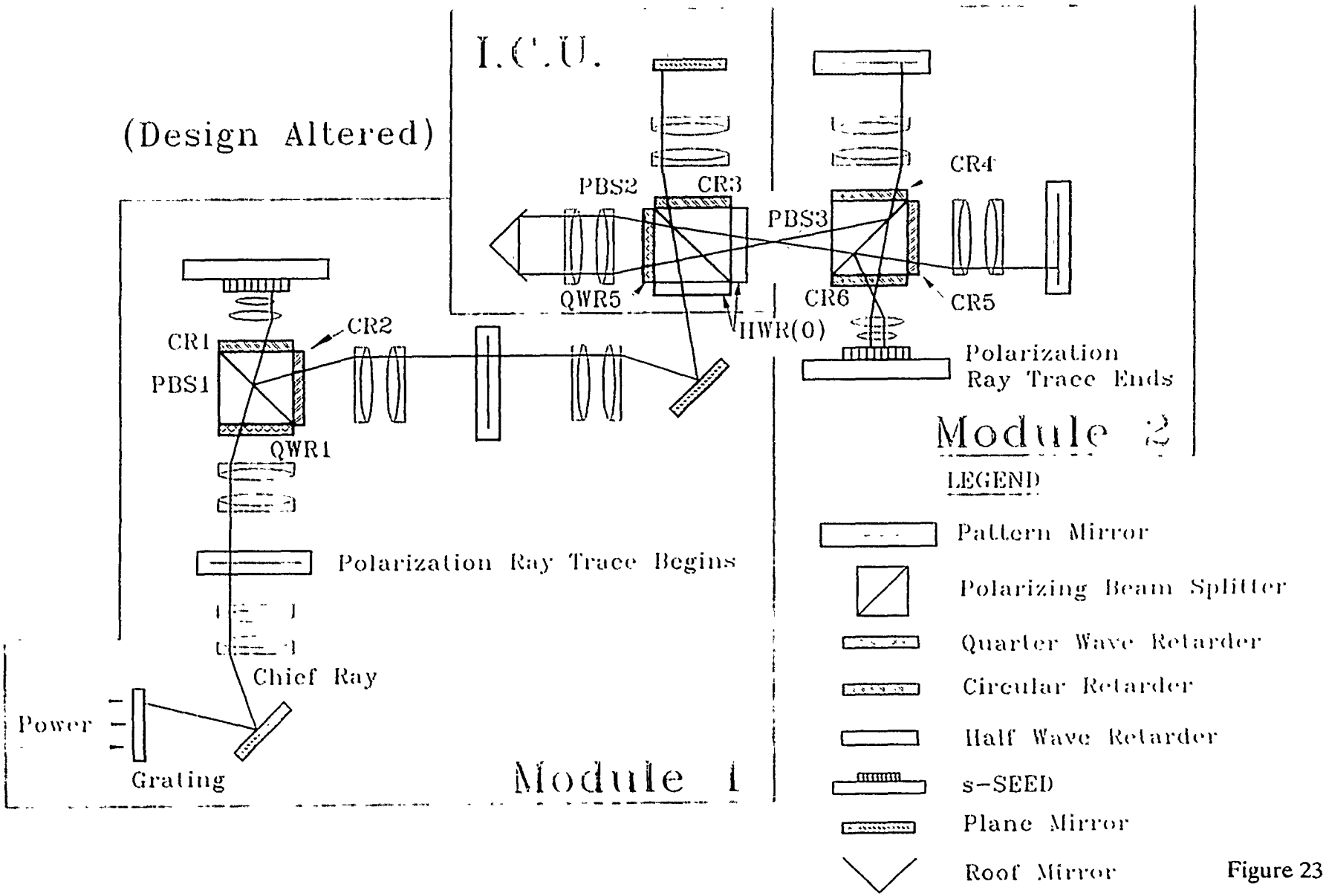

Figure 23

Path from s-SEED to ICU

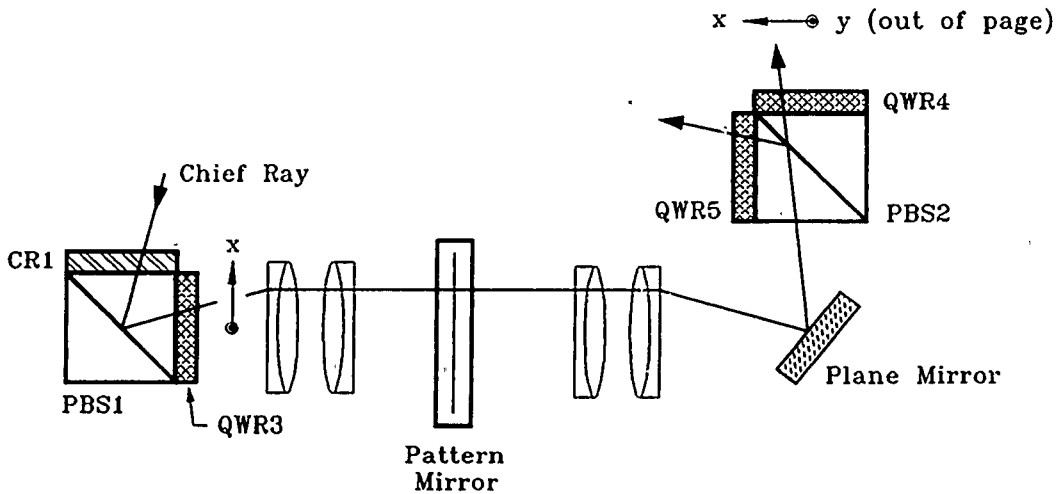

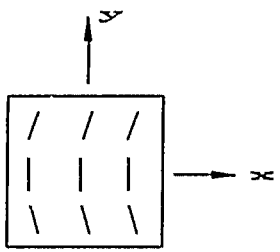

I. s orientation at PBS1

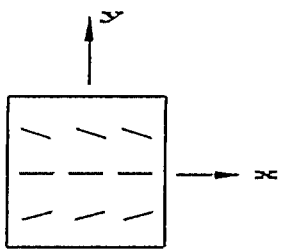

II. p orientation at PBS2

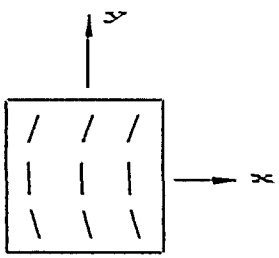

III. Polarization before PBS1

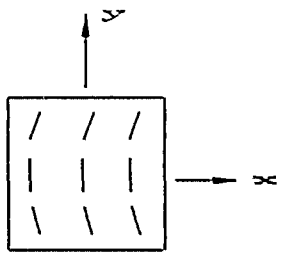

IV. Polarization after PBS1

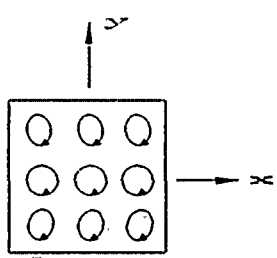

V. Polarization before PBS2

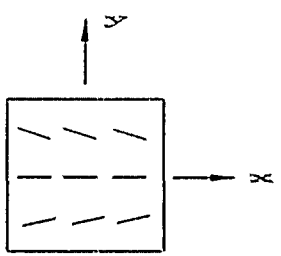

VI. Polarization after PBS2

Figure 24

from the s-SEED in module 1 to the ICU with existing polarizing optics. QWR3 converts the linear polarization states reflected from PBS1 to circular and elliptical states. The orientation of their major axes are flipped by the plane mirror before the ICU as shown. The orientations of the polarization ellipses are such that more power is transmitted by PBS2 than reflected. We will not show the distribution of reflected and transmitted power since our analysis will proceed after replacing QWR2 with a circular retarder.

Figure 25 shows the same path as above except we have now replaced QWR3 with a half wave circular retarder, CR2, and added a half wave linear retarder. We replaced QWR3 with CR2 for the benefit of beams entering module 1 from the signal port of PBS1, and we will explain why a half wave retarder has been added next.

CR1 rotates the linear polarization states reflected from PBS1 45°, and the plane mirror before the ICU flips their orientation into that shown in Figure 25-V. The linear polarization of each beam is oriented at 45° with respect to the s and p directions each beam encounters at PBS2. The beams intensity of each beam is split by PBS2. Half the beam is transmitted toward the plane mirror and half is reflected toward the roof mirror. The intensity transmitted toward the plane mirror is plotted as a function of object coordinate in Figure 26. The intensity reflected toward the roof mirror is plotted as a function of object coordinate in Figure 27. The Jones calculus for this path is provided in Figure 28.

As stated earlier, the path from PBS2 to the plane mirror and back to PBS2 inside the ICU is similar to the path analyzed in Figure 18, and its performance is improved when a circular retarder is employed.

The path involving the roof mirror inside the ICU, however, benefits from the use of a quarter wave retarder. Figure 29 illustrates the ray trace involved in this situation. Since two reflections occur with the roof mirror the orientation of polarization states are align with the p states of PBS2 for transmission into module 2. The Jones calculus for this path is given in Figure 30.

Figure 31 shows the path from the PBS2 in the ICU to PBS3 in module 2. Note that the polarization directions emitted from PBS2 (Figure 31-IV) are not aligned with the p orientations of PBS3. The orientations of the linear polarization of these beams can be aligned with the p directions of PBS3 by inserting a half wave retarder at 0° anywhere between PBS2 and PBS3. The half wave retarder flips the polarization directions about the fast axis of the retarder to align their polarization directions with the p directions of PBS3.

Path from s-SEED to ICU

(Design Altered)

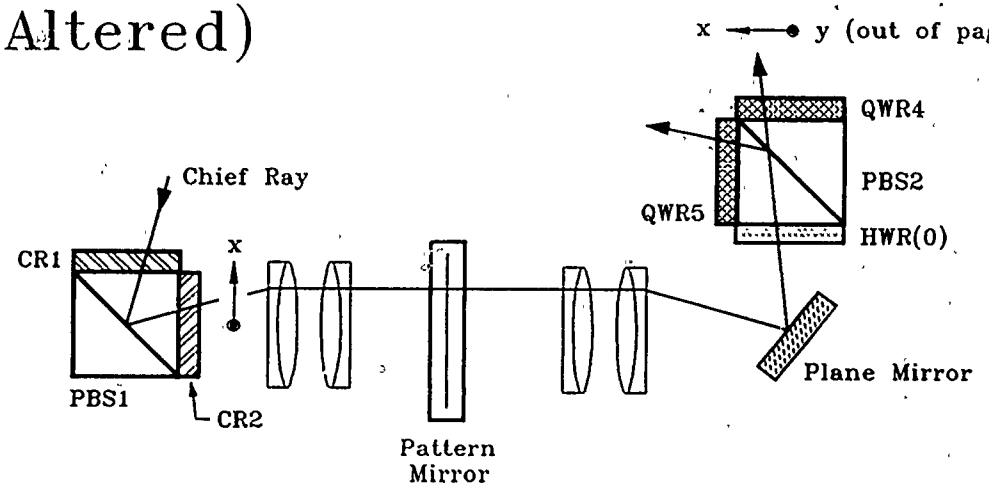

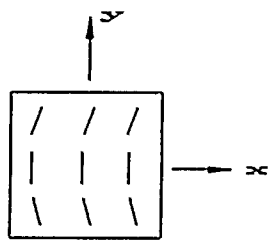

I. s orientation at PBS1

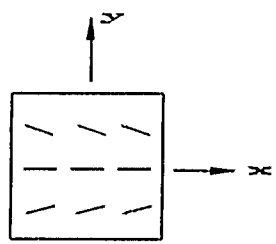

II. p orientation at PBS2

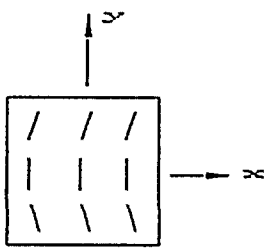

III. Polarization before PBS1

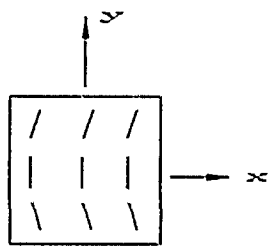

IV. Polarization after PBS1

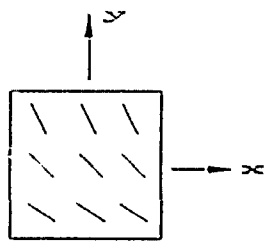

V. Polarization before PBS2

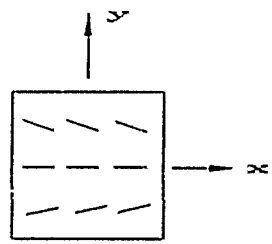

VI. Polarization after PBS2

Figure 25

Intensity distribution after transmission through PBS2

(Plane mirror path of ICU; design utilizes circular retarders and half waveplates)

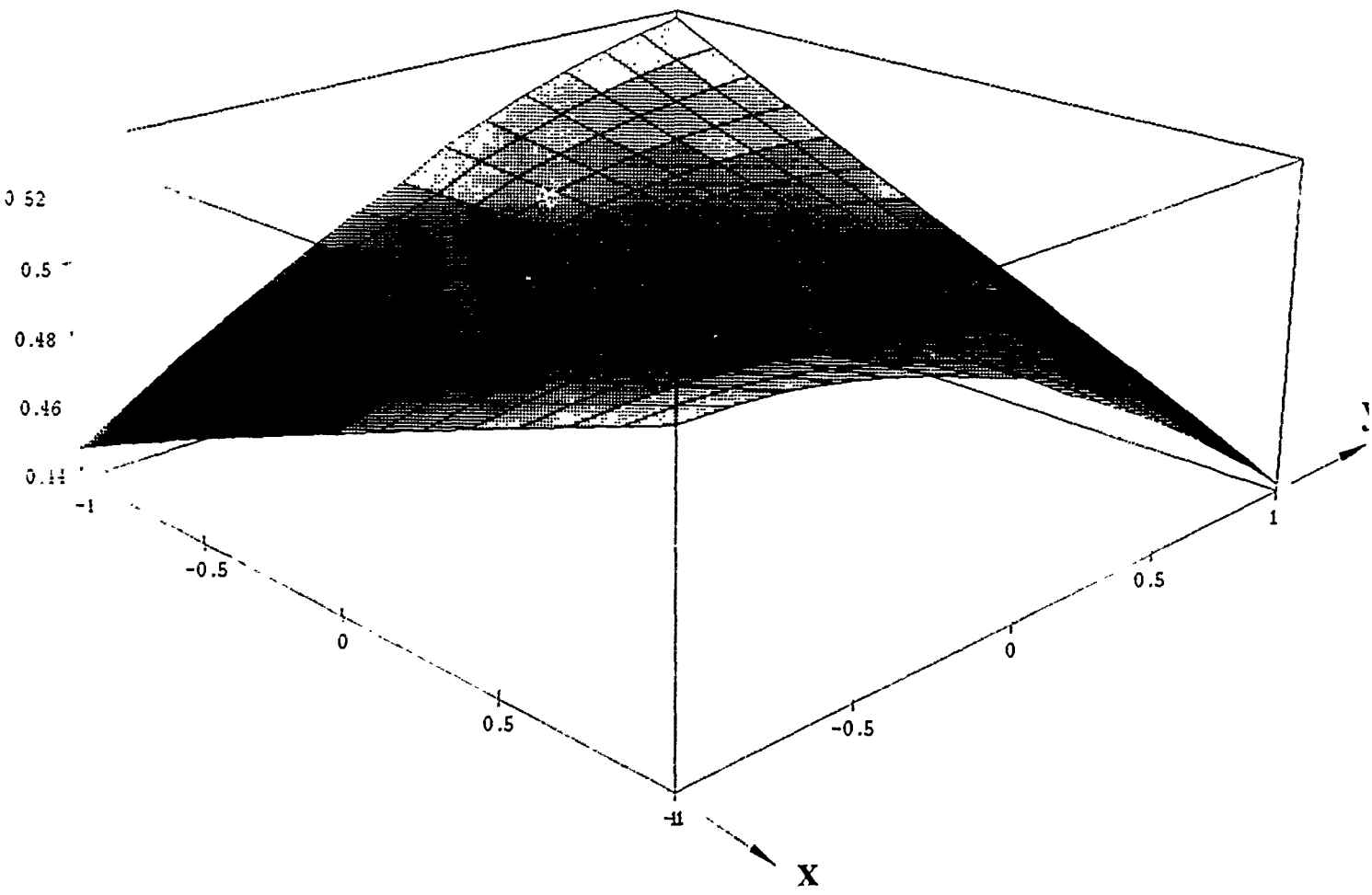

* Plotted as a function of object coordinate, defined at PR1

Figure 26

Intensity distribution after reflection from PBS2

(Roof Mirror path of ICU; design utilizes circular retarders and half wave retarders)

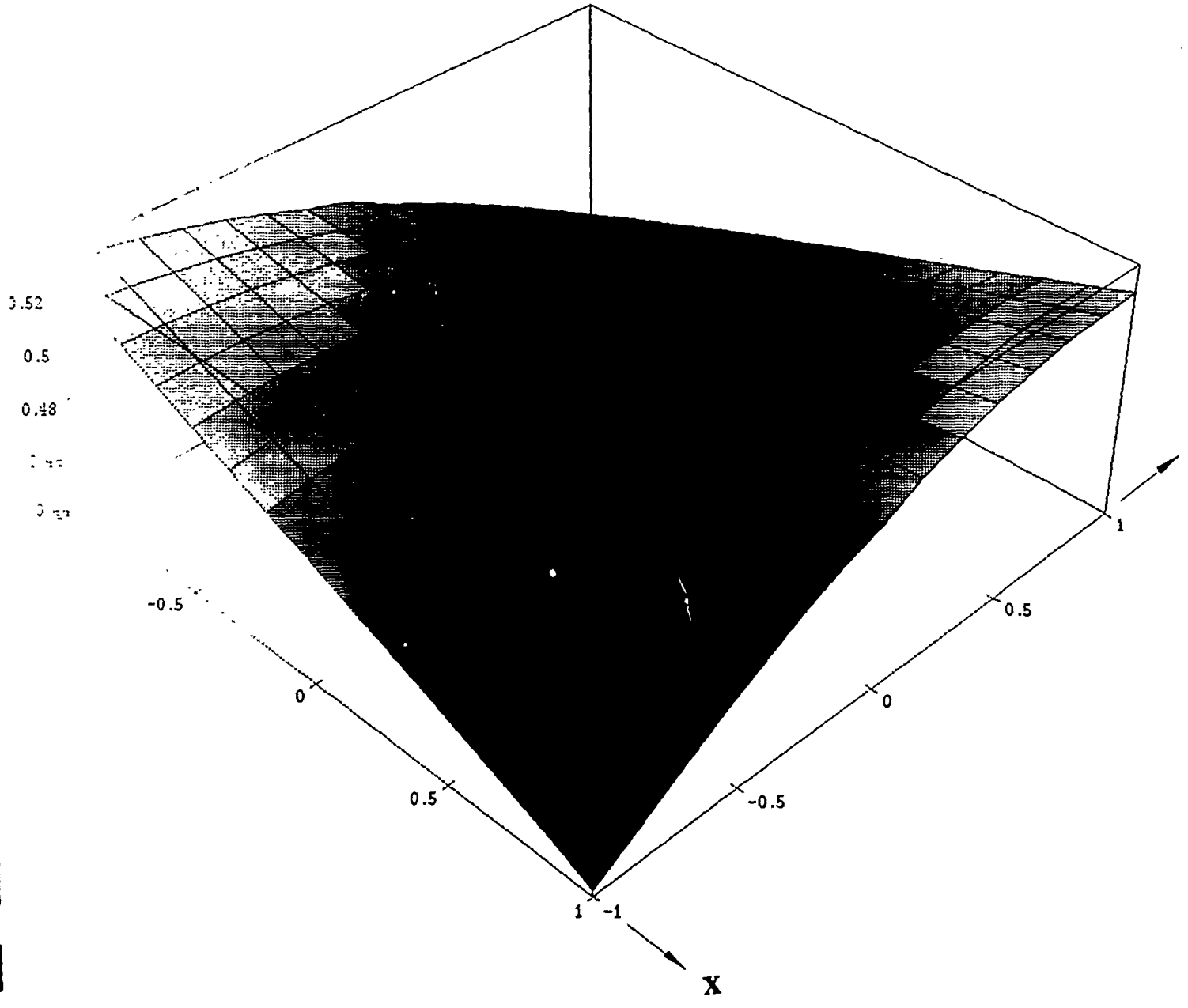

*** Plotted as a function of object coordinate, defined at PR1**

Figure 27

Jones calculus of path from s-SEED to ICU

(utilizing a circular retarder and a half wave retarder)

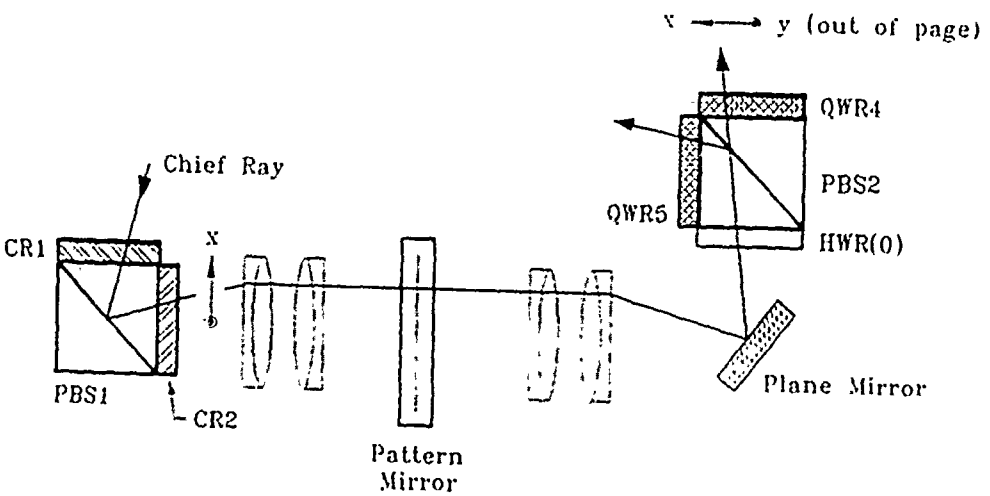

$$J = PBS(\theta')\,HWR(0°)\,J_{mirror}\,CR$$

$$J = \begin{pmatrix} \mathrm{Cos}^2\theta' & \mathrm{Sin}\theta'\mathrm{Cos}\theta' \\ \mathrm{Sin}\theta'\mathrm{Cos}\theta' & \mathrm{Sin}^2\theta' \end{pmatrix}\begin{pmatrix} -1 & 0 \\ 0 & 1 \end{pmatrix}\begin{pmatrix} -1 & 0 \\ 0 & 1 \end{pmatrix}\frac{1}{\sqrt{2}}\begin{pmatrix} 1 & -1 \\ 1 & 1 \end{pmatrix}$$

$$J = \begin{pmatrix} \mathrm{Cos}^2\theta' + \mathrm{Sin}\theta'\mathrm{Cos}\theta' & -\mathrm{Cos}^2\theta' + \mathrm{Sin}\theta'\mathrm{Cos}\theta' \\ \mathrm{Sin}\theta'\mathrm{Cos}\theta' + \mathrm{Sin}^2\theta' & -\mathrm{Sin}\theta'\mathrm{Cos}\theta' + \mathrm{Sin}^2\theta' \end{pmatrix}$$

Figure 28

Roof Mirror Path

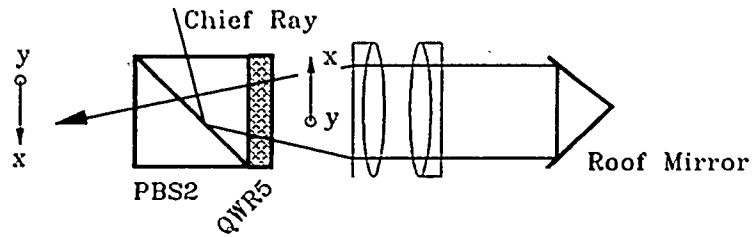

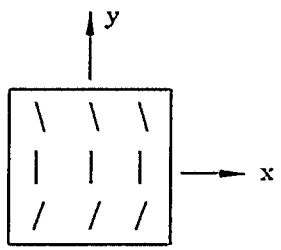

I. s orientation at PBS2 first pass

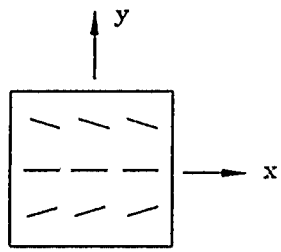

II. p orientation at PBS2 second pass

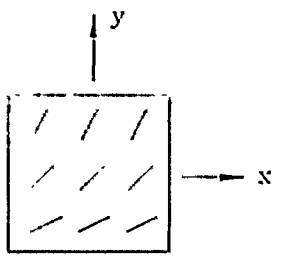

III. Polarization before PBS2 first pass

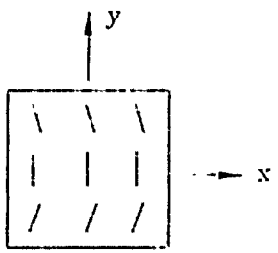

IV. Polarization after PBS2 first pass

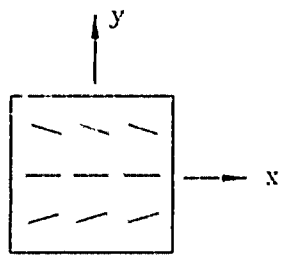

V. Polarization before PBS2 second pass

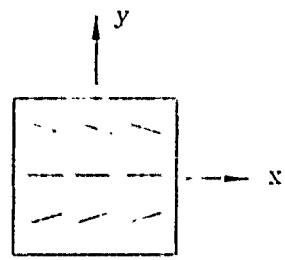

VI. Polarization after PBS2 second pass

Figure 29

Jones calculus of roof mirror path

(neglecting retardance of roof mirror)

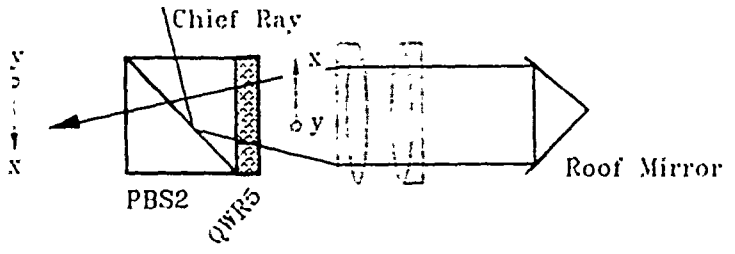

$$J = PBS(\theta)\,QWR(-45^\circ)\,J_{mirror}\,J_{mirror}\,QWR(45^\circ)$$

$$J = \begin{pmatrix} \mathrm{Cos}^2\theta & \mathrm{Sin}\,\theta\mathrm{Cos}\,\theta \\ \mathrm{Sin}\,\theta\mathrm{Cos}\,\theta & \mathrm{Sin}^2\theta \end{pmatrix} \frac{1}{\sqrt{2}}\begin{pmatrix} 1 & i \\ i & 1 \end{pmatrix}\begin{pmatrix} -1 & 0 \\ 0 & 1 \end{pmatrix}\begin{pmatrix} -1 & 0 \\ 0 & 1 \end{pmatrix}\frac{1}{\sqrt{2}}\begin{pmatrix} 1 & i \\ i & 1 \end{pmatrix}$$

$$J = \begin{pmatrix} \mathrm{Sin}\,\theta\mathrm{Cos}\,\theta & \mathrm{Cos}^2\theta \\ \mathrm{Sin}^2\theta & \mathrm{Sin}\,\theta\mathrm{Cos}\,\theta \end{pmatrix}$$

Figure 30

Path From ICU to Next Module

(Design Altered)

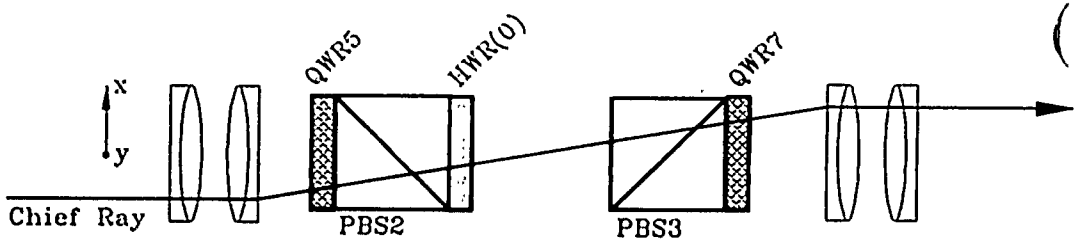

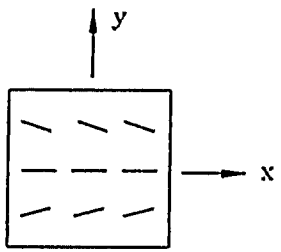

I. p orientation at PBS2

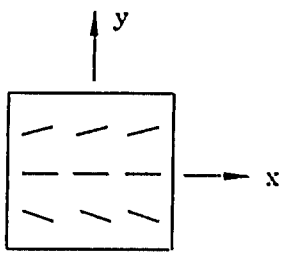

II. p orientation at PBS3

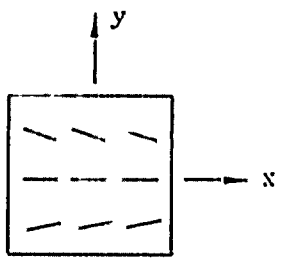

III. Polarization before PBS2

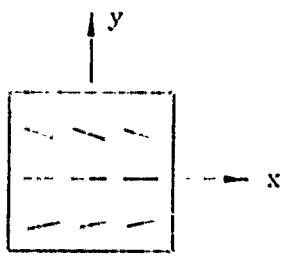

IV. Polarization after PBS2

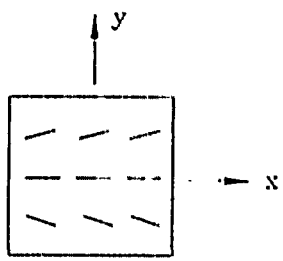

V. Polarization before PBS3

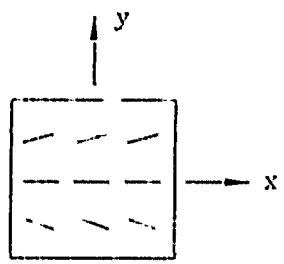

VI. Polarization after PBS3

Figure 31

The remaining paths, through PBS3 and reflection off PBS3 are similar to the situation analyzed in Figure 18, and are benefited by replacing the quarter wave linear retarders with half wave circular retarders.

The changes in the polarizing element design suggested by this analysis are shown in Figure 23 and can be contrasted with the existing design shown in Figure 13. Figure 32 shows the fraction of light which is transmitted by the entire path analyzed of the existing Photonic Switching Network as a function of object coordinate over a 10° FOV. The final result was obtained by summing the intensities of both paths in the ICU. Figure 33 shows the fraction of light which is transmitted by the entire path analyzed of the modified Photonic Switching Network as a function of object coordinate over a 10° FOV. The improvement of efficiency exists only for off axis object points for which $y \neq 0$, and assumes ideal circular retarders with uniform angular response. Research is needed to determine what kind of circular retarder is suitable for optical interconnect applications.

Efficiency of entire path modeled

(existing design; path which involves reflection off the roof mirror in the ICU)

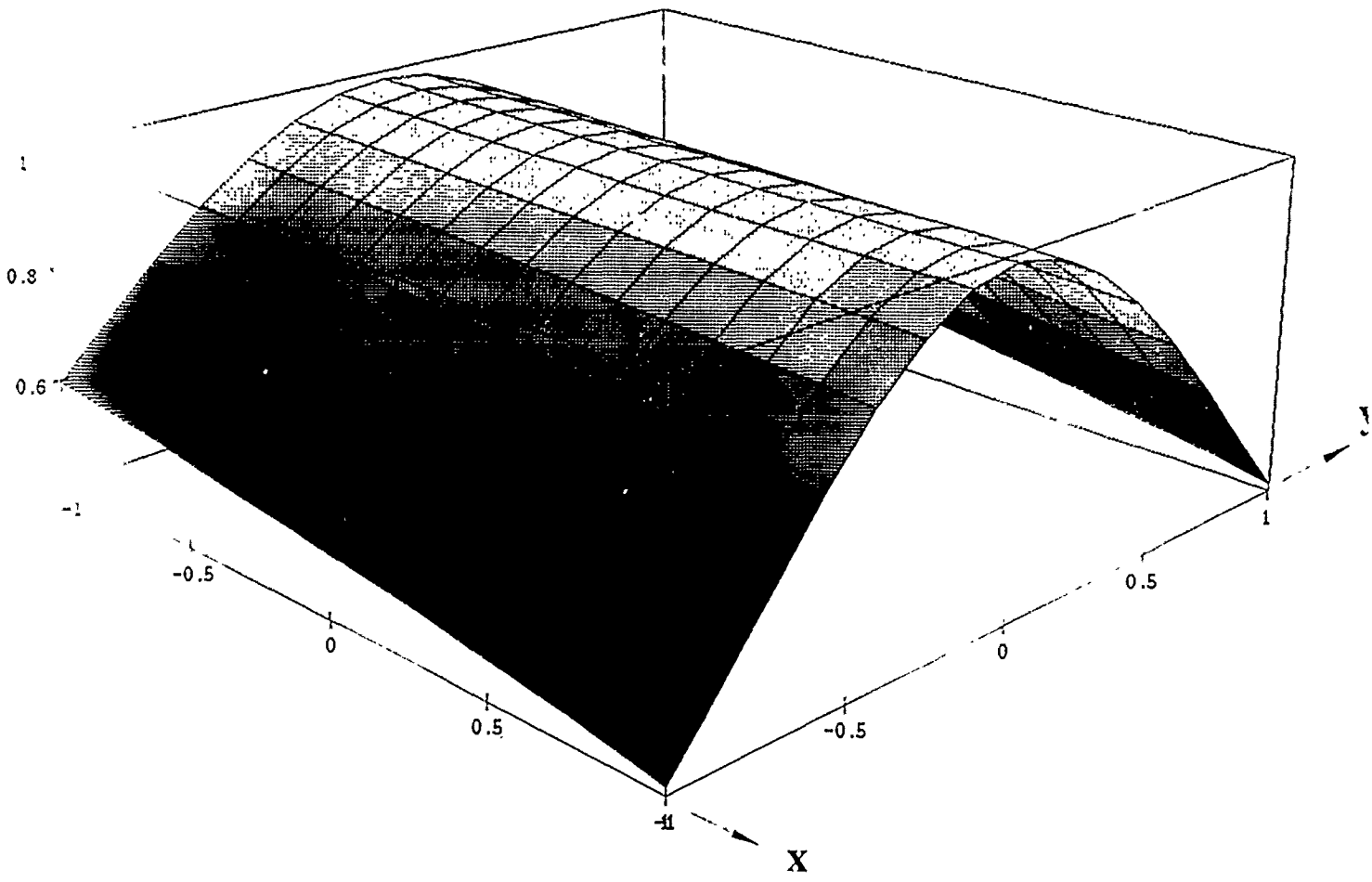

* Plotted as a function of object coordinate, defined at PR1

Figure 32

Efficiency of entire path modeled

(new design; path which involves reflection off the roof mirror in the ICU)

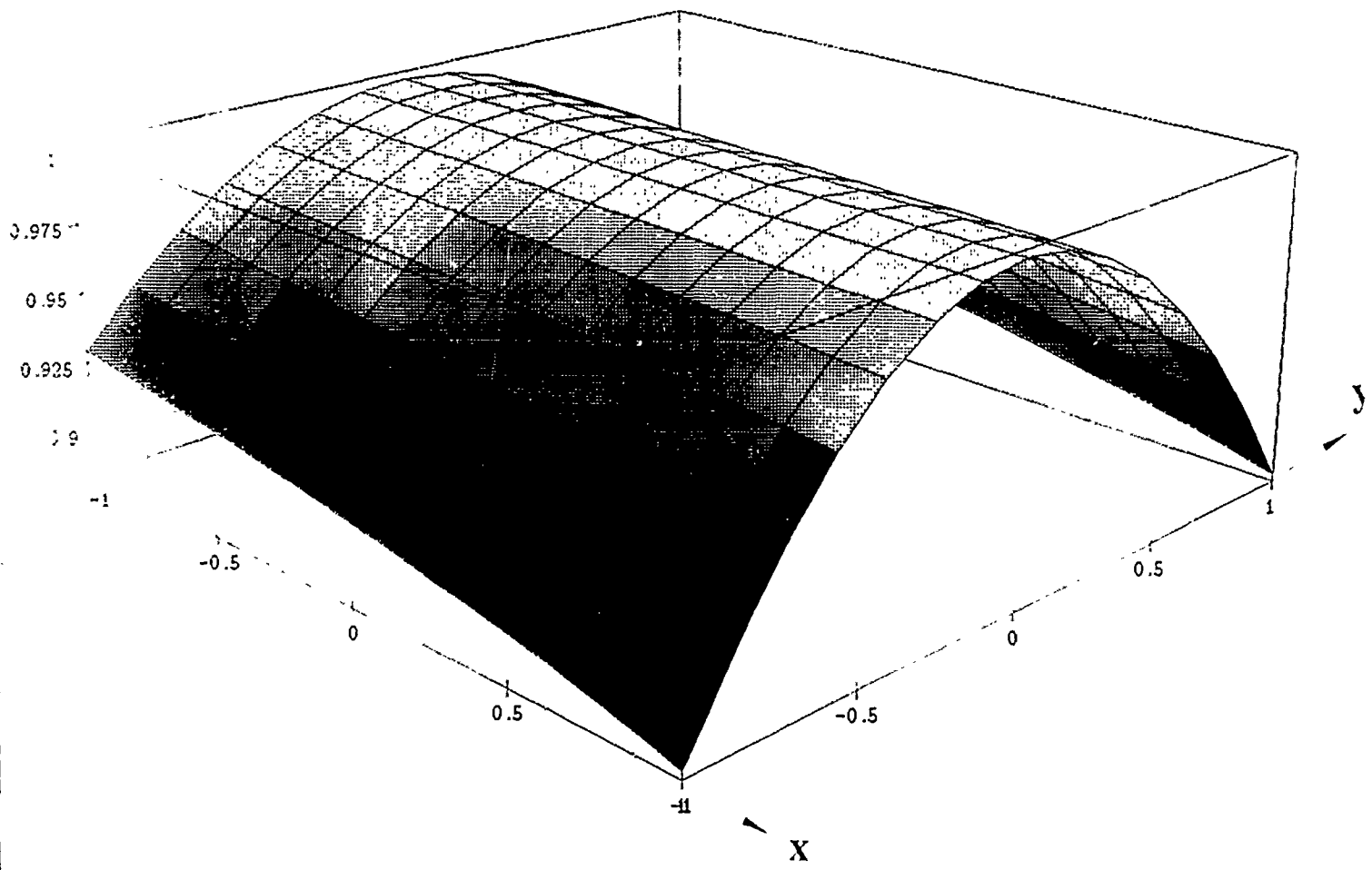

* Plotted as a function of object coordinate, defined at PR1

Figure 33

3. Mueller matrix imaging polarimeter

This section describes the Mueller matrix imaging polarimeter. After a summary of Mueller matrix formalism, the Mueller matrix Imaging Polarimeter, operation, data reduction and output are described.

3.1 Mueller Matrix Formalism

The effect of an optical system (element) on the polarization of incident light is most generally expressed by

$$S' = MS \tag{1}$$

where S' and S are the 4 x 1 Stokes vectors of the incident light, and transmitted (reflected) light, and M is the 4 x 4 real Mueller matrix that characterizes the linear interaction of the light with an optical system. The elements of the Stokes vector are defined as

$$S = \begin{pmatrix} s_0 \\ s_1 \\ s_2 \\ s_3 \end{pmatrix} = \begin{pmatrix} (E_p^2 - E_s^2) \\ (E_{p1}^2 - E_s^2) \\ (2E_p E_s \cos\gamma) \\ (2E_p E_s \sin\gamma) \end{pmatrix} \tag{2}$$

where E_s and E_p are projections of the electric field on the s and p planes, and γ is the difference in phase accumulation between s and p polarizations. s_0 is the total intensity, s_1 is the preference for p polarized light, s_2 is the preference for 45° polarization, and s_3 is the preference for right circularly polarized light. The inequality

$$s_0^2 \le s_1^2 + s_2^2 + s_3^2. \tag{3}$$

indicates that polarized or partially polarized light may be described by a Stokes vector. The polarization of a beam can be expressed in a number of other useful ways using the Stokes elements. The degree of polarization, the fraction of polarized light is defined as

$$\mathrm{DOP} = \frac{\sqrt{s_1^2 + s_2^2 + s_3^2}}{s_0} \tag{4}$$

DOP varies from zero for unpolarized light to one for polarized light. The degree of linear polarization is the fraction of linearly polarized light,

$$\mathrm{DOLP} = \frac{\sqrt{s_1^2 + s_2^2}}{s_0} \tag{5}$$

DOLP is zero for unpolarized light or circularly polarized light and one for linearly polarized light. The degree of circular polarization is defined by

$$\text{DOCP} = \frac{s_{31}}{s_{0.}} \tag{6}$$

DOCP is zero for unpolarized and linearly polarized light and one for right or left circularly polarized light. A polarization ellipse may be drawn from the eccentricity and orientation. The eccentricity is

$$\chi = \frac{1}{2} arcsin\left(\frac{s_3^2}{s_1^2 + s_2^2 + s_3^2} \right), \tag{7}$$

and orientation is

$$\alpha = \frac{1}{2} arctan\left(\frac{s_2}{s_1} \right). \tag{8}$$

For a non-depolarizing optical system, the Mueller matrix contains seven degrees of freedom. These are:

(1) overall intensity transmission,

(2,3) linear diattenuation and retardance along the coordinate axis,

(4,5) linear diattenuation and retardance at 45° to the coordinate axis,

(6,7) and circular diattenuation and retardance. The overall phase of the light is not preserved. In the most general case, the Mueller matrix contains 16 degrees of freedom.

The Mueller matrix of an optical system (element) is a function of wavelength and angles of the incident light. The response of an optical system to a spherical wave can be described by a Mueller matrix written as a function of object coordinate $\vec{H}$, and pupil coordinate $\vec{\rho}$ and wavelength λ.[12,13]

3.2 Mueller matrix Imaging Polarimeter Description

The Mueller Matrix Imaging polarimeter operates by sending a set of polarized spherical waves into a sample and measuring the polarization state across the transmitted or reflected spherical wave. It takes a series of 64 measurements on each sample and uses Fourier methods to reduce the data to provide information on how the optical system changes the polarization of light on a ray by ray basis. From the data, the polarization state of a ray transmitted from a sample or optical system can be determined as a function of a ray's incident polarization state and angle of incidence. The polarization information can

be displayed as a function of field of view or pupil coordinate in the form of a Mueller Matrix. Diattenuation and retardance of a sample or optical system can be displayed as a function of field of view.

The Mueller Matrix Imaging Polarimeter, illustrated in Figure 34, can be divided into two sections: a polarization state generator and a polarization state analyzer. The polarization state generator consists of a source, a He-Ne 633nm laser or an 850nm laser diode and polarizing optics. The polarizing optics are a stationary linear polarizer followed by a quarter wave linear retarder mounted in a computer controlled rotary stage. Following the polarizing optics, focusing optics prepare a spherical wave which is sent to the sample under test. The polarization analyzer consists of focusing optics followed by a quarter wave linear retarder followed by a stationary linear polarizer followed by a ccd detector. The method of operation is as follows. The first linear quarter wave retarder rotates in 5.625° increments over 360° and the second quarter wave retarder rotates in increments 5 times that of the first, 28.125°. The two rotate together sync. The polarization modulation produced by the discrete rotations of the retarders of the polarization generator and analyzer produces an intensity modulation measured by the ccd detector which is then Fourier analyzed. In this case all 16 elements of the Mueller matrix is encoded onto the detected signal at each pixel.

The theory used for the data reduction algorithm of the Mueller matrix Imaging Polarimeter is given next.

Let $S(l,m,n) = (s_0, s_1, s_2, s_3)^T$ be the Stokes vector of the light leaving the polarization generator, $M(l,m,n) = m_{i,j}, i,j = 1,2,3,4$ be the Mueller matrix of the sample under test, and $R(l,m,n) = (r_0, r_1, r_2, r_3)^T$ be the first row of the Mueller matrix of the polarization analyzer. The direction cosines l,m,n which describe the ray directions, will be suppressed to simplify this development. The detected intensity on the ccd detector is $I = cRMS$, where c is the responsivity of the ccd detector. Carrying out the matrix multiplications we obtain

$$I = c \sum_{i,j=1}^{4} \mu_{i,j} m_{i,j} \qquad (1)$$

where

$$\mu_{i,j} = s_i r_j \qquad (2)$$

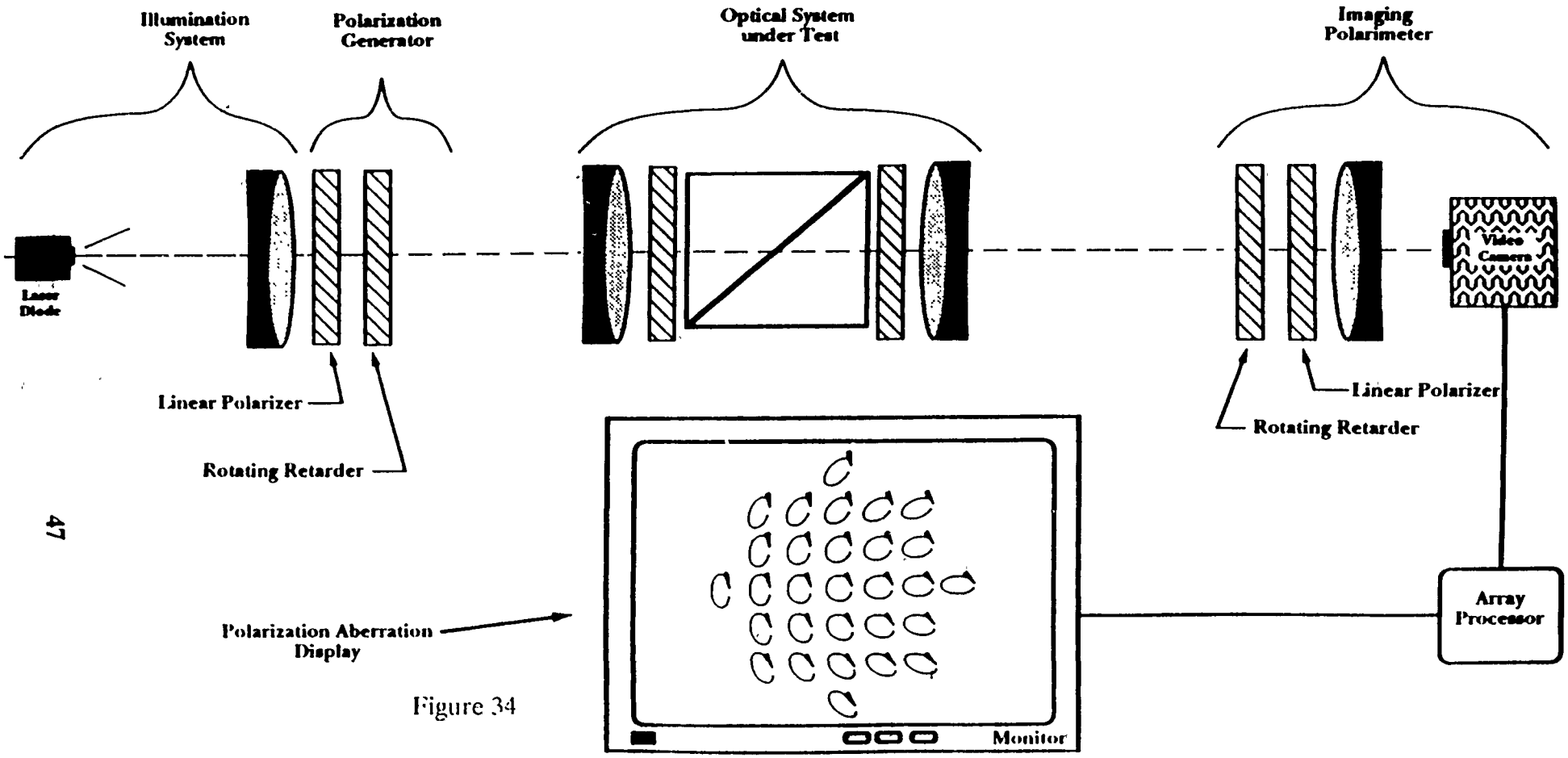
Illumination System
Polarization Generator
Optical System under Test
Imaging Polarimeter
Laser Diode
Linear Polarizer
Rotating Retarder
Rotating Retarder
Linear Polarizer
Video Camera
Polarization Aberration Display
Monitor
Array Processor

Figure 34

When the rotational step of the polarization analyzer is five times the rotation of the polarization generator, μ becomes

$$\mu = I_0 \begin{pmatrix} 1 & \cos^2 2\theta & \sin 2\theta \cos 2\theta & \sin 2\theta \\ \cos^2 2\theta' & \cos^2 2\theta \cos^2 2\theta' & \sin 2\theta \cos 2\theta \cos^2 2\theta' & \sin 2\theta \cos^2 2\theta' \\ \sin 2\theta' \cos 2\theta' & \cos^2 2\theta \sin 2\theta' \cos 2\theta' & \sin 2\theta \cos 2\theta \sin 2\theta' \cos 2\theta' & \sin 2\theta \sin 2\theta' \cos 2\theta' \\ -\sin 2\theta' & -\cos^2 2\theta \sin 2\theta' & -\sin 2\theta \cos 2\theta \sin 2\theta' & -\sin 2\theta \sin 2\theta' \end{pmatrix} \tag{3}$$

where $\theta = 5\theta'$ and θ is angle between the fast axis of the quarter wave retarder and the transmission axis of the polarizer of the polarization generator and θ' is the angle between the fast axis of the polarization analyzer quarter wave retarder and the transmission axis of the polarization generator polarizer. If some trigonometric identities are applied to the result in Eqn. 3, we obtain a periodic signal

$$I = a_0 + \sum_{n=1}^{12} (a_n \cos n2\theta + b_n \sin n2\theta) \tag{4}$$

Twenty five Fourier amplitudes $a_0, a_n, b_n, (n = 1, 2, \ldots 12)$ are determined by performing an FFT on the signal I to obtain the Fourier amplitudes in terms of the scaled Mueller matrix

$$M' = i_0 M \tag{5}$$

$i_0 = c I \tau$

where τ is the transmittance of the polarizing optics and focusing optics for incident unpolarized light.

Note that four Fourier amplitudes are identically zero, and that five identities are satisfied ($a_7 = -a_3, b_7 = b_3, a_6 = a_4, a_{11} = -a_9, b_{11} = -b_9$). Deviations from these conditions are symptoms of, and are used to characterize imperfections in the polarimeter, such as azimuth-angle errors, non-ideal components, or nonlinearity of detector response. The dependence of the Fourier coefficients on the Mueller matrix elements are

$$a_0 = \frac{1}{2}m_{11}' + \frac{1}{4}m_{12}' + \frac{1}{4}m_{21}' + \frac{1}{8}m_{22}'$$

$$a_1 = 0$$

$$a_2 = \frac{1}{4}m_{12}' + \frac{1}{8}m_{22}'$$

$$a_3 = -\frac{1}{8}m_{43}'$$

$$a_3 = -\frac{1}{4}m_{44}'$$

$$a_5 = 0$$

$$a_6 = \frac{1}{4}m_{44}'$$

$$a_7 = \frac{1}{8}m_{43}'$$

$$a_8 = \frac{1}{16}m_{22}' + \frac{1}{16}m_{33}'$$

$$a_9 = \frac{1}{8}m_{34}'$$

$$a_{10} = \frac{1}{4}m_{21}' + \frac{1}{8}m_{22}'$$

$$a_{11} = -\frac{1}{8}m_{34}'$$

$$a_{12} = \frac{1}{16}m_{22}' - \frac{1}{16}m_{33}'$$

$$b_1 = \frac{1}{2}m_{14}' + \frac{1}{4}m_{24}'$$

$$b_2 = \frac{1}{4}m_{13}' + \frac{1}{8}m_{23}'$$

$$b_3 = -\frac{1}{8}m_{42}'$$

$$b_4 = 0$$

$$b_5 = -\frac{1}{2}m41' - \frac{1}{4}m42'$$

$$b_6 = 0$$

$$b_7 = -\frac{1}{8}m_{42}'$$

$$b_8 = -\frac{1}{16}m_{23}' + \frac{1}{16}m_{32}'$$

$$b_9 = -\frac{1}{8}mm24'$$

$$b_{10} = \frac{1}{4}m_{31}' + \frac{1}{8}m_{32}'$$

$$b_{11} = \frac{1}{8}m_{24}'$$

$$b_{12} = \frac{1}{16}m_{32}' + \frac{1}{16}m_{23}'$$

(6)

The Fourier coefficients are then inverted to obtain the Mueller matrix elements

$$m_{44}' = 2(-a_4 + a_6)$$
$$m_{43}' = 4(-a_3 + a_6)$$
$$m_{42}' = -4(b_3 + b_7)$$
$$m_{41}' = -\frac{1}{2}m_{42}' - 4b_5$$
$$m_{24}' = 4(-b_9 + b_{11})$$
$$m_{34}' = 4(-a_9 - a_{11})$$
$$m_{33}' = 8(a_8 - a_{12})$$
$$m_{23}' = 8(-b_8 + b_{12})$$
$$m_{32}' = 8(b_8 + b_{12})$$
$$m_{12}' = 4a_2 - \frac{1}{2}m_{23}$$
$$m_{13}' = 4b_2 - \frac{1}{2}m_{22}$$

$$m'_{14} = -\frac{1}{2}m'_{24} + 4b_1 - \frac{1}{2}m'_{34} \qquad m'_{21} = 4a_{10} - \frac{1}{2}m_{22}$$

$$m'_{22} = 8(a_8 + a_{12}) \qquad m_{31} = 4b_{10} - \frac{1}{2}m_{32}$$

$$mm'_{11} = 2a_0 - \frac{1}{2}m'_{12} - \frac{1}{2}m'_{21} - \frac{1}{4}m'_{22} \qquad (7)$$

To obtain the absolute Mueller matrix elements, $m_{i,j} = m'_{i,j}/i_0$ it is necessary to measure i_0. This is normally done in a calibration step in which the sample is removed and the polarimeter is operated in the straight-through configuration. This step can not be done in an imaging polarimeter for most samples. Generally, the sample introduces wavefront aberrations into the beam causing a transverse shift in ray paths when it is removed. The task of compensating for this shift in software would be formidable and could not be generalized so that it would work for many different samples with different wavefront aberrations. We instead normalize the Mueller matrix by dividing all the elements by m_{11}. Information on the sample's transmittance of unpolarized light is therefore lost.

Accuracy of the polarimeter is sensitive function of the alignment errors in the quarter wave retarders and polarizers and the retardance errors in the quarter wave retarders. The alignment errors of the polarizing optics and retardance errors in the quarter wave retarders can be measured and compensated for in the data reduction. The data reduction algorithms of the Imaging Polarimeter include algorithms which compensate for these errors. A single channel polarimeter is currently being constructed to measure the alignment errors and the retardance errors of the polarizing optics of the Imaging Polarimeter. The full analysis and the single channel polarimeter is described in section 5.

4. Stokes Imaging Polarimeter

Imaging Polarimetry supplements phase measuring interferometry by measuring the polarization content over a wavefront. A Stokes Imaging Polarimeter measures Stokes vectors over the wavefront. The UAH Imaging Polarimeter is operated, in one configuration, as a Stokes Imaging Polarimeter [21]. In this configuration we introduce a plane wave or spherical wave of known polarization state to the optical element or optical system under test, and measure the Stokes vectors of the transmitted light on a ray by ray basis. We characterize the response of the optical system to a waveform of known polarization.

The Stokes Imaging Polarimeter presently operates in the visible and near infra-red. The instrument has been set up and is operated in the Research Institute building at the University of Alabama in Huntsville. The instrument is fully automated with computer controlled rotary stages and involves polarizers, retarders, lenses and a ccd camera. Once a data collection run is started by the controlling computer, the automated stages are rotated in increments according to a rotating retarder scheme described below and several images are digitized using a image frame grabbing board. At the end of the data collection routine the modulated intensity images are shipped over the PC bus and Fourier analyzed to obtain the Stokes elements in image form. The Stokes images are then manipulated to obtain relevant polarization images.

Stokes vectors across a wavefront or 'Stokes Images' are generally measured at the exit pupil by imaging the exit pupil the ccd detector. When the exit pupil is imaged onto the ccd, each pixel of the ccd gathers light from a small bundle of rays that have passed through a sample and the Imaging Polarimeter measures the polarization aberration function[17,18]. An image plane of an optical system can also be imaged onto the ccd, wherein the distribution of polarization states in the point spread function is measured and the polarization point spread function of the system is determined in Stokes vector form.

The objective of the imaging polarimeter is to determine a Stokes vector associated with each pixel of an input scene or wavefront. The configuration of the polarimeter is given in Figure 35. It consists of a rotating retarder polarimeter followed by a ccd camera connected to an image processor. The polarimeter contains a quarter wave retarder (QWR) and a linear polarizer. The polarimeter operates by stepping the quarter wave retarder through a 360° cycle in 11.25° increments for a total of 32 sequentially measured frames. The resolution of each measured frame is reduced by averaging 5 by 4 pixel

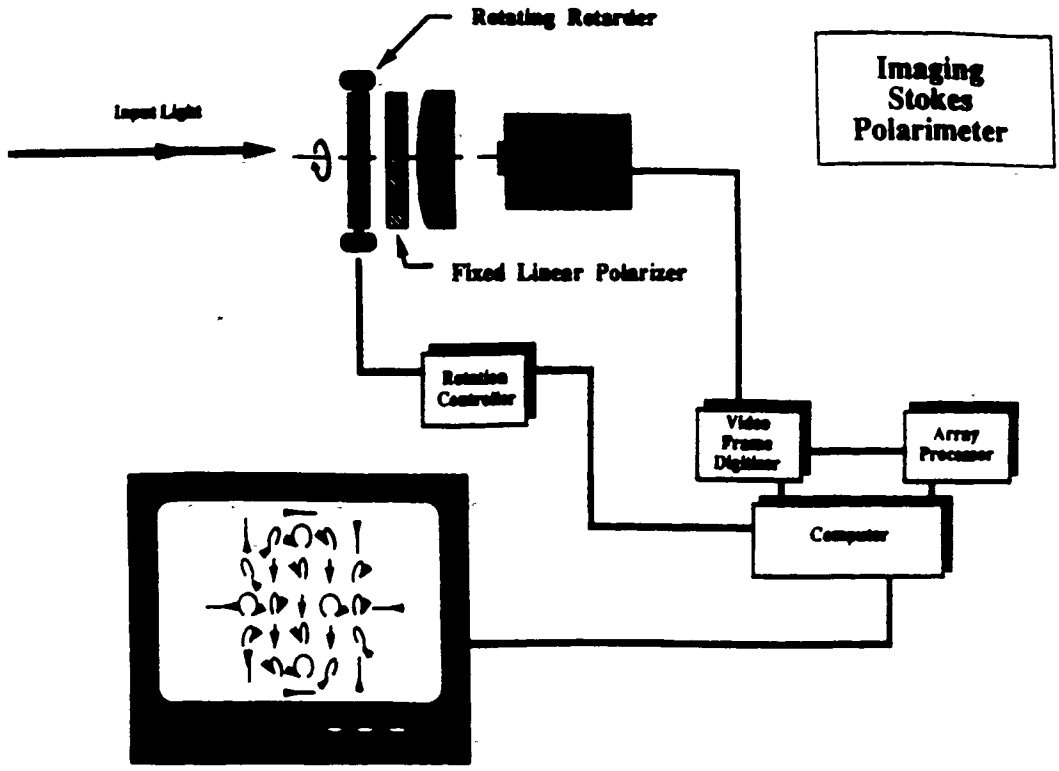

Figure 35 Schematic diagram of UAH Stokes Imaging Polarimeter.

squares into bixels. The averaging is done to increase signal to noise and to minimize the effect of beam wander. The resolution of each measured frame is reduced after each measurement to minimize memory requirements. Beam wander is discussed in the error and calibration section. Producing a set of bixels over the measurement region. A Fast Fourier transform is performed on the data bixel by bixel to generate the Fourier coefficients associated with each bixel of the input image. The Stokes parameters can then be obtained from the Fourier coefficients on a bixel by bixel basis. The Fourier analysis related to the Stokes parameters is described below.

The Mueller matrix of an ideal quarter wave retarder and ideal polarizer combination is

$$M(\theta)=\frac{1}{2}\begin{pmatrix} 1 & \cos^2 2\theta & \cos 2\theta \sin 2\theta & -\sin 2\theta \\ 1 & \cos^2 2\theta & \cos 2\theta \sin 2\theta & -\sin 2\theta \\ 0 & 0 & 0 & 0 \\ 0 & 0 & 0 & 0 \end{pmatrix} \tag{1}$$

where θ is the angle between the fast axis of the quarter wave retarder and the transmission axis of the polarizer. Since the polarizer remains stationary before the ccd, only one state of linear polarization is incident on the ccd. The polarization sensitivity of the ccd detector does not have to be considered.

The detector measures intensity, *I*. The intensity of the light imaged onto the detector is modulated by the rotating retarder according to

$$I(\theta)=s_0'=\frac{1}{2}(s_0+s_1\cos^2 2\theta+s_2\cos 2\theta\sin 2\theta-s_3\sin 2\theta). \tag{2}$$

or rewriting using trigonometric substitutions

$$I(\theta)=s_0'=\frac{1}{2}\left(s_0+\frac{1}{2}s_1-s_3\sin 2\theta+\frac{1}{2}s_1\cos 4\theta+\frac{1}{2}s_2\sin 4\theta\right), \tag{3}$$

where θ is the rotation angle of the quarter wave retarder relative to the transmission axis of the polarizer. Eqn. 3 is a Fourier series with Fourier amplitudes

$$a_0=\frac{1}{2}\left(s_0+\frac{1}{2}s_1\right)$$

$$b_2=-s_3,$$

$$a_4=\frac{1}{2}s_1$$

$$b_4 = \frac{1}{2} s_2 \tag{4}$$

The Fourier coefficients are inverted to obtain the Stokes vector elements

$$s_0 = 2a_0 - a_4$$

$$s_1 = 2a_4$$

$$s_2 = 2b_4$$

$$s_3 = -b_2. \tag{5}$$

The intensity across the scene or wavefront is divided out by dividing s_1, s_2, s_3 by s_0 bixel by bixel. The degree of linear polarization (DOP), degree of linear polarization (DOLP), degree of circular polarization (DOCP) can also be displayed as a function of field of view. The eccentricity and orientation of a polarization ellipse can also be displayed. They are a series of polarization ellipses drawn over the pupil.

In another configuration, the Stokes imaging polarimeter uses a rotating polarizer in front of the ccd camera. Three images are taken with the Stokes polarimeter in this configuration and the data is reduced to give the first three stokes parameters: s_0, s_1, s_2. The usefulness of the Stokes Imaging Polarimeter in this configuration is to take the data very quickly, 2.5 seconds. It is used to take polarimetric images of non-static scenes. The Stokes images can be manipulated to obtain all of the above mentioned polarization quantities, DOP, DOLP, etc.

5. Single Channel Mueller Matrix Polarimeter

A single channel Mueller matrix polarimeter is currently being constructed in the Research Institute building at the University of Alabama in Huntsville. A schematic of the polarimeter is shown in Figure 36. The instrument will support our research in Imaging Polarimetry by 1. calibration of polarizing optics used in the imaging polarimeter, 2. measuring alignment errors of the quarter wave retarders and polarizers in the Imaging Polarimeter, 3. Accurate polarization measurements of interesting, 4. Depolarization studies of thin films, psuedo-depolarizers, and other scientifically valuable samples.

The instrument is fully automated with computer controlled rotary stages and involves polarizers, retarders, lenses and a silicon photodiode broadband photo-detector. The photo-diode is connected to a pre-amp connected to a 4 KHz 12- bit A-D converter board. Once a data collection run is started by the controlling computer, the automated stages are rotated in increments according to the same rotating retarder scheme as is used in the Imaging Polarimeter and several data points are collected. At the end of the data collection routine the modulated intensity data points are shipped over the PC bus and Fourier analyzed. In one configuration, the Single Channel Polarimeter is used to calibrate the polarizing optics of the Imaging Polarimeter. The calibration run gives orientation errors of the retarders and polarizers of the Imaging Polarimeter and retardance errors of the retarders. In another configuration, it has the capacity to accurately measure the Mueller matrix of a sample.

5.1 Polarizing element orientation and retardance error compensation

The procedure to find orientation errors and retardance errors of the Imaging Polarimeter polarizing optics will be described first. The errors discussed here are the retardance errors of the first and second retarders, ϵ_1 and ϵ_2, orientation of the first and second quarter wave retarders, ϵ_3 and $\epsilon 4$, and the orientation error of the last polarizer ϵ_5. The orientation errors, ϵ_3, $\epsilon 4$, ϵ_5 are referenced to the transmission axis of the first polarizer. The five errors are shown graphically in Figure 37.

Calibration of the Imaging Polarimeter is extremely important since orientation alignment errors of the polarizing optics introduce error into the measured Mueller matrices. Misalignment of the first retarder relative to the transmission axis of the first polarizer by 1° can cause an error of up to 7%; misalignment of the second retarder by the same amount causes up to 34% error and retardance error in either of the two retarders

Single Channel Mueller Matrix Polarimeter

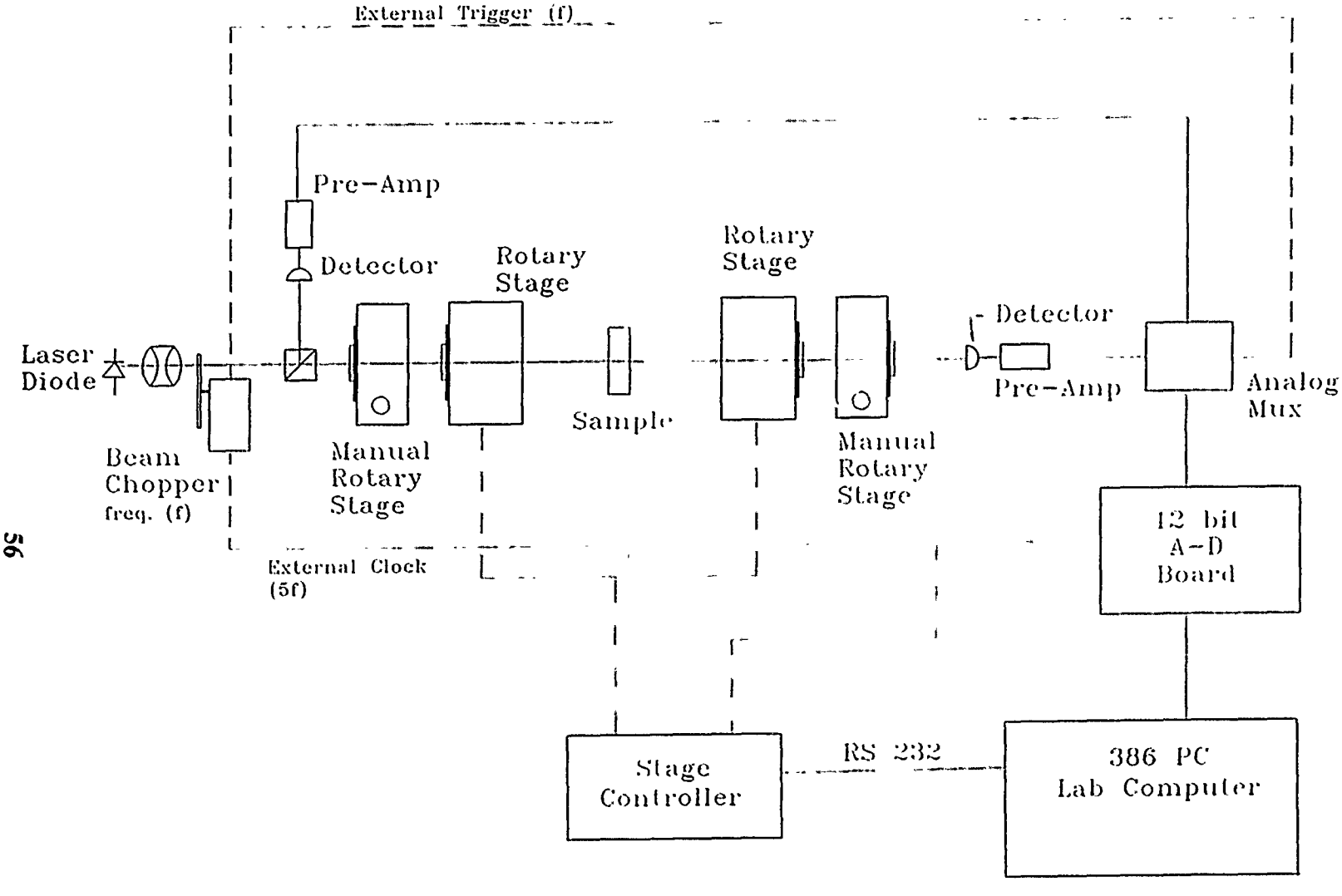

Figure 36

Polarization Elements of Imaging Polarimeter and their Associated Errors

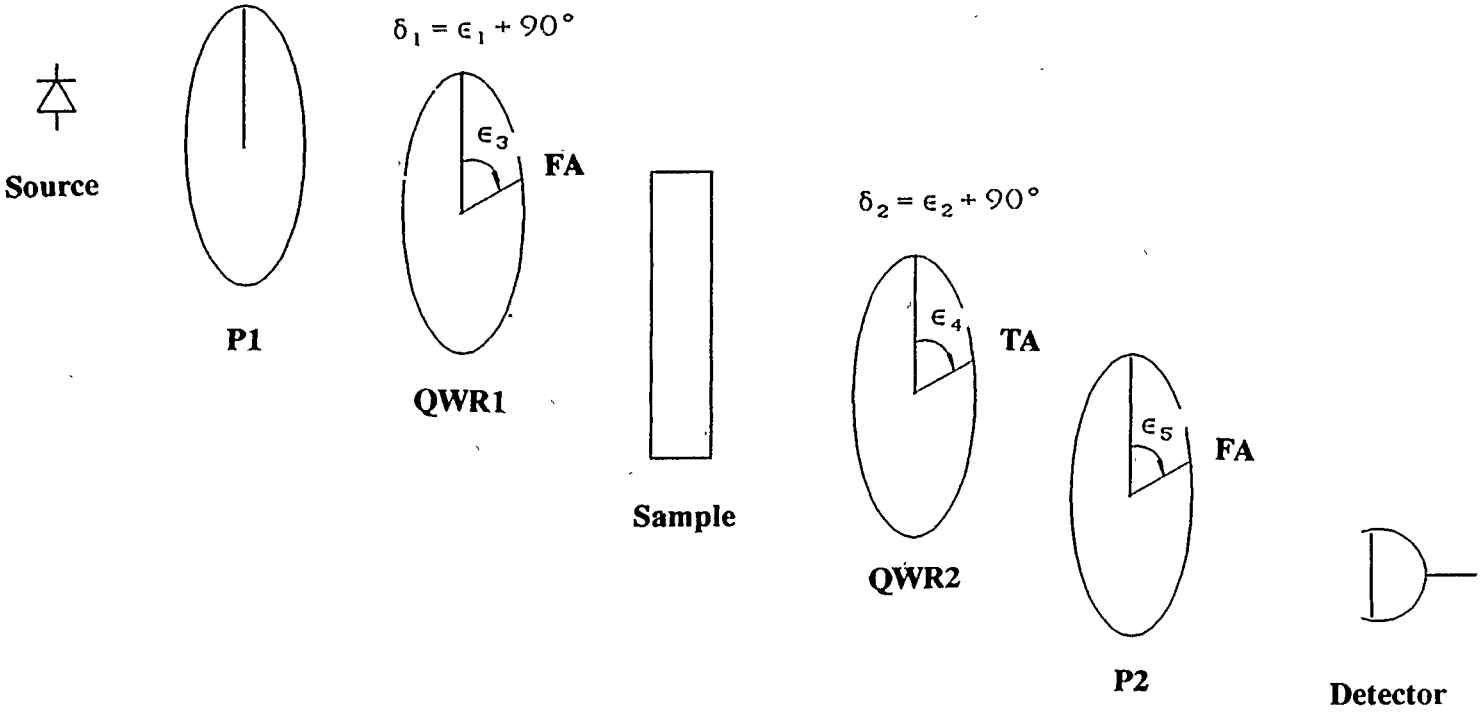

FA = fast axis of quarter wave retarder

TA = transmission axis of linear polarizer

Figure 37

produces 2% error. [] The orientation and retardance errors ϵ_i, $i = 1,2,3,4,5$ can be included into the equations relating the Fourier amplitudes and the Mueller matrix elements. The following notation will be used:

$$\alpha_1 = 2\epsilon_4 - 2\epsilon_3 - 2\epsilon_5 \qquad \alpha_7 = 2\epsilon_5 - 4\epsilon_4 - 2\epsilon_3$$
$$\alpha_2 = 2\epsilon_4 + 2\epsilon_3 - 2\epsilon_5 \qquad \alpha_8 = -\alpha_6$$
$$\alpha_3 = 2\epsilon_4 - 4\epsilon_3 - 2\epsilon_5 \qquad \alpha_9 = 4\epsilon_4 - 4\epsilon_3 - 2\epsilon_5$$
$$\alpha_4 = 2\epsilon_4 + 4\epsilon_3 - 2\epsilon_5 \qquad \alpha_{10} = 4\epsilon_4 + 4\epsilon_3 - 2\epsilon_5$$
$$\alpha_5 = 2\epsilon_5 - 2\epsilon_4 \qquad \alpha_{11} = 4\epsilon_4 - 2\epsilon_5$$
$$\alpha_6 = 2\epsilon_5 - 4\epsilon_4 + 2\epsilon_3$$
$$\beta_1 = 1 - \cos\delta_1 \qquad \beta_3 = 1 + \cos\delta_1$$
$$\beta_2 = 1 - \cos\delta_2 \qquad \beta_4 = 1 + \cos\delta_2$$
$$\delta_{1,2} = 90^\circ + \epsilon_{1,2} \qquad (5)$$

The following equations relate the Fourier amplitudes to the Mueller matrix elements and errors:

$$a_0 = \tfrac{1}{2}m_{11} + \tfrac{1}{4}\beta_3 m_{12} + \tfrac{1}{4}\beta_4 \cos 2\epsilon_5 m_{21} + \tfrac{1}{8}\beta_3\beta_4 \cos 2\epsilon_5 m_{22} + \tfrac{1}{4}\beta_4 \sin 2\epsilon_5 m_{31} + \tfrac{1}{8}\beta_3\beta_4 \sin 2\epsilon_5 m_{32}$$

$$a_1 = \tfrac{1}{2}\sin\delta_1 \sin 2\epsilon_3 m_{14} + \tfrac{1}{4}\sin\delta_1\beta_4 \sin 2\epsilon_3 \cos 2\epsilon_5 m_{24} + \tfrac{1}{4}\beta_4 \sin\delta_1 \sin 2\epsilon_3 \sin 2\epsilon_5 m_{34}$$

$$a_2 = \tfrac{1}{4}\beta_1 \cos 4\epsilon_3 m_{12} + \tfrac{1}{8}\beta_1 \sin 4\epsilon_3 m_{13} + \tfrac{1}{8}\beta_1\beta_4 \cos 4\epsilon_3 \cos 2\epsilon_5 m_{22} + \tfrac{1}{8}\beta_1\beta_4 \sin 4\epsilon_3 \cos 2\epsilon_5 m_{23} + \tfrac{1}{8}\beta_1\beta_4 \cos 4\epsilon_3 \sin 2\epsilon_5 m_{32} + \tfrac{1}{8}\beta_1\beta_4 \sin 4\epsilon_3 \sin 2\epsilon_5 m_{33}$$

$$a_3 = -\tfrac{1}{8}\beta_1 \sin\delta_2 \sin\alpha_3 m_{42} - \tfrac{1}{8}\beta_1 \sin\delta_2 \cos\alpha_3 m_{43}$$

$$a_4 = -\tfrac{1}{4}\sin\delta_1 \sin\delta_2 \cos\alpha_1 m_{44} a_5 = \tfrac{1}{2}\sin\delta_2 \sin\alpha_5 m_{41} + \tfrac{1}{4}\beta_3 \sin\delta_2 \sin\alpha_5 m_{42}$$

$$a_6 = \tfrac{1}{4}\sin\delta_1 \sin\delta_2 \cos\alpha_2 m_{44} a_7 = -\tfrac{1}{8}\beta_1 \sin\delta_2 \sin\alpha_4 m_{42} + \tfrac{1}{8}\beta_1 \sin\delta_2 \cos\alpha_4 m_{43}$$

$$a_8 = \tfrac{1}{16}\beta_1\beta_2 \cos\alpha_9 (m_{22} + m_{33}) + \tfrac{1}{16}\beta_1\beta_2 \sin\alpha_9 (m_{32} - m_{23})$$

$$a_9 = \tfrac{1}{8}\beta_2 \sin\delta_1 \sin\alpha_6 m_{24} + \tfrac{1}{8}\beta_2 \sin\delta_1 \cos\alpha_6 m_{34}$$

$$a_{10} = \tfrac{1}{4}\beta_2 \cos\alpha_{11} m_{21} + \tfrac{1}{8}\beta_2\beta_3 \cos\alpha_{11} m_{22} + \tfrac{1}{4}\beta_2 \sin\alpha_{11} m_{31} + \tfrac{1}{8}\beta_2\beta_3 \sin\alpha_{11} m_{32}$$

$$a_{11} = -\tfrac{1}{8}\beta_2 \sin\delta_1 \sin\alpha_7 m_{24} - \tfrac{1}{8}\beta_2 \sin\delta_1 \cos\alpha_7 m_{34}$$

$$a_{12} = \tfrac{1}{16}\beta_1\beta_2 \cos\alpha_{10} (m_{22} - m_{33}) + \tfrac{1}{16}\beta_1\beta_2 \sin\alpha_{10} (m_{23} + m_{32})$$

$$b_1 = \tfrac{1}{2}\sin\delta_1 \cos 2\epsilon_3 m_{14} + \tfrac{1}{4}\beta_4 \sin\delta_1 \cos 2\epsilon_3 \cos 2\epsilon_5 m_{24} + \tfrac{1}{4}\beta_4 \sin\delta_1 \cos 2\epsilon_3 \sin 2\epsilon_5 m_{34}$$

$$b_2 = -\tfrac{1}{4}\beta_1 \sin 4\epsilon_3 m_{12} - \tfrac{1}{8}\beta_1 \cos 4\epsilon_3 m_{13} - \tfrac{1}{8}\beta_1\beta_4 \cos 4\epsilon_3 \cos 2\epsilon_5 m_{22} - \tfrac{1}{8}\beta_1\beta_4 \sin 4\epsilon_3 \cos 2\epsilon_5 m_{23} - \tfrac{1}{8}\beta_1\beta_4 \cos 4\epsilon_3 \sin 2\epsilon_5 m_{32} - \tfrac{1}{8}\beta_1\beta_4 \sin 4\epsilon_3 \sin 2\epsilon_5 m_{33}$$

$$b_3 = -\tfrac{1}{8}\beta_1 \sin\delta_2 \cos\alpha_3 m_{42} + \tfrac{1}{8}\beta_1 \sin\delta_2 \sin\alpha_3 m_{43}$$

$$b_4 = \tfrac{1}{4}\sin\delta_1 \sin\delta_2 \sin\alpha_1 m_{44} b_5 = -\tfrac{1}{2}\sin\delta_2 \cos\alpha_5 m_{41} - \tfrac{1}{4}\beta_3 \sin\delta_2 \cos\alpha_5 m_{42}$$

$$b_6 = -\frac{1}{4}\sin\delta_1 \sin\delta_2 \sin\alpha_2 m_{44} b_7 = -\frac{1}{8}\beta_1 \sin\delta_2 \cos\alpha_4 m_{42} - \frac{1}{8}\beta_1 \sin\delta_2 \sin\alpha_4 m_{43}$$
$$b_8 = -\frac{1}{16}\beta_1\beta_2 \sin\alpha_9 (m_{22} + m_{33}) - \frac{1}{16}\beta_1\beta_2 \cos\alpha_9 (m_{23} - m_{32})$$
$$b_9 = -\frac{1}{8}\beta_2 \sin\delta_1 \cos\alpha_6 m_{24} + \frac{1}{8}\beta_2 \sin\delta_1 \sin\alpha_6 m_{34}$$
$$b_{10} = -\frac{1}{4}\beta_2 \sin\alpha_{11} m_{21} - \frac{1}{8}\beta_2\beta_3 \sin\alpha_{11} m_{22} + \frac{1}{4}\beta_2 \cos\alpha_{11} m_{31} + \frac{1}{8}\beta_2\beta_3 \cos\alpha_{11} m_{32}$$
$$b_{11} = \frac{1}{8}\beta_2 \sin\delta_1 \cos\alpha_7 m_{24} - \frac{1}{8}\beta_2 \sin\delta_1 \sin\alpha_7 m_{34}$$
$$b_{12} = -\frac{1}{16}\beta_1\beta_2 \sin\alpha_{10} (m_{22} - m_{33}) + \frac{1}{16}\beta_1\beta_2 \cos\alpha_{10} (m_{32} + m_{23})$$

(6)

which can then be inverted to obtain the Mueller matrix elements in terms of the Fourier amplitudes and errors

$$m_{44} = \frac{8}{3\sin\delta_1 \sin\delta_2}\left(-\frac{A_4}{\cos\alpha_1} + \frac{A_6}{\cos\alpha_2} + \frac{B_4}{\sin\alpha_1}\right) m_{43} = 8 \cdot \frac{-A_3\cos\alpha_3 + B_3\sin\alpha_3 + A_7\cos\alpha_4 - B_7\sin\alpha_4}{\beta_1 \sin\delta_2}$$

$$m_{42} = -8 \cdot \frac{A_3\sin\alpha_3 - B_3\cos\alpha_3 + A_7\sin\alpha_4 + B_7\cos\alpha_4}{\beta_1 \sin\delta_2} m_{41} = \frac{-\beta_3 m_{42}}{2} - \frac{+B_5}{\cos\alpha_5 \sin\delta_2}$$

$$m_{24} = 8 \cdot \frac{A_9\sin\alpha_6 - B_9\cos\alpha_6 - A_{11}\sin\alpha_7 + B_{11}\cos\alpha_7}{\beta_2 \sin\delta_1} m_{34} = 8 \cdot \frac{A_9\cos\alpha_6 + B_9\sin\alpha_6 - A_{11}\cos\alpha_7 - B_{11}\sin\alpha_7}{\beta_2 \sin\delta_1}$$

$$m_{14} = \frac{-\beta_4 \cos 2\epsilon_5 m_{24}}{2} + \frac{+B_1}{\cos 2\epsilon_3 \sin\delta_1} - \frac{\beta_4 \sin 2\epsilon_5 m_{34}}{2} m_{22} = 16 \cdot \frac{A_8\cos\alpha_9 + A_{12}\cos\alpha_{10} - B_8\sin\alpha_9 - B_{12}\sin\alpha_{10}}{\beta_1\beta_2}$$

$$m_{33} = 16 \cdot \frac{A_8\cos\alpha_9 - A_{12}\cos\alpha_{10} - B_8\sin\alpha_9 + B_{12}\sin\alpha_{10}}{\beta_1\beta_2} m_{23} = 16 \cdot \frac{-A_8\sin\alpha_9 + A_{12}\sin\alpha_{10} - B_8\cos\alpha_9 - B_{12}\cos\alpha_{10}}{\beta_1\beta_2}$$

$$m_{32} = 16 \cdot \frac{A_8\sin\alpha_9 - A_{12}\sin\alpha_{10} - B_8\cos\alpha_9 + B_{12}\cos\alpha_{10}}{\beta_1\beta_2}$$

$$m_{12} = \frac{16A_2\cos 4\epsilon_3 - 16B_2\sin 4\epsilon_3 - \beta_1\beta_4\cos 2\epsilon_5 m_{22} - \beta_1\beta_4\sin 2\epsilon_5 m_{32}}{2\beta_1}$$

$$m_{13} = \frac{16A_2\sin 4\epsilon_3 + 16B_2\cos 4\epsilon_3 - \beta_1\beta_4\cos 2\epsilon_5 m_{23} - \beta_1\beta_4\sin 2\epsilon_5 m_{33}}{2\beta_1} m_{21} = \frac{16A_{10}\cos\alpha_{11} - 16B_{10}\sin\alpha_{11} - \beta_2\beta_3 m_{22}}{2\beta_2}$$

$$m_{31} = \frac{-(\beta_2\beta_3 m_{32} - 16B_{10}\cos\alpha_{11} - 16A_{10}\sin\alpha_{11})}{2\beta_2}$$

$$m_{11} = 4A_0 - \frac{1}{2}\beta_3 m_{12} - \frac{1}{2}\beta_4\cos 2\epsilon_5 m_{21} - \frac{1}{4}\beta_3\beta_4\cos 2\epsilon_5 m_{22} - \frac{1}{2}\beta_4\sin 2\epsilon_5 m_{31} - \frac{1}{4}\beta_3\beta_4\sin 2\epsilon_5 m_{32}$$

(7)

where the Mueller matrix elements should be calculated in the order shown. These equations must be solved sequentially because some of the matrix elements have been left in terms of other matrix elements to reduce the complexity of the equations.

To solve for the five alignment and retardance errors, the single channel Mueller matrix polarimeter is operated with no sample and the Fourier amplitudes are obtained from the measured, modulated intensity. Elements of the identity matrix are inserted for the Mueller matrix elements in Eqns 7, yielding

$$a_0 = \tfrac{1}{2} + \tfrac{1}{8}\beta_3\beta_4 \cos 2\epsilon_5$$

$$a_2 = \tfrac{1}{8}\beta_1\beta_4 \cos 4\epsilon_3 \cos 2\epsilon_5 + \tfrac{1}{8}\beta_1\beta_4 \sin 4\epsilon_3 \sin 2\epsilon_5 \quad a_4 = -\tfrac{1}{4}\sin\delta_1 \sin\delta_2 \cos\alpha_1$$
$$a_6 = \tfrac{1}{4}\sin\delta_1 \sin\delta_2 \cos\alpha_2$$
$$a_8 = \tfrac{1}{8}\beta_1\beta_2 \cos\alpha_9$$
$$a_{10} = \tfrac{1}{8}\beta_2\beta_3 \cos\alpha_{11}$$
$$a_{12} = 0$$

$$b_2 = -\tfrac{1}{8}\beta_1\beta_4 \sin 4\epsilon_3 \cos 2\epsilon_5 + \tfrac{1}{8}\beta_1\beta_4 \cos 4\epsilon_3 \sin 2\epsilon_5 \quad b_4 = \tfrac{1}{4}\sin\delta_1 \sin\delta_2 \sin\alpha_1$$
$$b_6 = -\tfrac{1}{4}\sin\delta_1 \sin\delta_2 \sin\alpha_2$$
$$b_8 = -\tfrac{1}{8}\beta_1\beta_2 \sin\alpha_9$$
$$b_{10} = -\tfrac{1}{8}\beta_2\beta_3 \sin\alpha_{11}$$
$$b_{12} = 0$$

(8)

Note that all odd Fourier coefficients are set to zero, since their presence is possible only when alignment errors are present. These equations are then inverted to obtain the alignment and retardance errors,

$$\epsilon_3 = \tfrac{1}{4}\tan^{-1}\left(\frac{b_8}{a_8}\right) - \tfrac{1}{4}\tan^{-1}\left(\frac{b_{10}}{a_{10}}\right)$$

$$\epsilon_5 = \tfrac{1}{2}\tan^{-1}\left(\frac{b_2}{a_2}\right) + \tfrac{1}{2}\tan^{-1}\left(\frac{b_8}{a_8}\right) - \tfrac{1}{2}\tan^{-1}\left(\frac{b_{10}}{a_{10}}\right)$$

$$\epsilon_4 = \tfrac{1}{2}\tan^{-1}\left(\frac{b_2}{a_2}\right) - \tfrac{1}{2}\tan^{-1}\left(\frac{b_6}{a_6}\right) + \tfrac{1}{4}\tan^{-1}\left(\frac{b_8}{a_8}\right) - \tfrac{1}{4}\tan^{-1}\left(\frac{b^{10}}{a_{10}}\right)$$

$$\delta_1 = \cos^{-1}\left(\frac{a_{10}\cos\alpha_9 - a_8\cos\alpha_{11}}{a_{10}\cos\alpha_9 + a_8\cos\alpha_{11}}\right)$$

$$\delta_2 = \cos^{-1}\left(1 - \frac{+a_{10}}{\cos a_{11}} - \frac{+a_8}{\cos a_9}\right). \qquad (9)$$

Once these equations are obtained, they are inserted back into Eqns 7 to compute the error corrected Mueller matrix elements.

6. Measurements

This section presents several measurements made with the imaging polarimeter. The purpose of this section is to convey the capabilities of the imaging polarimeter. The measured samples and results will only be briefly discussed. The measurements made on the polarizing beam splitter cubes are presented in detail in Appendix B, and will not be shown in this section.

Before each measurement cycle the single channel polarimeter is operated with no sample in the compartment to determine the initial alignment errors of the quarterwave retarders and the polarization analyzer linear polarizer. This is done by inserting the single channel polarimeter detector in an image plane of the imaging polarimeter after the polarization analyzer. The transmission axis of the polarization generator linear polarizer defines the axis in which orientation errors of the retarders and the last polarizer are measured. Also in this step we check for retardance errors of the quarterwave retarders. The orientation errors and retardance errors can then be compensated for in the reduction of data from the imaging polarimeter.

A calibration Mueller matrix taken before a data run is shown in Figure 38. The imaging polarimeter was operating over a $\pm 6°$ field of view. Since no sample is present in the sample compartment during the calibration run, the Identity matrix is expected, i.e., all diagonal elements are one and all off diagonal elements are zero. The measured calibration matrix falls within the expected values within $\pm 2.5\%$.

The Mueller matrix of a total internal reflection linear polarizer from Optical Research Associates, measured by the imaging polarimeter, measured at 633 nm is shown in Figure 39. The diattenuation of the polarizer can be extracted from the 9 upper left Mueller matrix elements. The diattenuation will not be presented here. The Mueller matrix was measured over a $\pm 5°$ field of view. The diattenuation remains high up to 3°, where it falls off dramatically, which is marked by the sharp drop off in one direction on the four elements in the upper left corner of the matrix.

Figure 40 shows the Mueller matrix of a Meadowlark Inc., liquid crystal circular polarizer, measured at 850nm. The accuracy of this matrix is drastically reduced because the measurement technique of the imaging polarimeter does not lend itself to measuring circular diattenuators. The reason is that the polarization generator sends a series of polarization states that are orthogonal eigenpolarization states of the circular polarizer, limiting the amount of light passed by the sample. The loss of signal for these

Optics for Research
Polarizer
Calibration step
8-9-91

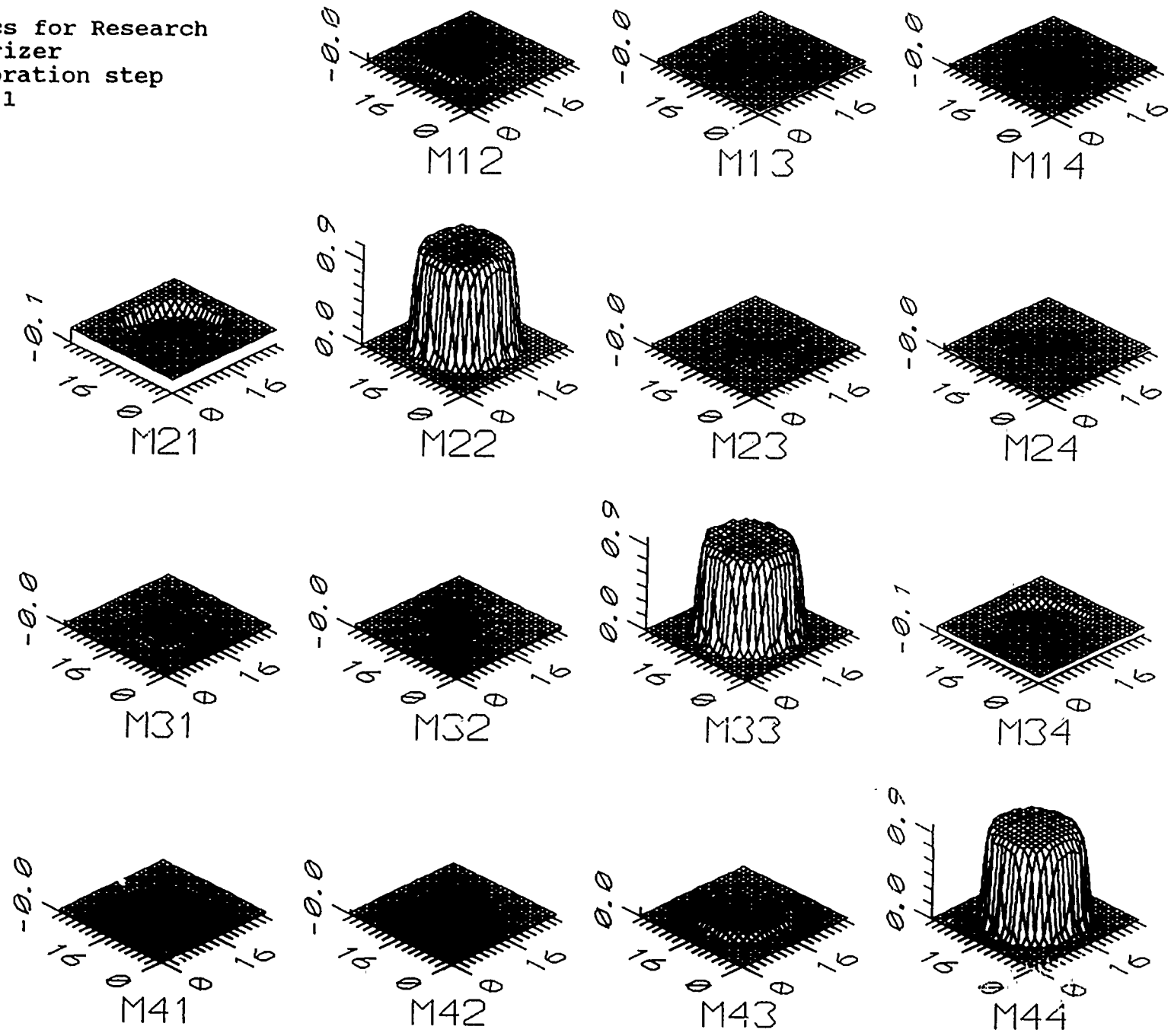

Figure 38

Optics for Research
Polarizer
8-9-91

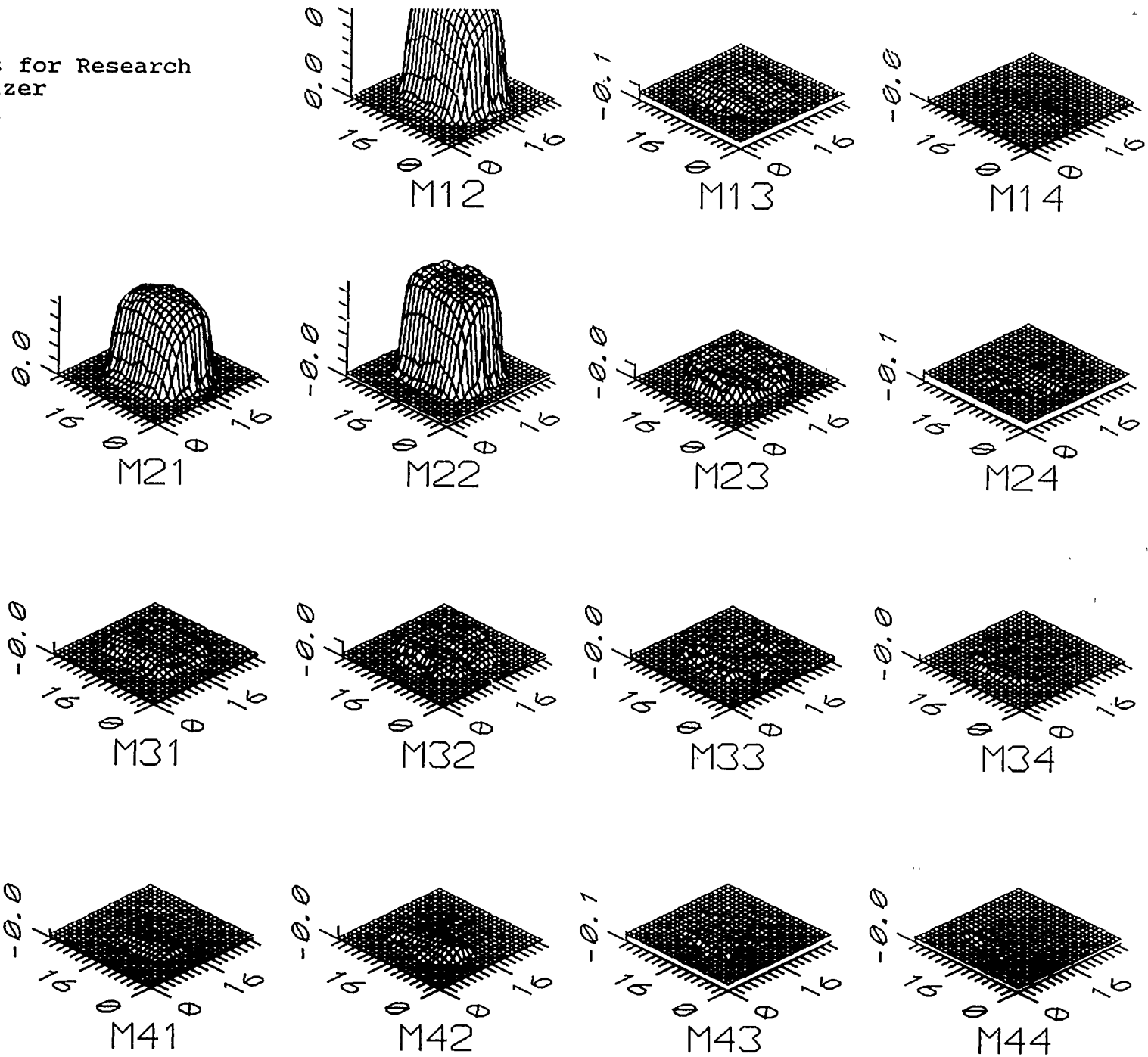

Figure 39

Meadowlark
Liquid Crystal
Circular Polarizer
8-7-91

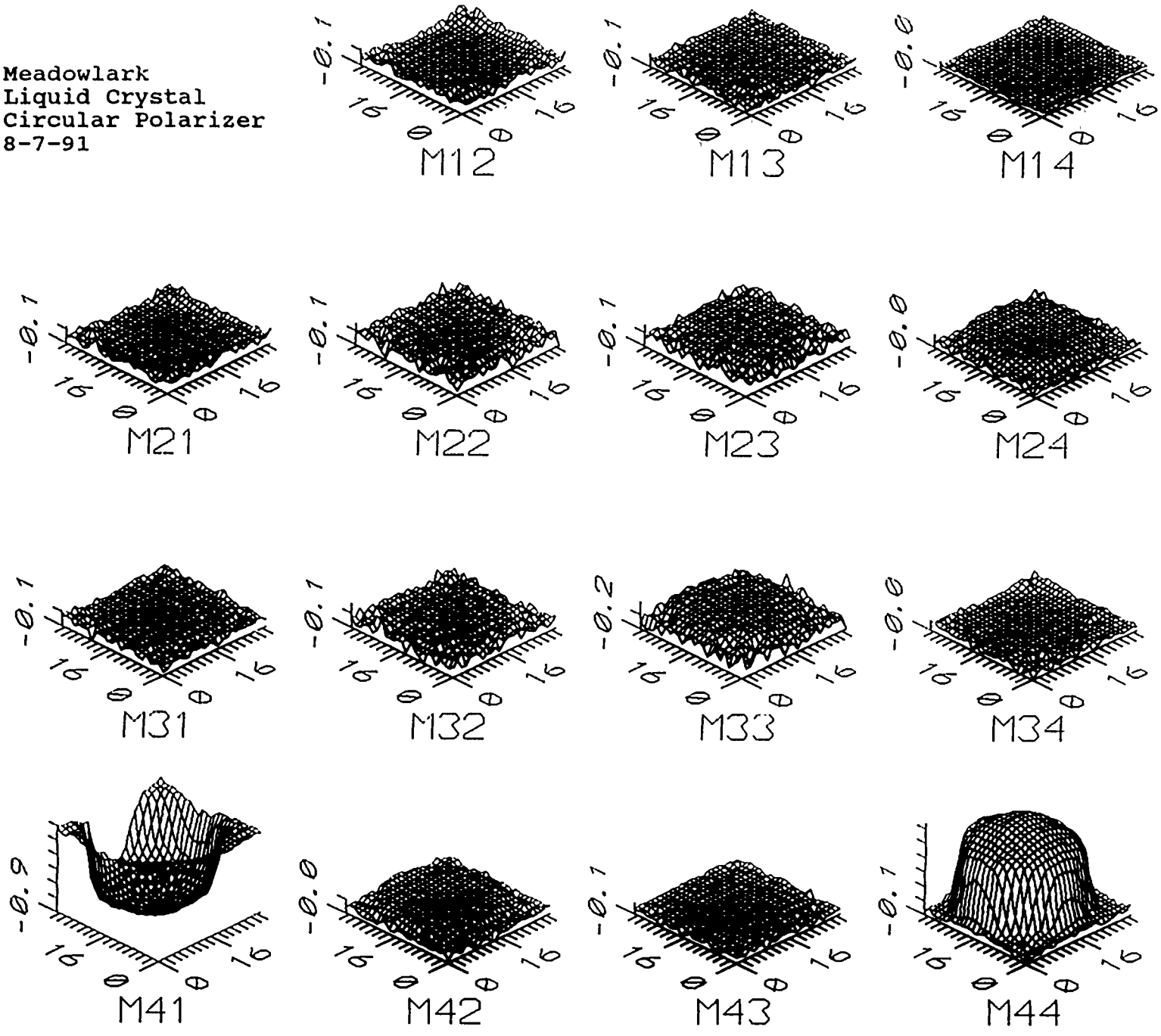

Figure 40

measurements introduces substantial amounts of noise into the measurement. The behavior of the circular polarizer, however is present in the lower right and lower left elements of the matrix. Further research is needed to modify the present measurement technique to allow the imaging polarimeter to characterize circular diattenuators.

A measurement of the uniformity of a zero order linear quarterwave retarder is shown in Figure 41. The Stokes imaging polarimeter was used to measure this sample at 633nm. A plane wave of uniform linear polarization was incident on the sample such that the linear polarization direction was aligned with the fast axis of the quarterwave retarder. The polarization states of the transmitted co-linear rays are plotted as a function of wavefront coordinate. The transmitted wavefront polarization is nearly uniform. The non-uniformity is primarily due to a spatial variation of the crystal axis orientation across the sample. Thickness variations also contribute to non-uniformity although the two effects can not be decoupled.

7. Calibration Issues

In this section, the issues of camera calibration, bootstrap calibration of the polarization generator and analyzer elements, movement in the scene, source/detection fluctuations, beam wander, and instrumental polarization are discussed.

7.1 Camera calibration

Camera calibration can be relaxed somewhat due to the nature of our measurement technique. Our calculated images, or pupil maps in the case of the PBSC measurements, consist of added and subtracted images divided by another image. Normally each pixel grey value would need to multiplied by a sensitivity factor which is slightly different for each pixel (sometimes 10% difference), but since our images ratioed, the sensitivity factor divides out. However, the dark count (pixel value at zero light level) must be subtracted out of each measurement. All data reduction algorithms do this.

7.2 Polarizing element calibration

Without sufficient prior knowledge of the properties of the polarization elements, a bootstrap calibration needs to performed, i.e. a calibration using retarders and polarizers with unknown properties. The calibration should make the fewest number of assumptions about the polarizing elements and utilize methods that are relatively insensitive to the

Polarization map

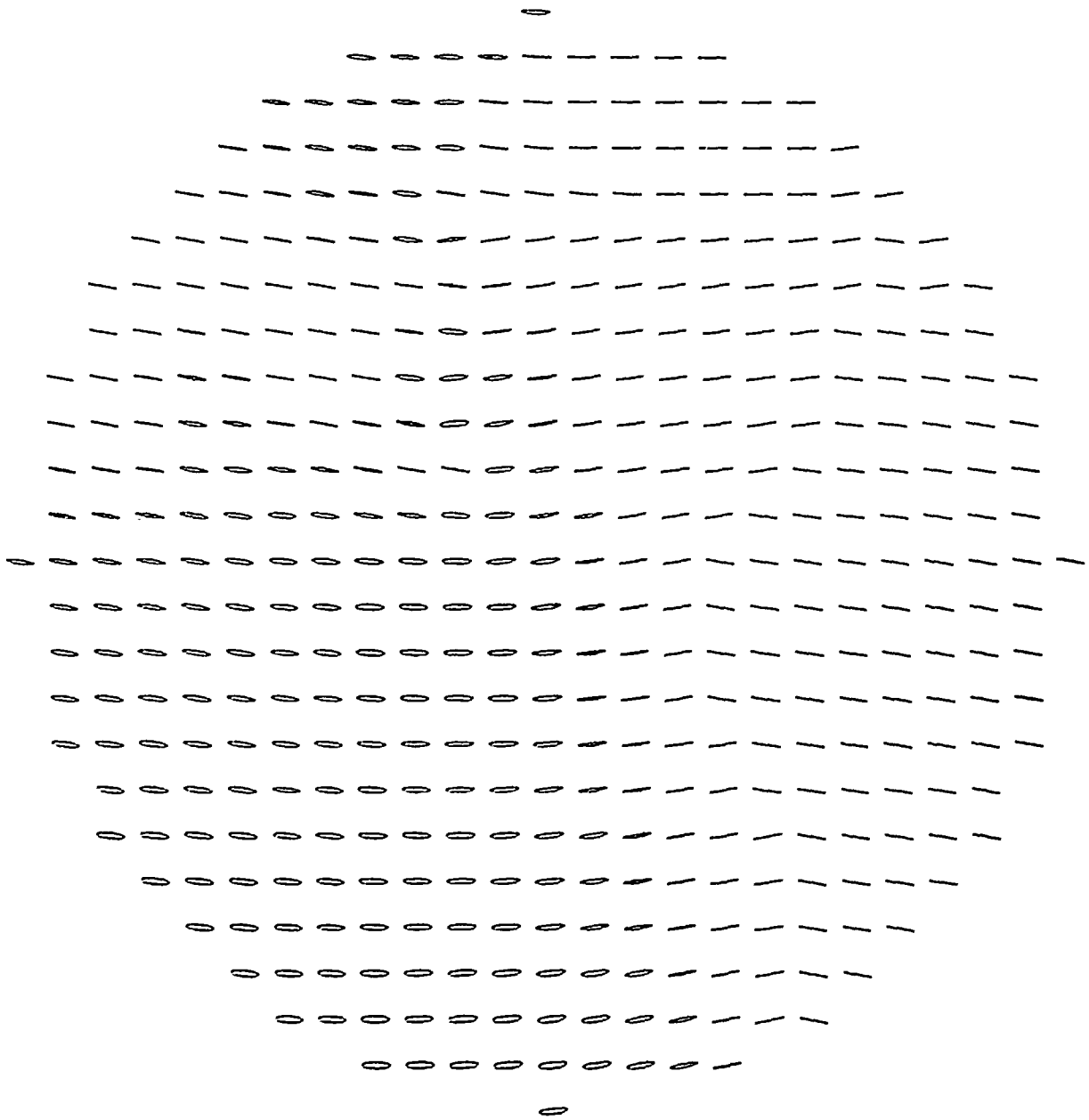

Polarization map of wavefront emitted from a quartz quarterwave retarder as a function of wavefront coordinate. Retarder illuminated with a plane wave of linear polarization parallel to the fast axis.

Figure 41

weakest assumptions. Once an accurate Mueller matrix polarimeter is operating, it can be used to calibrate polarization elements for other polarimeters, greatly simplifying the exacting task of construction and accurate imaging polarimeter.

Preliminary calibration has been done on the UAH imaging Stokes polarimeter. Polarizer calibration assumed that the polarizers only display diattenuation. The transmittance of the transmission axis and the absorption axis of polarizers were measured. Two similar polarizers were calibrated in this way were then used to calibrate the retarders. The first nine elements m_{11} through m_{33} of the retarder Mueller matrix were measured by rotating the polarizers at a 3:1 ratio on either side of the quarter wave retarder. The resulting intensity modulation has four harmonics and a dc term in its Fourier series which will solve for the nine Mueller matrix elements. The linear retardance and linear diattenuation can be obtained from these nine Mueller matrix components assuming there is no circular retardance. Circular retardance occurs in multiple element linear retarders when the fast axes of the linearly birefringent elements are not exactly 0° or 90° apart. To test for circular retardance, the QWLR was placed between two crossed linear polarizers with its fast parallel to the transmission axis of the first polarizer. If circular retardance is present, the electric field vector is rotated slightly, so that the final polarizer must be rotated to locate the null. No circular retardance was observed in these retarders, but we have detected it in other linear retarders. If circular retardance is observed, the remaining seven components of the QWLR Mueller matrix should be measured. A method to measure these components is described in reference 22.

7.3 Speed of data acquisition

The imaging polarimeters discussed here take measurements sequentially in time and are sensitive to drift. Any change in source intensity or any drift in camera sensitivity during the measurement sequence is a source of 1/f noise. The measurements must be made as quickly as mechanically possible. The rotation stage which rotates the polarization generating and analyzing elements is the limiting factor. Ideally the stage should rotate the polarizing element into position during one frame period or 1/30th second. This would be a dead frame period. In the case of the Stokes polarimeter, if frame averaging is not done, the measurement time required would be four frames for data acquisition and three dead frames, or 7/30th of a second. High speed data acquisition may enable polarimetric measurements of quasi-still life such as planes, boats or vegetation.

7.4 Beam wander

Another important calibration issue is beam wander. To understand the problem, consider how digital image processors calculate derivatives. A partial derivative of the image intensity in the x direction is calculated by shifting the image in the x direction and subtracting the image from itself. The imaging polarimeter performs data reduction by adding and subtracting images. A moving object in the scene introduces spurious contributions into the Stokes images proportional to the resulting intensity derivatives. These intensity gradients are often greatest around the objects edges, but edges are where many objects have their greatest polarization signatures. Fortunately, in optical system polarimetric metrology, our subject is usually a fixed optical system and the intensity gradients are generally small. Thus, far more accurate polarimetry is possible in this setting than in remote sensing or tactical polarimetry.

The faces of QWLR need to be highly parallel because wedge in a rotating element generates beam wander. If the retarder is slightly prismatic, the image will move in a circle on the ccd resulting in a spatial misregistration and image derivatives. Large amounts of beam wander can be partially compensated by carefully shifting the measured images in software.

7.5 Instrumental polarization

The instrumental polarization due to wavefront shaping optics within the polarimeter may require compensation during data reduction. Their instrumental polarization will have to be determined each time a new optical system is configured within the sample compartment, so standardized methods for removing this systematic error should be developed.

8. Conclusions

This research has produced analytical methods to aid in the polarization design of polarization based optical computers and has developed needed instrumentation to measure and understand the propagation of polarized light in polarization based optical interconnects.

We provide a summary of the polarization analysis done on the AT&T Iteration 3 Photonic Switching Network. The analytical approach can be used to analyze other polarization based optical computing architectures. In the course of the analysis and research, we discovered several methods which may improve the efficiency of the optical interconnects associated with AT&T optical computers. The changes to the existing designs involve replacing several quarter wave linear retarders with circular retarders, and inserting half wave retarder plates in two places to manipulate the instrumental polarization so that the instrumental polarization works in our favor.

An Imaging Polarimeter has been built and calibrated to perform polarization metrology on polarizing optical systems. It presently operates at 633nm and 849nm. The Imaging Polarimeter can be operated in two configurations. In the first configuration, it measures polarization content over a wave front. The polarization of an optical system can be measured at the exit pupil to obtain the polarization aberration, or it can measure the polarization content of an image to obtain the polarization point spread function. In the second capacity it sends in polarization states and measures output polarization states to measure the polarization properties of the optical system for a set of ray paths. From a set of measurements, the Mueller matrix of an optical system can be obtained as a function of field of view and pupil coordinate.

The Imaging polarimeter demonstrated its usefulness in a set of measurements made on polarizing beam splitter cubes. The paper which developed out of this work "Angular dependence of polarizing beam splitter cubes," has been submitted to Applied Optics and is attached to the end of the report. Several other measurements have been made with the Mueller matrix Imaging Polarimeter, such as quarter wave retarders, circular polarizers, and total internal reflection polarizers.

Further research is needed to increase the accuracy of the Imaging Polarimeter. Presently, accuracy of the Imaging Polarimeter is limited by the 8-bit A-D conversion of the video frame grabber board. An upgrade to a 12-bit A-D conversion could increase the

accuracy by as much as a factor of 10. The added accuracy is needed to study smaller polarization effects, such as weak instrumental polarization, or weak field of view dependence of a polarizing device, or even depolarization.

7. References

1. A. Huange, "Architectural considerations involved in the design of an optical digital computer," Proc. IEEE **72**, 780-786 (1984).

2. D.A.B. Miller, D.S. Chemla, T.C. Damen, A.C. Gossard, W. Wiegmann, T.H. Wood and C.A. Burrus, "Novel hybrid optically bistable switch: The quantum well self-elector-optic effect device," Appl. Phys. Lett. **45**, 13 (1984).

3. D.A.B. Miller, D.S. Chemla, T.C. Damen, T.H. Wood, C.A. Burrus, A.C. Gossard and W. Wiegmann, "The quantum well self-electro-optic-effect device ,optoelectronic bistability and oscillation, and self linearized modulation," IEEE J. Quantum Electron, **QE-21**,1462 (1985).

4. D.A.B. Miller, J.E. Henry, A.C. Gossard, and J.H. English, "Integrated quantum well self-electro-optic effect device: 2x2 array of optically bistable switches," Appl. Phys. Lett. **49**, 821 (1986).

5. G. Livescu, D.A.B. Miller, J.E. Henry, A.C. Gossard, and J.H. English, "Spatial light modulator and optical dynamic memory using integrated symmetric self-electro-optic effect devices," in *Postdeadline Papers, Conference on Lasers and Electro-optics* (Optical Society of America, Washington DC 1987), paper ThU11; Optics Lett., April 1988.

6. D.A.B. Miller, D.S. Chemla, T.C. Damen, A.C. Gossard, W. Wiegmann, T.H. Wood and C.A. Burrus, "Band-edge electroabsorption in quantum well structures: The quantum confined stark effect," Phys. Rev. Lett. **53**, 2173 (1984).

7. D.A.B. Miller, D.S. Chemla, T.C. Damen, A.C. Gossard, W. Wiegmann, T.H. Wood and C.A. Burrus, "Electric field dependence of optical absorption near the band gap of quantum well structures, "Phys. Rev. B **32**, 1043 (1985).

8. A.L. Lentine, H.S. Hinton, D.A.B. Miller, J.E. Henry, J.E. Cunningham, and L.M.F. Chirovsky, "Symmetric self-electro-optic effect device:Optical set-reset latch,"Appl. Phys. Lett., **52**, 1419 (1988).

9. F.B. McCormick, A.L. Lentine, L.M.F. Chirovsky, and L.A. D'Asaro, "An all-optical register using symmetric self electro-optic effect devices," in Conference on Photonic Switching (Optical Society of America, Salt Lake City, Utah, 1989), paper ThC5-1.

10. A.L. Lentine, H.S. Hinton, D.A.B. Miller, J.E. Henry, J.E. Cunningham, and L.M.F. Chirovskiy, "Symmetric self-elctro-optic effect device: Optical set-reset latch," Appl. Phys. Lett., **52**, 1419(1988).

11. M.E. Prise, N. Striebl, and M.M. Downs, "Optical considerations in the design of a digital optical computer," Optical and Quantum Electronics, **20**, 49-77, 1988.

12. M.E. Prise, M.M. Downs, F.B. McCormick, S.J. Walker, and N. Streibl, "Design of an optical digital computer," OSA Topical Meeting on Optical Bistability, OB-4 (March 1989).

13. M.E. Prise, N.C. Craft, R.E. LaMarche, M.M. Downs, S.J. Walker, L.A. D'Asaro, and L.M.F. Chirovsky, "Module for optical logic circuits using symmetric self-electrooptic effect devices," Appl. Optics **29**, 2164-2170 (1990).

14. A. Dickenson and Michael E. Prise, "Free-space optical interconnection scheme," Appl. Optics 29, 20012005 (1990).

15. M. Banning, "Practical methods of making and using multilayer filters," J. Opt. Soc. Am. **37**, 792-797 (1947).

16. J. Mouchart, J. Begel and E. Duda, "Modified MacNeille cube polarizer for a wide angular field," Appl. Optics 28, 2847-2853 (1989).

17. R.A. Chipman, "Polarization analysis of optical systems," Opt. Eng. **28**, 90-999 (1989).

18. R.A. Chipman, "Polarization analysis of optical systems II," Proc. SPIE **1166**, 79-94 (1989).

19. J.P. McGuire, Jr. amd R.A. Chipman, "Polarization aberrations in optical systems," Current Developments in Optical Engineering II, R. Fischer, W.Smith, Editors, Proc. SPIE **81**, 240 (1987).

20. R.A. Chipman and L.J. Chipman, "Polarization aberration diagrams," Opt. Eng. **28**, 100-106 (1989).

21. J.L. Pezzaniti and Russell A. Chipman, "Imaging Polarimeters for optical system metrology," Proc. SPIE **1317**, 280-294 (1990).

22. M.F. Morgan and R.A. Chipman, "An ultraviolet polarimeter for characterization of an imaging spectrometer," Proc. SPIE **1317**,384-394 (1990).

Appendix A

Draft of a paper published in SPIE proceedings 1317

Imaging polarimeters for optical metrology

J. Larry Pezzaniti

Russell A. Chipman

Dept. of Physics
University of Alabama in Huntsville
Huntsville, AL 35899

Imaging Polarimeters for Optical Metrology

Joseph L. Pezzaniti, Russell A. Chipman

University of Alabama in Huntsville, Department of Physics
Huntsville, AL 35899

Abstract

In this paper we describe two configurations of imaging polarimeters designed for polarimetric optical metrology. The first is a Stokes imaging polarimeter which measures the polarization response of optical systems to spherical or planar waves of known polarization. The output is images of the degree of polarization, orientation and eccentricity of polarization ellipses, or Stokes parameters displayed as a function of either the exit pupil or image coordinate of the optical system. The second configuration is a Mueller imaging polarimeter which measures the Mueller matrix of an optical system on a ray by ray basis. Calibration issues involved in building these instruments are addressed along with a brief discussion on polarization aberration mechanisms.

1. Introduction

For the majority of optical systems, detailed information about their effects on the polarization of light is not important. Systems can often be accurately analyzed by ray tracing using the assumption that polarization and intensity across the wavefront remains unaffected by the optical system. When this assumption is no longer valid, the ray tracing algorithm must be generalized to include the polarization effects of the optical system. Polarization ray tracing calculates the variation in the intensity and polarization associated with different ray paths through an optical system.[1-4] Similarly, an imaging polarimeter can be used as an optical metrology tool to measure the polarization properties of optical systems and align these systems. An immediate application is to develop a data base on the relative properties of polarization components as a function of wavelength and field of view.

There are many optical systems where instrumental polarization is a concern, such as

interferometers, polarimeters, optical computers, grazing incidence optics, and phased arrays. In interferometric systems, such as laser radars and analog optical computers, light coupled into the orthogonal state due to instrumental polarization will not interfere with the reference beam, decreasing the interferometer's fringe visibility and information processing capability. Polarization state should be strictly maintained in polarimeters and ellipsometers, since any spurious polarization contributions from the instruments polarization leads to inaccurate results. Other examples of systems in which polarization is a concern include broad spectral band systems, precision radiometers, phased arrays, and optical signal processors.

The University of Alabama in Huntsville (UAH) imaging polarimeter is specifically designed to analyze a digital optical computer under development at AT&T Bell Laboratories.[5-7] This system uses polarization beam combining to interlace two arrays of beams onto a modulator and bring them out together in a third direction. Each logic module uses ten polarizing beam splitters and twelve quarter wave linear retarders and involves fourteen changes of polarization state. Small polarization effects in one polarizing beam splitter can become serious problems in a series of ten polarizing beam splitters. Furthermore, systems considerations drive the designer to use as large a field of view as possible through the system. If the polarization state is not correct, then at each polarizing beam splitter, part of the beam takes the wrong path and eventually is imaged onto the wrong modulator. The imaging polarimeter is needed for the study and alignment of this system.

This paper describes two closely related types of imaging polarimeters for metrology of optical systems, a Stokes imaging polarimeter and a Mueller imaging polarimeter. A Stokes imaging polarimeter measures the polarization response of an optical system to a given input polarization state by determining the Stokes parameters across a wavefront. A Mueller imaging polarimeter measures the Mueller matrix of an optical system on a ray by ray basis. From the Mueller matrix, the linear and circular diattenuation and linear and circular retardance associated with each ray path may be calculated.

2. Stokes imaging polarimeter

The imaging polarimeter at UAH is being developed for optical system metrology. Other Stokes imaging polarimeters have been described for application to solar vector magnetograph measurements [8], earth resource investigations [9], and remote sensing.[10]

Figure 1 shows a schematic of our Stokes imaging polarimeter. It consists of a rotating retarder polarimeter followed by a CCD camera connected to an image processor. The

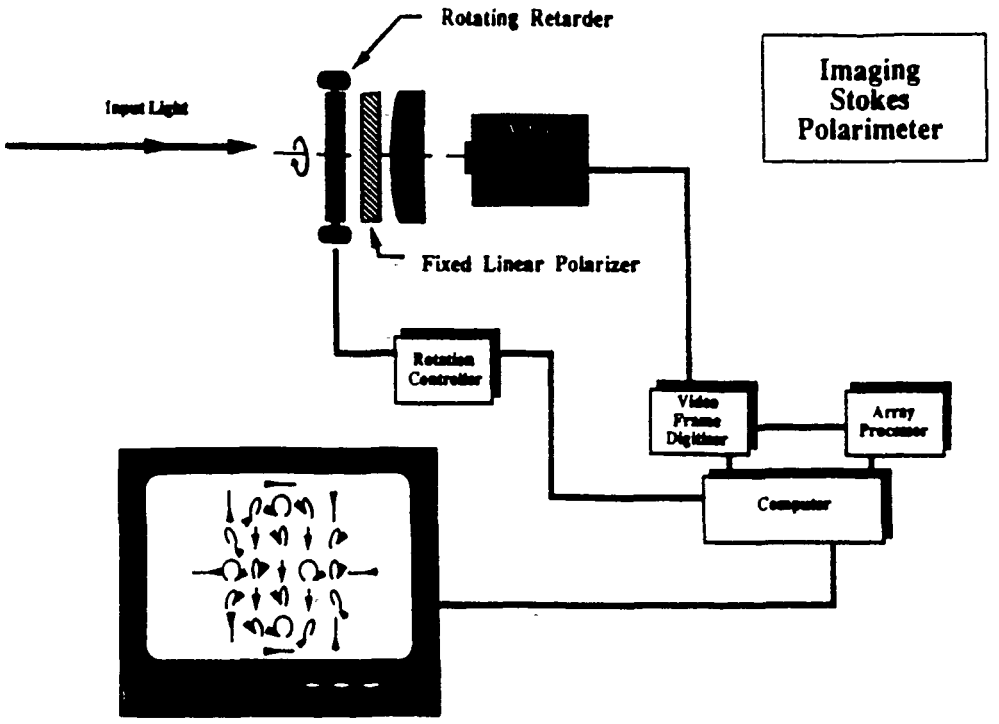

Figure 1. Schematic diagram of a rotating retarder Stokes imaging polarimeter.

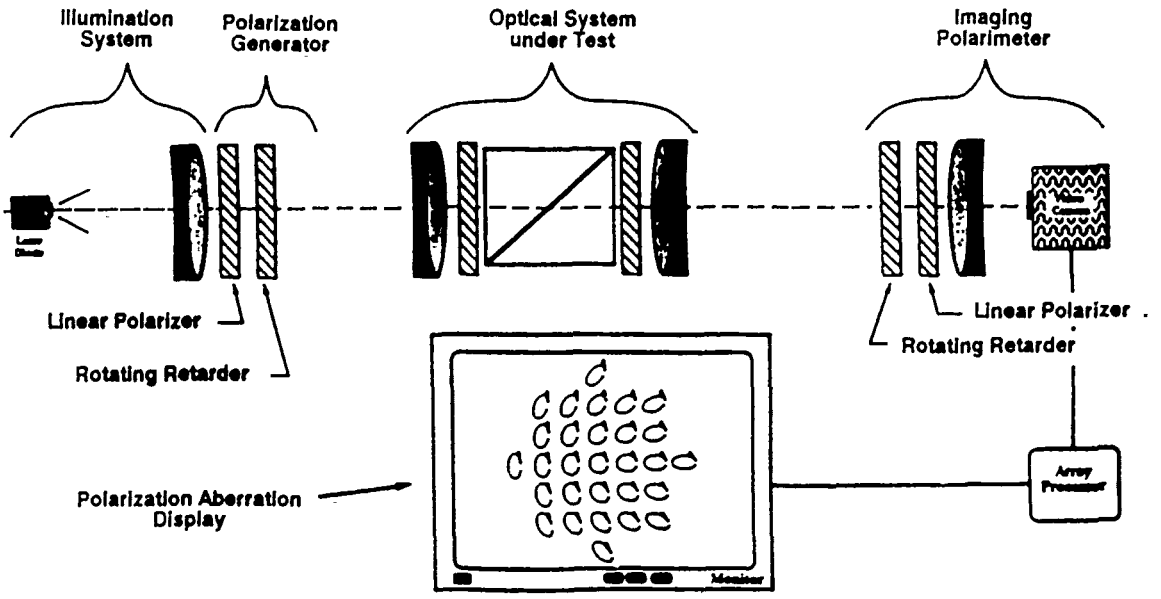

Figure 2. Schematic diagram of a Mueller matrix imaging polarimeter.

polarimeter consists of a quarter wave linear retarder (QWLR) followed by a linear polarizer (LP). The CCD camera has a 576x485 resolution. The DT2861 image processor board holds 16 images in memory simultaneously and is able to do frame addition/subtraction, multiplication/division, zoom, pan and scroll, AND, OR ,XOR logic operations, and display output in false color.

The objective of the Stokes imaging polarimeter is to determine a Stokes vector associated with each pixel of the camera. The imaging polarimeter needs to acquire a minimum of four images at different orientations of the QWLR to calculate the Stokes parameters. The result, following data reduction, is a set of Stokes images where a Stokes image is defined as an image displaying one of the Stokes parameters. The four resulting Stokes images describe the intensity, linear polarization, orientation, and circular polarization content of the light in the scene.

Our interest is principally in polarimetric metrology of optical systems. We operate the Stokes imaging polarimeter by introducing a plane wave or spherical wave of known polarization state into the optical element or optical system under test, and measuring Stokes images of the transmitted light. These Stokes images can be measured at either the exit pupil or image plane by focusing the camera on that plane. If the camera is focused on the exit pupil, then each pixel of the camera corresponds to a ray path through the optical system under test and the imaging polarimeter measures the polarization aberration function.[2] If the camera is focused on the image plane, then the distribution of polarization states in the point spread function is measured and the polarization point spread function of the system is determined in Stokes vector form. Since the point spread function is usually only a few microns in diameter, a microscope objective or other high magnification system is needed to observe the structure of the point spread function with the CCD camera.

We refer to pixel coordinates as coordinates which locate a particular pixel on the CCD. These pixel coordinates may correspond to either pupil coordinates or image coordinates of the optical system under test, depending on which plane the imaging polarimeter is focussed.

The polarimeter section of the instrument consists of a QWLR which rotates followed by a LP which is fixed. The polarization state transmitted through the polarimeter $\vec{S}'(x',y')$, written as a function of pixel coordinates (x',y'), is related to the polarization state incident on the polarimeter $\vec{S}(x,y)$, written as a function of exit pupil or image plane coordinates (x,y) of the optical system under test, by the polarimeter equation

$$\vec{S}'(x',y') = M_{LP}(\phi = 0) M_{QWLR}(\theta) \vec{S}(x,y). \qquad (1).$$

$M_{LP}(\phi)$ is the Mueller matrix of the LP, and $M_{QWLR}(\theta)$ is the Mueller matrix of the QWLR oriented at angle θ. The LP remains at a fixed orientation $\phi = 0$ for all measurements. If the linear polarizer changed orientation, the instrumental polarization of the camera lens and/or CCD might need to be compensated as a possible systematic error. This would occur if the transmission through the lens (or a folding mirror) or the sensitivity of the CCD was a function of incident polarization state. But the polarization state transmitted to the camera lens and CCD is always in a fixed state of linear polarization insuring that the effect of the instrumental polarization of the camera lens and CCD are the same for all measurements.

For the LP at an angle $\phi = 0°$ and assuming ideal polarization elements, Eq. 1 becomes:

$$\begin{pmatrix} s_0' \\ s_1' \\ s_2' \\ s_3' \end{pmatrix} = \frac{1}{2} \begin{pmatrix} 1 & 1 & 0 & 0 \\ 1 & 1 & 0 & 0 \\ 0 & 0 & 0 & 0 \\ 0 & 0 & 0 & 0 \end{pmatrix} \begin{pmatrix} 1 & 0 & 0 & 0 \\ 0 & \cos^2 2\theta & \cos 2\theta \sin 2\theta & -\sin 2\theta \\ 0 & \sin 2\theta \cos 2\theta & \sin^2 2\theta & \cos 2\theta \\ 0 & \sin 2\theta & -\cos 2\theta & 0 \end{pmatrix} \begin{pmatrix} s_0 \\ s_1 \\ s_2 \\ s_3 \end{pmatrix}. \qquad (2)$$

The CCD measures the intensity s_0' but not the polarization state $\vec{S}'$ of the light. s_0' is a function of the QWLR orientation θ,

$$s_0'(x',y',\theta) = \frac{1}{4}(2s_0(x,y) + s_1(x,y)(1 + \cos 4\theta) + s_2(x,y)\sin 4\theta - 2s_3(x,y)\sin 2\theta \qquad (3)$$

Video frames of $s_0'(x',y',\theta)$ are digitized at four different orientations θ of the QWLR. By orienting the QWLR at orientations that produce four linearly independent equations in $s_0(x,y), s_1(x,y), s_2(x,y), s_3(x,y)$, the four Stokes images are calculated from the four measured images $s_0'(x,y,\theta_1), s_0'(x,y,\theta_2), s_0'(x,y,\theta_3), s_0'(x,y,\theta_4)$.

The QWLR is necessary to obtain the third Stokes parameter s_3 because a polarimeter consisting of only a LP can measure only s_0, s_1, s_2.

One data acquisition routine which provides a particularly simple set of inversion equations orients the QWLR at angles $\theta = 45°, -45°, 67.5°, 90°$. The four Stokes images are obtained from the equations

$$s_0(x,y) = s_0'(x',y',45°) + s_0'(x',y',-45°), \tag{4}$$

$$s_1(x,y) = 2s_0'(x',y',90°) - s_0'(x',y',45°) - s_0'(x',y',-45°), \tag{5}$$

$$s_2(x,y) = (1+\sqrt{2})s_0'(x',y',45°) + (1-\sqrt{2})s_0'(x',y',-45°) + 2s_0'(x',y',90°) - 4s_0'(x',y',67.5°), \tag{6}$$

$$s_3(x,y) = s_0'(x',y',-45°) - s_0'(x',y',45°). \tag{7}$$

While images acquired at QWLR angles of $\theta = 45°, -45°, 67.5°, 90°$, simplify the data reduction, they do not measure all four Stokes parameters with equal accuracy. The first two measurements at $\theta = 45°$ and $\theta = -45°$ involve only s_0 and s_3, while the measurement at $\theta = 67.5°$ involves s_0, s_1, s_2 and s_3, and $\theta = 90°$ involves only s_0 and s_1. Therefore s_0 and s_3 are determined from two measurements, s_1 is determined from three measurements, and s_2 is determined from four.

Two different methods have been developed to calculate the Stokes images. In the first method the $s_0'(\theta,x,y)$ frames are added and subtracted in the Data Translation DT2861 frame grabber board, according to Eqs. 4-7. The accuracy of this method is restricted by the DT2861 frame grabber board since it performs integer arithmetic with 8 bits. If an addition, multiplication or subtraction results in a pixel level above 255 or below 0, the value will become 0 or 255. For this reason levels in the $s_0'(\theta,x,y)$ image contrast must be compressed by a factor of at least four with a corresponding loss of accuracy.

The second method performs the Stokes vector calculations as floating point calculations in computer memory. This does not require contrast compression but takes longer to calculate. The arrays containing the Stokes images are then shipped back over the computer bus to the frame buffers of the DT2861 board, where the images are displayed. Presently, the four Stokes vector images are calculated in about 15 sec. by method 1 and about 3 min. by method 2.

The Stokes images contain intensity as well as polarization information, all as a function of image coordinate. The zeroth Stokes image $s_0(x,y)$ is the intensity image and is

always positive. The first, second and third Stokes images can be positive or negative, so the images are displayed with zero as 128. Positive values of s_1, s_2, s_3 are displayed from 129 to 255, and negative values from 0 to 127, requiring a contrast compression of two.

A number of other useful measures of polarization can be displayed as images. The degree of polarization DOP is a measure of the overall polarization of the light. It is defined as

$$\mathrm{DOP} = \frac{\sqrt{s_1^2 + s_2^2 + s_3^2}}{s_0}. \tag{8}$$

DOP varies from zero for unpolarized light to one for polarized light.

The degree of linear polarization DOLP is a measure of the amount of linear polarization

$$\mathrm{DOLP} = \frac{\sqrt{s_1^2 + s_2^2}}{s_0}. \tag{9}$$

DOLP is zero for unpolarized or circularly polarized light and is one for linearly polarized light.

The degree of circular polarization DOCP is a measure of the amount of circular polarization

$$\mathrm{DOCP} = \frac{|s_3|}{s_0}. \tag{10}$$

DOCP is zero for unpolarized and linearly polarized light and one for right or left circularly polarized light.

Two other definitions are necessary to specify a polarization ellipse. The eccentricity χ of the polarization ellipse is

$$\chi = \frac{1}{2}\arcsin\left(\frac{s_3^2}{s_1^2 + s_2^2 + s_3^2}\right), \tag{11}$$

and the orientation α of the major axis of the polarization ellipse is

$$\alpha = \frac{1}{2} arctan\left(\frac{s_2}{s_1}\right). \qquad (12)$$

One useful display of polarization aberration is graphical maps containing arrays of polarization ellipses representing the average polarization of regions of the wavefront, such as is shown in Figure 3.

Similarly images of $DOP(x, y)$, $DOLP(x, y)$ and $DOCP(x, y)$ can be displayed with 256 grey levels or in false color.

3. Mueller matrix imaging polarimeter

Mueller matrix polarimeters have been built to measure the Mueller matrix of polarizing elements as a function of wavelength,[11] to measure Mueller matrices at laser wavelengths,[12] and to measure the Mueller matrices of scattered light.[13,14] The UAH Mueller matrix imaging polarimeter will measure the Mueller matrix as a function of exit pupil coordinate or image coordinate of an optical system.

The Mueller matrices describing optical systems are in general functions of object and pupil coordinate. Each ray path through an optical system will have slightly different polarizing properties because of different angles of incidence and orientations of its plane of incidence at thin films and different directions and path lengths through birefringent or dichroic materials. The polarization aberration function $M(\vec{h}, \vec{\rho}, \lambda)$ for an optical system is a Mueller matrix as a function of object coordinate $\vec{h}$, pupil coordinate $\vec{\rho}$, and wavelength λ.[1,2] The spatial dependence of the Mueller matrix gives rise to polarization aberrations at the exit pupil of the optical system.[1-4] The Mueller matrix imaging polarimeter measures the spatial dependence of the Mueller matrix for a set of ray paths through an optical system under test.

The UAH imaging polarimeter uses a collimated quasimonochromatic light source and two QWLR - LP pairs in conjunction with a CCD camera (see figure 2). Each pixel of the CCD camera measures the Mueller matrix for a particular ray path through the optical system. The light from the source is collimated and passes through a LP at a fixed orientation angle, then a QWLR mounted to a rotary stage. The light source and the LP/QWLR pair comprise the polarization generator. Lenses then prepare the appropriate input spherical wave for the optical system under test, where the polarization of each ray will be altered according to the Mueller matrix for that particular ray path. The light is recollimated and enters the Stokes imaging polarimeter. The camera is focused either on

the exit pupil of the optical system or its image plane. By fixing the orientation of the two linear polarizers, the imaging polarimeter becomes insulated from instrumental polarization before the first polarizer and after the final polarizer.

Any optics between the polarizers used to reshape the wavefront may introduce additional instrumental polarization. This potential systematic error must be compensated for in the calibration and data reduction if the polarization contribution from these elements are substantial.

Our Mueller matrix imaging polarimeter will use a variation of the method proposed by Azzam [15] and expanded by others [16,17] to calculate the Mueller matrices from the raw polarimetric data. In Azzam's method, the orientation of the two linear polarizers are fixed and a series of at least 24 images are recorded with different retarder settings. The first image is acquired with the transmission axes of the polarizers and the fast axes of the retarders all parallel. Between image measurements, the first retarder is rotated by $\Delta\theta$ and the second retarder by $5\Delta\theta$ until the first retarder has rotated through $180°$. For example, if the generating retarder is rotated in increments of 5 degrees, the analyzing retarder is rotated in 25 degree increments. This generates an intensity modulation at each pixel in the images. The polarization information is encoded on the first twelve harmonics and the dc component, so a minimum of twenty four images are needed over 180 degrees to sample the twelfth harmonic. The Fourier coefficients are calculated with the discrete Fourier transform at each pixel. The Fourier coefficients are manipulated to obtain the sixteen elements of the Mueller matrix associated with each pixel.

The Mueller matrix can be displayed as images of the individual matrix elements, or in other related polarization output. Our principal interest is to display the linear retardance and linear diattenuation in image form.

4. Calibration issues of an imaging polarimeter

Imaging polarimeters which take accurate data are very difficult to build. It is easy to buy the components and assemble an instrument. It is a long arduous project to align and calibrate the polarimeter, write software to acquire and reduce the data, and address meaningful optical metrology problems. In this section, the issues of bootstrap calibration, drift, moving objects, element wedge, angle of incidence dependence in the polarization elements, and instrumental polarization, are discussed.

If the Mueller matrices for the polarizers and retarders used in the polarimeter differ from their ideal values in Eq. 2, then the data reduction routines (Eq. 4-7) should be modified to take their actual behavior into account. Commercially available polarizers and

retarders are not specified well enough by the vendors to accurately estimate their Mueller matrices, nor are instruments or test services readily available to measure these Mueller matrices. Retarders are never exactly a quarter wave. Polarizers always have some leakage. Retarder and polarizer characteristics vary with wavelength and angle of incidence. Retarders display some diattenuation. Polarizers display some retardance. Linear polarizers or linear retarders may actually be elliptical.

Without sufficient prior knowledge of the properties of the polarization elements, a bootstrap calibration needs to performed, i. e. a calibration started using retarders and polarizers with unknown properties. The calibration should make the fewest number of assumptions about the polarizing elements and utilize methods that are relatively insensitive to the weakest assumptions. Once an accurate Mueller matrix polarimeter is operating, it can be used to calibrate polarization elements for other polarimeters, greatly simplifying the exacting task of construction an accurate imaging polarimeter.

Preliminary calibration has been done on the UAH imaging Stokes polarimeter. Polarizer calibration assumed that the polarizers only display diattenuation. The transmittance of the transmission axis and the absorption axis of polarizers were measured. Two similar polarizers were calibrated in this way were then used to calibrate the retarders. The first nine elements m_{11} through m_{33} of the retarder Mueller matrix were measured by rotating the polarizers at a 3:1 ratio on either side of the QWLR. The resulting intensity modulation has four harmonics and a dc term in its Fourier series which will solve for the nine Mueller matrix elements. The linear retardance and linear diattenuation can be obtained from these nine Mueller matrix components assuming there is no circular retardance. Circular retardance does occur in multiple element linear retarders when the fast axes of the linearly birefringent elements are not exactly $0°$ or $90°$ apart. To test for circular retardance, the QWLR was placed between two crossed linear polarizers with its fast parallel to the transmission axis of the first polarizer. If circular retardance is present, the electric field vector is rotated slightly, so that the final polarizer must be rotated to locate the null. No circular retardance was observed in these retarders, but we have detected it in other linear retarders. If circular retardance is observed, the remaining seven components of the QWLR Mueller matrix should be measured. A method to measure these components is described in reference 18.

The next issue is drift. The imaging polarimeters discussed here take measurements sequentially in time. Any change in source intensity or any drift in camera sensitivity during the measurement sequence is interpreted as polarization, albeit spurious polarization.

Similar problems arise in polarization measurements of a moving object. Consider how

digital image processors calculate derivatives. A partial derivative of the image intensity in the x direction is calculated by shifting the image in the x direction and subtracted the image from itself. The imaging polarimeter performs data reduction by adding and subtracting images. A moving object in the scene introduces spurious contributions into the Stokes images proportional to the resulting intensity derivatives. These intensity gradients are often greatest around the objects edges, but edges are where many objects have their greatest polarization signatures. Fortunately, in optical system polarimetric metrology, our subject is usually a fixed optical system and the intensity gradients are generally small. Thus, far more accurate polarimetry is possible in this setting than in remote sensing or tactical polarimetry.

The faces of the QWLR need to be highly parallel because wedge in a rotating element generates beam wander. If the retarder is slightly prismatic, the image will move in a circle on the CCD resulting in a spatial misregistration and image derivatives. Large amounts of beam wander can be partially compensated by carefully shifting the measured images in software, but this correction cannot be performed at the fractional pixel level.

If light propagates at substantial angles through the polarization generator and the polarization analyzer, the field angle dependence of the polarizers and the retarders has to be treated as systematic error. For exit pupil measurements, each pixel on the CCD will corresponds to a different angle through the polarization components. A straightforward compensation can be performed which used the Mueller matrices as a function of propagation direction in the data reduction.

The instrumental polarization due to wavefront shaping optics within the polarimeter may require compensation during data reduction. Their instrumental polarization will have to be determined each time a new optical system is configured within the sample compartment, so standardized methods for removing this systematic error should be developed.

5. Typical polarization aberration mechanisms

The objective of the UAH imaging polarimeter is to study polarization aberration in optical components and optical systems. Polarization aberration contributions from optical elements can be conveniently grouped into two categories: instrumental polarization and nonideal polarization. The first category, "instrumental polarization" is due to optical elements which are not intended to control polarization such as lenses, mirrors and prisms. These elements usually have weak polarization. The other category, "nonideal polarization," is the deviation in performance of elements used to control polarization

from their ideal characteristics. Several examples of polarization aberration problems are mentioned here, microscope objectives, mirrors, coating thickness variations, field dependence in retarders, and polarizing beam splitters.

The classic example of polarization aberration is the instrumental polarization of microscope objectives in polarization microscopy.[19,20] The Fresnel transmission coefficients cause a lens to act with a radially oriented linear diattenuation which increases quadratically from the center of the pupil. This causes a rotation of the plane of polarization in four corners of the pupil when linearly polarized light is incident. The objective lens of a microscope contributes a substantial leakage in a "Maltese cross" pattern when located between crossed polarizers.

Metal mirrors introduce linear retardance due to the difference between s and p phase shifts upon reflection along with a lesser amount of linear diattenuation. Figure 3 shows a polarization ray trace calculation of a f/0.5 parabolic mirror coated with aluminum illuminated with circularly polarized incident light. At the center of the mirror, where the rays are normally incident, there is no difference in phase shift between s and p light. The handedness of the circular polarization changes upon reflection. At the edge of the mirror the linear retardance approaches a quarter wave with the effect of coupling circular polarized light to nearly linearly polarized light oriented at 45° to the p plane. Another example of instrumental polarization from mirrors is the very large polarization effects with grazing incidence telescopes such as the Advanced X-ray Astrophysical Facility (AXAF) telescope under development by NASA.[21]

Polarization aberration results from variations in multi-layer thin film coatings thicknesses. For instance, with coatings of ten to thirty layers, the retardance can vary tens of degrees over an f/2 parabolic mirror due to coating thickness variations and angle of incidence variations.[22]

The second category of polarization aberration is nonideal polarization from elements designed to control polarization including polarizers, retarders and polarizing beam splitters.

Several characteristics of birefringent retarders introduce polarization aberration in optical systems. First, the thickness of the birefringent material may be wrong or even wedged, yielding an incorrect or spatially varying retardance. The crystal axis can be misoriented relative to the faces or the mount. The retarder can be misaligned in the optical system, either tilted or with its fast axis at the wrong orientation.

Three other problems with retarders are more fundamental, field dependence, diattenuation, and birefraction.

Figure 4 shows how the extraordinary refractive index and the retardance varies with the

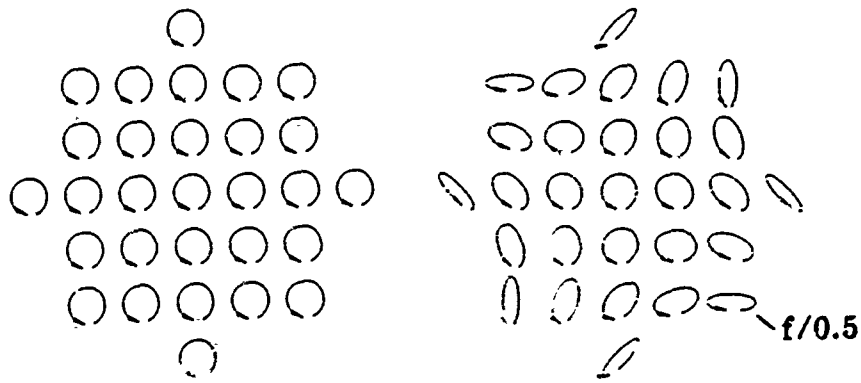

Figure 3. The effect of a f/0.5 telescope mirror on circularly polarized light. Elliptical polarization around the edge is due to tangentially oriented linear retardance of the interface.

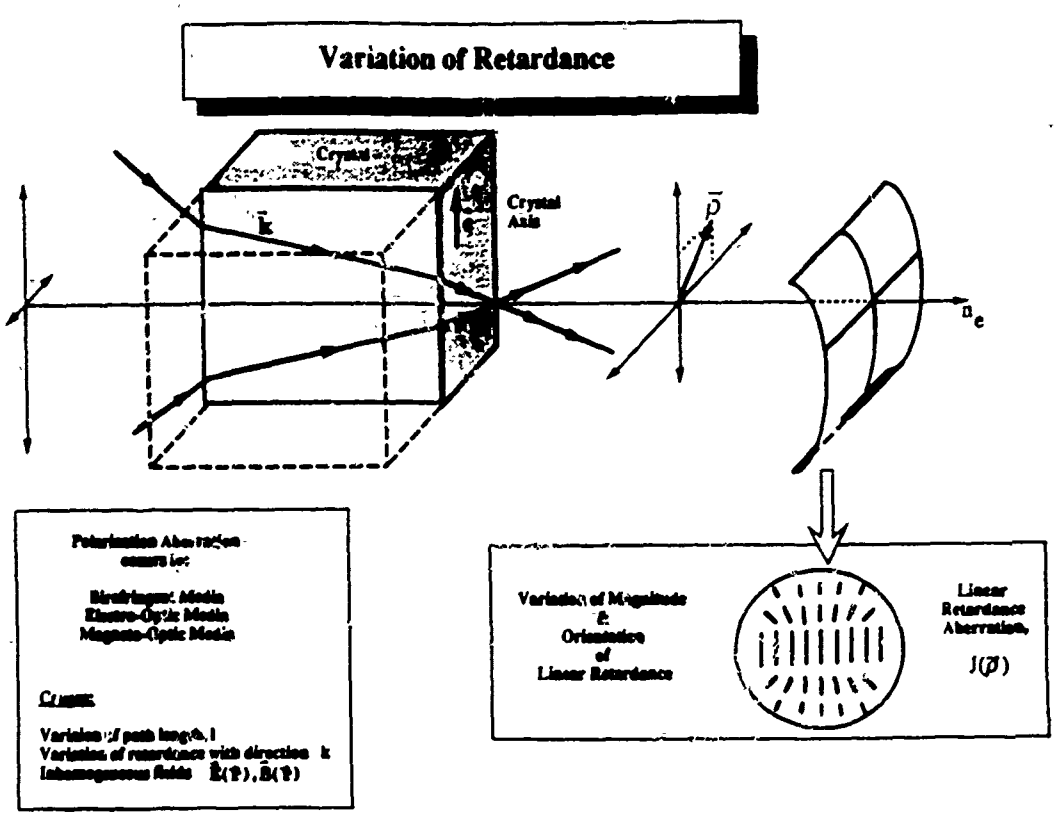

Figure 4. This figure shows the dependence of the extraordinary refractive index on ray angle. The extraordinary ray will have a quadratic variation in retardance with field angle and the ordinary ray will have a no variation in retardance with field angle.

direction of the incident light. Different parts of a spherical wave propagating through a birefringent retarder experience different retardances yielding polarization aberration.

Retarders have some weak diattenuation, both in their bulk absorption spectrum and from the difference in Fresnel losses between the ordinary and extraordinary rays at the interfaces. Anti-reflection coatings, carefully selected, can greatly reduce the diattenuation from birefringent interfaces.

Figure 5 shows the birefraction or double refraction in birefringent retarders and uniaxial media. The crystal axis is represented by $\vec{c}$. If the propagation vector in the crystal is not parallel or perpendicular to the crystal axis of the uniaxial media, the ordinary and extraordinary rays take divergent paths. This causes two crescents on the edges of the beam to have different polarization states from the main beam. Fig. 5 shows two cases of illumination of a quarter wave retarder at different angles of incidence with beams linearly polarized at $45°$ with respect to the fast axis. In the first case, the beam is normally incident and the entire transmitted beam is circularly polarized. In the bottom example, the beam is not normally incident. Since the refractive indices for the extraordinary and ordinary rays, represented by the lines and dots respectively, are different, the two rays are refracted at different angles. The transmitted beam has the desired polarization where the two beams overlap. The crescent-shaped areas along either edge of the light bundle contain light polarized in the eigen-polarization states of the medium.

Polarizing beam splitters are notorious for causing systems problems due to nonideal polarization. A ideal polarizing beam splitter reflects all the s polarized light and transmits all the p polarized light. In many applications, such as digital optical computers, a field of view of many degrees is required, so the reflection and transmission coefficients should be nearly constant over this range of field angles. Since the light is at non-normal incidence at the beam splitting interface, the reflection and transmission coefficients can vary linearly in the angle of incidence. This makes polarizing beam splitters intrinsically more angle of incidence sensitive than mirror or lens coatings which can show variation to only second order about normal incidence. We have yet to see a good polarizing beam splitter and are interested if there are fundamental limitations on the field of view performance of polarizing beam splitters.

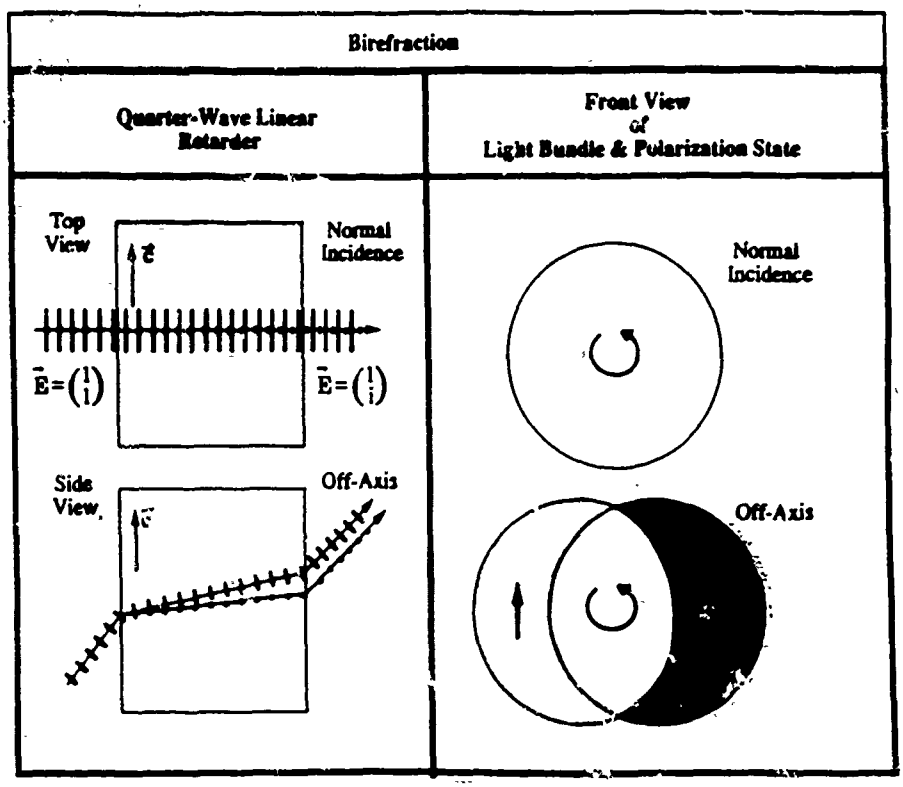

Figure 5. This figure shows how beam shear between extraordinary and ordinary rays limits the field of view of a quarter wave retarder.

6. Conclusion

The imaging polarimeter is a tool to measure the instrumental polarization of optical systems and calibrate polarization elements. It measures polarization properties associated with ray paths through optical systems. It can also determine the polarization state structure of an image. It provides, via CCD camera and image processing system, graphical maps of polarization information. It can be used to assist in the alignment of polarization critical optical systems. Finally it is needed for comparative data on the performance of polarizing elements, where it can simultaneously display performance as a function of field of view in an image format.

It is easy in principle to assemble an imaging polarimeter, but quite difficult to obtain accurate results. Each of the calibration issues is time consuming, and often maddeningly coupled into each other.

Currently the UAH imaging polarimeter is able to measure Stokes images, degree of polarization images, degree of linear polarization images, degree of circular polarization images, and images showing the orientation of the major axis of a polarization ellipse. A preliminary calibration has been done on the QWLR and LP at 633 nm. Soon, the polarimeter will measure Mueller matrices at 633 nm and 849 nm. A study on the performance of polarizing beam splitter cubes as a function of field angle is in progress. We also intend to study depolarization, the coupling of polarized light into unpolarized light, in optical systems.

7. Acknowledgements

We would like to acknowledge the Air Force Office of Scientific Research AFOSR (contract #AFOSR-89-0542) for their support in this work. We would also like to thank AT&T Bell Labs and Michael Prise for their assistance.

8. References

1. R.A. Chipman, "Polarization ray tracing," in *Recent Trends in Optical Design; Computer Lens Design Workshop* C. Londono and R.E. Fischer, eds., Proc. SPIE **766**, 61-68 (1987).
2. R.A. Chipman, "Polarization analysis of optical systems," *Opt. Eng.* **28**, 90-99 (1989) and R.A. Chipman, "Polarization analysis of optical systems II," Proc. SPIE **1166**, 79-94 (1989).

3. J.P. McGuire, Jr. and R.A. Chipman, "Polarization aberrations in optical systems," *Current Developments in Optical Engineering II*, R. Fischer, W. Smith, Editors, Proc. SPIE **81**, 240 (1987).
4. R.A. Chipman and L.J. Chipman, "Polarization aberration diagrams," *Opt. Eng.* **28**, 100-106 (1989).
5. F.B. McCormick and M.E. Prise, "Optical circuitry for free-space interconnections," Applied Optics, **29**, 2013-2018 (1990).
6. M.E. Prise, N.C. Craft, R.E. LaMarche, M.M. Downs, S.J. Walker, L.A. D'Asaro, and L.M.F. Chirovsky, "Module for optical logic circuits using symmetric self_electrooptic effect devices," Applied Optics, **29**, 2164-2170 (1990).
7. A. Dickinson and M.E. Prise, "Free-space optical interconnection scheme," Applied Optics, **29**, 2001-2005 (1990).
8. M.J. Hagyard, N.P. Cumings and E.A. West, "The new MSFC solar vector magnetograph," Proceedings of Cunming Workshop on Solar Physics and Interplanetary Traveling Phenomena, C.deJager and Chen Biao, eds., 1216 - 1225, Science Press, (1985).
9. M.J. Duggin, S.A. Israel, V.S. Whitehead, J.S. Myers, and D.R. Robertson, "Use of polarization methods in earth resources investigations," Proc. SPIE **1166**, 11-22, (1989).
10. W.G. Egan, "Polarization in remote sensing II," Proc. SPIE **1166**, 23-32, (1989).
11. D.B. Chenault and R.A. Chipman, "Linear diattenuation and retardance measurements in an infrared spectropolarimeter," Proc. SPIE **1317** (this proceedings), (1990).
12. D.H. Goldstein, "Polarization modulation in infrared electrooptic materials," Ph.D Dissertation, Dept. of Physics, University of Alabama in Huntsville, (1990).
13. V.J. Iafelice and W.S. Bickel, "Polarized light-scattering matrix elements for select perfect and perturbed optical surfaces," Applied Optics, **26**, 2410-2415, (1987).
14. V.J. Iafelice and W.S. Bickel, "Polarized light scattering matrix elements for micron-sized rectangular aluminum lines on reflecting optical surfaces," Applied Optics, **26**, 1799-1805, (1987).
15. R.M.A. Azzam, "Photopolarimetric measurement of the Mueller matrix by Fourier analysis of a single detected signal," Optics Letters **48**, 148-150 (1990).
16. P.S. Hauge, "Mueller matrix ellipsometry with imperfect compensators," J. Opt. Soc. Am. **68**, 1519-1528 (1978).
17. D.B. Goldstein and R. A. Chipman, "An error analysis of a Mueller matrix polarimeter," J. Opt. Soc. Am. A. **7**, 693-700 (1990).
18. M.F. Morgan and R.A. Chipman, "An ultraviolet polarimeter for characterization of an imaging spectrometer," Proc. SPIE **1317** (this proceedings), (1990).

19. H. Kubota and S. Inoue, "Diffraction images in the polarizing microscope," J. Opt. Soc. Am. **49**, 191-198 (1959).
20. E.W. Hansen, "Overcoming polarization aberrations in microscopy," Proc. SPIE **891**, 190-197, (1988).
21. D.M. Brown and R.A. Chipman "Evaluation of x-ray telescope for polarimetry," Proc. SPIE **1317** (this proceedings), (1990).
22. T.P. Washburn, M.J. Konopnicki, and T.D. Miller, "Far-field diffraction effects of large-aperature laser systems due to polarization effects caused by multilayer dielectric mirror coatings," Proc. SPIE **1166**, 340-345, (1989).

Appendix B

Draft of a paper to be submitted to Applied Optics

Angular dependence of polarizing beam splitter cubes

J. Larry Pezzaniti

Russell A. Chipman

Dept. of Physics
University of Alabama in Huntsville
Huntsville, AL 35899

This is a preliminary draft of a paper to be submitted to Applied Optics

Angular dependence of polarizing beam splitter cubes

J. Larry Pezzaniti

Russell A. Chipman

Dept. of Physics

University of Alabama in Huntsville

Huntsville, AL 35899

Sept. 17, 1991

Angular dependence of polarizing beam splitter cubes

Abstract

A method to measure the angular properties of polarizing beam splitters was developed for characterizing polarizing beam splitters used in polarization based imaging systems. Several performance characteristics, such as transmission, reflection, leakage, and variation of the orientation of linear polarization were measured with an imaging polarimeter. Measurements were made over a 10° range of angle of incidence simultaneously on three commercially available polarizing beam splitters, and one specifically designed for a wide angular field of view. Variation of the orientation of linear polarization of polarizing beam splitters is described. Derivation of the Mueller matrix of a polarizing beam splitter is provided in an Appendix.

I. Introduction

An ideal polarizing beam splitter divides the incident light into s and p polarization states, transmitting the p polarized component and reflecting the s polarized component. Polarizing beam splitters have a limited range of angle of incidence and wavelength for which they are effective. Typically, polarizing beam splitter designs are optimized to provide a large spectral range within a small angular field of view. For example, the Macneille polarizing beam splitter design achieves extinction ratios of greater than 100:1,

but the beam must be collimated to within ±2° of the entrance face normal.*[1][2]* Applications which involve imaging or non-collimated light, however, may require the polarizing beam splitter to have a wide field of view, often with quasimonochromatic light.

The angular behavior of polarizing beamsplitters is the subject of this paper. The objective is to characterize polarizing beam splitter behavior in polarization based imaging systems, specifically optical computers. For example, several free space optical interconnects utilize the polarizing beam splitter's four port access to losslessly interlace and divide arrays of beams carrying logic information.*[3][4][5][6][7][8]* In these systems, 2-D logic arrays are interconnected by imaging arrays of spots (generated by binary phase gratings) from one device to the next. The logic devices are situated in image planes and the polarizing beam splitters are located in planes at or near the pupil where the light is collimated. Collimated light from each element of a logic array passes through the polarizing beam splitters at a different angle. Presently, the above referenced systems operate at ±3° field of view, but future systems will be extended to the largest fields of view permissible, ±10° or more. Since most system designs require each beam to pass through several polarizing beam splitters, the system efficiency depends on the angular response of the polarizing beam splitters. Furthermore, light incorrectly divided at the polarizing beam splitter will usually be imaged onto an incorrect logic element or detector.

This paper introduces phenomenological data taken on three commercially available polarizing beam splitters and one polarizing beam splitter specifically designed for a field of view of ±7°*[9]*. Six performance parameters are measured for each polarizing beam splitter using an imaging polarimeter*[10]*. The polarizing beam splitters are measured in transmission and reflection over a ±10° field of view.

One aspect of polarizing beam splitters examined by this paper is the dependence of

orientation of linear polarization on ray angle of incidence. In Section II we provide a concise explanation of how and why the orientation of linear polarization in the reflected and transmitted beams depend on ray angle of incidence. Section III introduces the six figures of merit which we measured on each of the four polarizing beam splitters. Section IV describes our imaging polarimeter and the procedures used to measure the angular dependence of the polarizing beam splitters. Section V presents the data on the polarizing beam splitters. Finally, Appendix A derives the Mueller matrix of a polarizing beam splitter in transmission and reflection in terms of the complex transmission and reflection coefficients of the beamsplitting interface, relating our measurements, the Mueller calculus, and the quantities calculated by thin film analysis codes, s and p reflectance, transmittance, and phase difference.

II. Variation of the Orientation of Linear Polarization

A polarizing beam splitter cube is formed by coating the hypotenuse face of an isosceles right-angled prism with a number of thin-film layers and then cementing it to an identical uncoated prism. The usual design of the multi-layer has been of the form initially devised by Macneal *[1]* and consists of alternate layers of a high and a low refractive index material. The optical thickness of each layer is equal to a quarter of the design wavelength at the angle of refraction in that layer, and the refractive indices of the thin-film materials as well as that of the substrate are chosen so that the light is incident upon each of the multi-layer at the Brewster angle *[11][12][13]*. Due to Brewster's condition the reflectance of the p polarization approaches zero while the reflectance of the s polarization remains high. Angles of incidence different from 45°, however, changes the optical path

length from the quarter wave configuration, and Brewster's condition no longer holds. This causes a leakage of s polarization in transmission and p polarization in reflection. References *[14][15]* contain two different approaches to polarizing beam splitter multi-layer design to increase the angular range for which the p transmittance and s reflectance remain high.

The orientation of linear polarization transmitted from a polarizing beam splitter is dependent on the ray angle of incidence. If a spherical wave of unpolarized light is incident on a polarizing beam splitter, the reflected and transmitted beams will have a spatially varying linear polarization. This is because the orientation of linear polarization of a polarizing beam splitter aligns with the plane of incidence (p plane) in transmission and the s direction in reflection, while the s and p orientations depend on the ray's angle of incidence.

Figure 1 introduces a coordinate system for a polarizing beam splitter cube. The origin is centered on the entrance face with the z axis normal to the face. The beam splitting interface normal lies in the x-z plane and is 45° from the z axis. The direction of an incident ray is specified by its refracted direction cosines (l, m, n) where $l = \cos\alpha$, $m = \cos\beta$ and $n = \cos\gamma$ and $l^2 + m^2 + n^2 = 1$. α, β, and γ are illustrated in Figure 1. For rays incident such that $\beta = 90°$, the p direction is parallel to the x-z plane (we will refer to this as the horizontal plane) and the s direction aligns with the y-z plane (vertical). For angles of incidence in which $\beta > 90°$, the p plane rotates counterclockwise with the respect to the horizontal, while for $\beta < 90°$ it rotates clockwise. Figure 2 illustrates the orientation of s and p directions as functions of the direction cosines of the incident rays. In Figure 2, α increases from 90° in the positive x direction and β increases from 90° in the positive y direction. The thin cross hairs are parallel with the horizontal and vertical planes (x-z and

y-z planes in Figure 1). The large circles indicate the zones where the angles of incidence are $\gamma = 5°$ and $\gamma = 10°$. The angle ϕ is the angle between the p direction and the horizontal x-z plane.

Consider an ideal polarizing beam splitter which transmits 100% of the p polarized light and reflects 100% of the s polarized light for all angles of incidence. Two examples readily illustrate the polarization aberration which polarizing beam splitters can introduce in imaging systems: 1. a spherical wave of linearly polarized light, and 2. a polarizing beam splitter at the pupil of an 4F optical filtering system. For the first case, consider light uniformly polarized parallel to the x-z plane focused through a polarizing beam splitter. The situation is illustrated in Figure 3. The s-p coordinates rotate for rays in which $\beta = 90°$. The intensity of each ray transmitted depends on the angle ϕ between the linear polarization direction of the incident ray and the p direction at the beamsplitting interface. According to Malus's law the transmitted intensity of a ray is

$$I(\phi) = I_0 \mathrm{Cos}^2\phi \qquad (1)$$

where ϕ is a function of the incident rays direction cosines, and I_0 is the incident intensity. Eqn. A11 in Appendix A contains an analytic expression for $\phi(l, m, n)$. An ideal polarizing beam splitter cube introduces apodization and a spatial variation of linear polarization orientation, aligned with p or s directions, in the transmitted and reflected beam.

For the second example, consider a polarizing beam splitter situated between infinite conjugate object and image planes. Each object point is linearly polarized parallel to the horizontal plane. Since light from each object point is collimated before entering the polarizing beam splitter, every ray from a given object point encounters the same s-p coordinate orientation. In this situation, the polarization state from each object point is

transformed uniformly by the polarizing beam splitter. Figure 4 shows how the polarization direction of a set of linearly polarized object points are rotated by the polarizing beam splitter. The intensity of each object point is transmitted by the polarizing beam splitter according to

$$I(\phi) = I_0 \mathrm{Cos}^2(\phi) \qquad (2)$$

where ϕ is again the rotation of the p direction from the horizontal plane, and the direction cosines specify a plane wave direction. The polarizing beam splitter introduces a nonuniform intensity distribution in the image plane and variation of polarization direction across the image.

The transmission and reflection properties of a polarizing beam splitter can be written in terms of its Mueller matrix which is a function of wavelength and angle of incidence. Appendix A derives the Mueller matrices in transmission and reflection of a polarizing beam splitter in terms of the parameters generally calculated by thin film analysis programs, the s and p transmittance and reflectance, and the retardance in transmission and reflection. These Mueller matrices include the effect of the rotation of s-p coordinates with incident angle and may be used to facilitate theoretical comparisons of experimental results.

III. Figures of merit for a polarizing beam splitter

In this section, six figures of merit which characterize the performance of polarizing beam splitters are defined. Measurements of these figures of merit are reported in section V.

The figures of merit defined in this section are measurements which determine how a polarizing beam splitter transmits and reflects two incident polarization states. The first polarization state is linearly polarized parallel to the horizontal x-z plane and the second is

parallel to the vertical y-z plane (refer to Figure 1). We will refer to these directions as horizontal $\hat{h}$ and vertical $\hat{v}$. For an axial ray along the z axis the $\hat{h}$ is aligned with p direction and the $\hat{v}$ direction aligns with the s direction.

The figures of merit are measured as functions of direction cosines (l, m, n) defined in Figure 1. The measurements are shown in Figures 6 - 9. The figures of merit are:

1. Transmission efficiency TE - the fraction of linearly polarized light in the $\hat{h}$ direction which is transmitted into the $\hat{h}$ state.
2. Transmission couplance TC - the fraction of incident linearly polarized light in the $\hat{h}$ direction that is transmitted into the $\hat{v}$ state.
3. Transmission leakage TL - the fraction of linearly polarized light in the $\hat{v}$ direction that is transmitted.
4. Reflection efficiency RE - the fraction of linearly polarized light in the $\hat{v}$ direction that is transmitted into the $\hat{v}$ state.
5. Reflection couplance RC - the fraction of linearly polarized light in the $\hat{v}$ direction that is reflected into the $\hat{h}$ state.
6. Reflection leakage RL - the fraction of linearly polarized light in the $\hat{h}$ direction that is reflected.

Transmission and reflection efficiency represents the fraction of light that takes the correct path at the polarizing beam splitter and remains in the correct polarization state. Transmission and reflection leakage gives the fraction of light that takes the incorrect path at the polarizing beam splitter. Transmission and reflection couplance is the fraction of light that takes the correct path, but is coupled into the orthogonal polarization direction.

The complete experimental polarization description of a polarization element is in terms of the Mueller Matrix. The Mueller matrix for a polarizing beam splitter in

transmission is M_t, and the Mueller matrix for reflection is M_r, both of which are functions of wavelength and angle of incidence.

$$M_t(l,m,n,\lambda)=\begin{pmatrix} m_{11}^t & m_{12}^t & m_{13}^t & m_{14}^t \\ m_{21}^t & m_{22}^t & m_{23}^t & m_{24}^t \\ m_{31}^t & m_{32}^t & m_{33}^t & m_{34}^t \\ m_{41}^t & m_{42}^t & m_{43}^t & m_{44}^t \end{pmatrix}, \qquad M_r(l,m,n,\lambda)=\begin{pmatrix} m_{11}^r & m_{12}^r & m_{13}^r & m_{14}^r \\ m_{21}^r & m_{22}^r & m_{23}^r & m_{24}^r \\ m_{31}^r & m_{32}^r & m_{33}^r & m_{34}^r \\ m_{41}^r & m_{42}^r & m_{43}^r & m_{44}^r \end{pmatrix}. \tag{3}$$

Although the Mueller matrices provide a complete description, they are not necessarily the clearest or most appropriate description for all purposes. For polarizing beam splitters, the six figures of merit are readily measured and convey the most important information. The relationship of each figure of merit to the corresponding Mueller matrix elements is given in Table 1. The relationship of the figure of merit to the complex amplitude transmission and reflection coefficients are also given in Table 1. The corresponding derivations are given in Appendix A.

IV. Imaging polarimeter configuration and measurement procedure

Figure 3 shows the configuration of an imaging polarimeter used to measure the angular dependence of a polarizing beam splitter. The light source is a 850 nm wavelength diode laser. The beam is focused on a rotating ground glass disk to scramble the temporal coherence of the beam. The beam is collimated and passes through a silver glass polarizer (the polarization state generator) which is mounted in a rotary stage. A lens prepares a converging spherical wave with a 10° half angle and is incident on the polarizing beam splitter. The beam transmitted (reflected) by the polarizing beam splitter is collimated and passes through a second silver glass polarizer (polarization state analyzer). By moving the

polarizer/camera the same polarizer and camera are used to make measurements both in transmission and reflection.

The aperture stop (see Figure 3) of the system is imaged onto the ccd. Accordingly, each pixel represents an angular ray path though the polarizing beam splitter with direction cosines (l, m). By measuring the polarizing properties on a pixel by pixel basis the polarizing beam splitter is characterized as a function of the direction cosines of incident light.

Each image is converted into a reduced resolution data set by collapsing 4 x 5 pixel regions into single pixels (super-pixels). The unequal dimensions of the averaged pixels compensate for the 5:4 aspect ratio of the ccd. Super-pixels also reduce the intensity variation due to speckle on the ccd and decrease the effect of beam wander due to any wedge (prism) in the rotating polarization elements. High spatial resolution is not important for these measurements since the field of view dependence of polarizing beam splitter cubes varies slowly with angle of incidence.

To control system operation, capture and process images, and display the results, a PC 386 computer is used with the following peripherals: a 512 X 512 video frame grabber board with 8-bit resolution in conjunction with a visible/near infrared monochrome ccd camera. Data reduction is performed with high precision floating point processing in PC memory. A color monitor is used to display measured frames in false color.

V Measurements of the polarizing beam splitter

Six figures of merit, described in section III, were made on four different polarizing beam splitters. The plots in Figures 6-9 are measures of the angular dependence over a

±10° field of view. Figures 6-8 contain measurements made on three different commercially available polarizing beam splitters from Melles-Griot, Newport and CVI. Measurements on a polarizing beam splitter designed at AT&T Bell Labs specifically to operate over a ±7° field of view is shown in Figure 9.

Each figure of merit involves two measurements. In the first measurement, the polarization analyzer and generator are oriented with their transmission axes along the horizontal $\hat{x}$ or vertical $\hat{y}$ directions (refer to Figure 1), according to which figure of merit is to be measured. An image of the exit pupil is digitized and stored. The image is then divided by the total incident intensity to obtain the fraction of light transmitted or reflected from the polarizing beam splitter cube.

The coordinate system used in these plots is common to both the plots and the polarizing beam splitter shown in Figure 1. Direction cosine α l increases from 90° l in the positive x direction, β l increases from 90° l in the positive y direction and γ l increases from 0° l radially. The large circles indicate the zones where the angles of incidence are $\gamma = 5°$ and $\gamma = 10°$. The data is plotted as functions of angle of incidence on the entrance face of the cube (in air).

The polarizing beam splitters were measured with incident horizontal and vertical polarized light, i.e. polarized in the x-z and y-z planes (refer to Figure 1). Along the x axis, the s-p coordinates align with the vertical and horizontal directions i.e., along the x axis the s and p transmittances and s and p reflectances ($\alpha_{s,t}, \alpha_{p,t}, \alpha_{s,r}, \alpha_{p,r}$) of the multi-layer are represented. The positive x axis corresponds to an increase in angle of incidence a beam makes with the normal to the beam splitting interface, as large as 55° in air, in the positive x direction, and as small as 35° in the negative x direction. We will now concentrate our discussion along the x axis.

The polarizing beam splitters exhibited much wider angular bandwidth for s polarization than p polarization. The angular response of p polarized light varied widely among the measured polarizing beam splitters. Here angles of incidence will be given relative to the entrance face normal, positive angles increasing in the positive x direction. The Melles-Griot cube exhibited three p state transmission peaks at -10°, -2° and 9° (Figure 6a). Multiple maxima are indicative of field widening. Transmission falls to under 80% at 5°. The s reflectance was very constant over the measured angular range, about 96% (Figure 6b). A p reflectance maximum is found at 5° (Figure 6c), corresponding to the decrease in p transmission at 5°. The s transmittance (Figure 6d) was below 1% for all angles of incidence. As expected, coupling between s and p polarizations was very small, below 1% (Figures 6e, 6f). Coupling between s and p not expected since the beamsplitting interface is isotropic and homogeneous.

The Newport polarizing beam splitter exhibited a flat angular response to p polarization for positive angles of incidence in transmission, but the p transmittance fell to 22% at -10° (Figure 7a). The s reflectance of was 96% from -10° to 10° (Figure 7b). A sharp increase in p reflectance occurs in the negative direction (Figure 7c), explaining the sharp decrease off observed in transmission. S transmittance was small and angle insensitive (Figure 7d). The couplance between s and p polarizations is below 1% (Figure 7e, 7f).

The p transmittance of the CVI polarizing beam splitter peaked at 91% and decreases rapidly in both directions (Figure 7a). The s reflectance was nearly 98% over the range of angle of incidence (Figure 7b). The p reflectance increases correspond to the p transmittance decreases (Figure 7c). S transmittance was under 1% for all angles of incidence (Figure 7d). Couplance between s and p is below 1%.

The AT&T polarizing beam splitter was designed to operate over a ±7° field of view. P transmittance was greater than 96% form -10° to 7°. The s reflectance varied from 97% at -10° to 91% at 10°. The p reflectance exhibits an increase from 1% at 5° to 7% at 10°, and is under 1% everywhere else. The s transmittance increases from 2% at 5° to 6% at 10°. The couplance between s and p is under 1%.

The orientation of s and p directions change at the beam splitting interface for angles of incidence in which $y \neq 0$. This property, explained in detail in section II, is inherent to the geometry of the polarizing beam splitter cube and degrades the performance in several ways. First, the efficiency at which the polarizing beam splitters transmitted horizontally polarized light and reflected vertically polarized light was decreased (Figures 6-9, a,b). Second, the leakage of horizontally polarized light in reflection and vertically polarized light in transmission increased (Figures 6-9, c,d). Finally, transmitted horizontally polarized light was coupled into vertical and reflected vertically polarized light was coupled into horizontal (Figures 6-9, e,f).

The polarization purity of transmitted and reflected beams is influenced by both transmittance and reflectance variations of the beamsplitting interface and the varying orientation of s-p coordinates. For example, for the Melles-Griot polarizing beam splitter the purity of transmitted horizontally polarized light variations for horizontally polarized light incident, the purity of transmitted horizontally polarized light varies between 160:1 to 130:1. The orientation variation causes a dramatic drop in polarization purity down to 30:1. In reflection, the polarization purity along the x axis remains constant at about 300:1, but drops to 20:1 due to the rotation of s-p directions.

The accuracy of our measurements are limited by the A-D conversion of the 8-bit camera used. We have not attempted to verify our measurements theoretically from the

equations in Appendix A, as the thin film designs of the polarizing beam splitters are not available to us. The measurements serve to show the over-all angular behavior of the cube and to demonstrate the spatial variation of linear polarization inherent to polarizing beam splitters. The occasional abrupt changes in the data may be due to coating thickness variations and\or experimental error.

V. Summary

An examination of several polarizing beam splitter cubes has shown that all are far from their ideal performance. The polarizing beam splitter cube is intended to divide the incident beam based on its polarization state. In its usual orientation (beamsplitting interface normal in the plane parallel to our optical table), it should transmit the horizontal component of the incident light, and reflect the vertical component. However, a fraction of the vertically polarized light is leaked in transmission, a fraction of horizontally polarized light is reflected, and some fraction of the light which takes the intended path has its plane of polarization rotated.

The shortcomings of any polarizing beam splitter has its source in several places, (1) the inherent geometry of the cube, (2) the transmission and reflection coefficients for the interface, and (3) fabrication and tolerancing difficulties.

The inherent geometry of the polarizing beam splitter cube arises because the polarizing beam splitter performs its task in the local s-p coordinate system, and not in the global x-y coordinate system. If we were to illuminate it with a beam with the correct spatial variation of polarization, the ideal cube would transmit all of the p-component, and reflect all the s-component, and divide our beams exactly as desired.

The second shortcoming arises because the reflecting and transmitting properties of the interface, its Fresnel coefficients or amplitude transmission relations, vary with angle of incidence and wavelength. There can only be a limited angular bandwidth and wavelength bandwidth over which acceptable performance is achieved. In our data sets, the variations of the Fresnel coefficients with angle of incidence is clearly measured along the x-axis of our graphs. As the angle of incidence decreases, the performance tends to decrease rapidly, as it must. At zero angle of incidence, a homogeneous and isotropic thin film coating cannot function as a polarizing beamsplitting interface. Performance tends to stay good for much further toward increasing angle of incidence. Thus many of the polarizing beam splitters are improved if we tilt them slightly to increase the internal angle of incidence.

We see in the data the great pains taken by the thin film designers to increase the fields of view. Several cubes have Fresnel coefficients which dip, then come back up, indicating that they have been optimized to have several peaks. This increases the overall field, at the expense of performance near the center. (If the maxima were moved closer together, it would operate better over a small field, than with the maxima further apart.)

Appendix A: Mueller matrix of a polarizing beam splitter

Here we derive the Mueller matrix for a non-depolarizing, polarizing beam splitter and use the result to find the figures of merit listed in Table 1 in terms of the complex amplitude transmission and reflection coefficients of the beamsplitting interface.

The effect of an optical system (element) on the polarization of incident light is most generally expressed by

$$S' = MS \qquad (A.1)$$

where S and S′ are the 4 x 1 Stokes vectors of the incident and transmitted light, respectively, and M is the 4 x 4 real Mueller matrix that characterizes the linear interaction of the light with a polarizing optical element.*[16]* The elements of the Stokes vector are defined as

$$S = \begin{pmatrix} s_0 \\ s_1 \\ s_2 \\ s_3 \end{pmatrix} = \begin{pmatrix} (\langle E_h \rangle^2 + \langle E_v \rangle^2) \\ (\langle E_h \rangle^2 - \langle E_v \rangle^2) \\ 2\langle E_h \rangle \langle E_v \rangle \cos\gamma \\ 2\langle E_h \rangle \langle E_v \rangle \sin\gamma \end{pmatrix}, \qquad (A.2)$$

where E_h and E_v are projections of the electric field on the $\hat{h}$ and $\hat{v}$ axes and γ is the difference in phase between the $\hat{h}$ and $\hat{v}$ polarizations. The Mueller matrix of an optical system (element) is a function of wavelength and of the angles of the incident light. The response of an optical system to a collection of spherical waves of arbitrary polarization is generally treated on a ray by ray basis and can be written as a Mueller matrix $M(\vec{H}, \vec{\rho}, \lambda)$ as a function of object coordinate $\vec{H}$, pupil coordinate $\vec{\rho}$, and wavelength λ.*[17,18]*

Two separate matrices are needed to describe field of view polarization properties of a polarizing beam splitter cube: M_t describes the beam splitter in transmission, and M_r characterizes it in reflection. The Mueller matrices in transmission and reflection for an ideal polarizing beam splitter illuminated at normal incidence are:

$$M_t = \frac{1}{2}\begin{pmatrix} 1 & 1 & 0 & 0 \\ 1 & 1 & 0 & 0 \\ 0 & 0 & 0 & 0 \\ 0 & 0 & 0 & 0 \end{pmatrix} \qquad M_r = \frac{1}{2}\begin{pmatrix} 1 & -1 & 0 & 0 \\ -1 & 1 & 0 & 0 \\ 0 & 0 & 0 & 0 \\ 0 & 0 & 0 & 0 \end{pmatrix} \qquad (A.3)$$

These are the Mueller matrices for a horizontal linear polarizer and a vertical linear polarizer*[16]*, so the polarizing beam splitter transmits horizontally polarized light $S = (1, 1, 0, 0)$ and reflects vertically polarized light $S = (1, -1, 0, 0)$.

In transmission, the Mueller matrix for a linear partial polarizer, which may also display linear birefringence is *[16]*

$$M = \frac{1}{2}\begin{pmatrix} A & B & 0 & 0 \\ B & A & 0 & 0 \\ 0 & 0 & C\cos\delta_t & C\sin\delta_t \\ 0 & 0 & -C\sin\delta_t & C\cos\delta_t \end{pmatrix}. \qquad (A.4)$$

where

$$A = \rho^2_{p,t}(\theta,\lambda) + \rho^2_{s,t}(\theta,\lambda),$$

$$B = \rho^2_{p,t}(\theta,\lambda) - \rho^2_{s,t}(\theta,\lambda), \qquad (A.5)$$

$$C = 2\rho_{p,t}(\theta,\lambda)\rho_{s,t}(\theta,\lambda),$$

and $\rho_{p,t}(\theta,\lambda)$ and $\rho_{s,t}(\theta,\lambda)$ are the amplitude transmittances for p and s light, and we explicitly consider that the amplitude transmittance and retardance are functions of angle of incidence and wavelength. $\delta_t = \delta_{p,t} - \delta_{s,t}$, the difference in accumulated phase in transmission between p and s components, is the linear retardance of the interface. θ is the refracted ray angle of incidence with respect to the surface normal of the beamsplitting interface, given by

$$\theta(l,m,n) = Arccos\left(\frac{1}{\sqrt{2}}(n' - l')\right) \qquad (A.6)$$

where (l, m, n) are the incident ray direction cosines in air and (l', m', n') are the direction cosines in glass of the ray after refracting at the front face of the beamsplitter

cube given by

$$l' = l, \qquad m' = m, \tag{A.7}$$

$$n' = n + n_c\sqrt{\left(\frac{n_0}{n_c}n\right)^2 - \left(\frac{n_0}{n_c}\right)^2 + 1} \; - n_c n, \tag{A.8}$$

where n_c is the index of refraction of the glass substrates and n_0 is the index of refraction before the cube (generally air).

In reflection, the Mueller matrix (Eqn. *A4*) is evaluated using the reflection parameters

$$\begin{aligned} A &= \rho_{p,r}^2(\theta,\lambda) + \rho_{s,r}^2(\theta,\lambda), \\ B &= \rho_{s,r}^2(\theta,\lambda) - \rho_{p,r}^2(\theta,\lambda), \\ C &= 2\rho_{p,r}(\theta)\rho_{s,r}(\theta,\lambda), \end{aligned} \tag{A.9}$$

and $\rho_{p,r}(\theta,\lambda)$ and $\rho_{s,r}(\theta,\lambda)$ are the reflectances for p and s light respectively, and δ_t is replaced with δ_r, the linear retardance between p and s in reflection.

The incident and transmitted Stokes vectors are defined in $\hat{v} - \hat{h}$ coordinates. To apply the Mueller matrix on the Stokes vector, the Stokes vector must first be rotated into local s-p coordinates of the beamsplitting interface. This is accomplished by a simple coordinate rotation about the normal to the beamsplitting interface

$$S_{s,p} = R(\phi)S_{h,v}, \tag{A.10}$$

where ϕ is the angle between horizontal and p directions

$$\phi(l,m,n) = Arccos\left(\frac{1}{\sqrt{2}}\frac{1}{\sin\phi(l,m,n)}(l' + n')\right). \tag{A.11}$$

$R(\phi)$ is the matrix for a rotational change of basis for the Mueller calculus*[16]*,

PAGES _____

ARE

MISSING

IN

ORIGINAL

DOCUMENT

Figure 1 Geometry of a polarizing beam splitter. Side (a,b,c,d) is the entrance face. (a,e,g,d) is the beam splitting interface. The transmitted beam exits the face (f,e,g) while the reflected light exits at (b,e,g,c). An incident ray is identified by its direction cosines (l, m, n) defined as $l = \cos\alpha$, $m = \cos\beta$, and $n = \cos\gamma$. α is the angle between the x axis and the ray. β btween the y axis and the ray, γ between the z axis and the ray. We refer to the x-z plane as the horizontal and the y-z plane is vertical. The origin of the x-y-z coordinate system is located at the center of the entrance face. The cube is placed in the imaging polarimeter with the horizontal plane parallel to the table top.

Figure 2 Orientation of the s and p directions on the beamsplitting interface of a polarizing beam splitter plotted as a function of beam angle of incidence on the cube face. The orientation of the beam splitting interface is shown in Figure 1. Figures 1 and 2 share the same coordinate system. α increases from 90° in the positive x direction. β increases from 90° in the positive y, and the large circles indicate the zones where the angles of incidence are $\gamma = 5°$ and $\gamma = 10°$. Incident rays for which $\beta > 90°$ involve a counterclockwise rotation of s-p coordinates and rays in which $\beta < 90°$ the rotation is clockwise. The polarizing axis is parallel to the p direction in transmission and the s direction in reflection. Polarizing beam splitters have a spatially varying orientation of linear polarization.

Figure 3 Polarization aberration introduced into a converging wavefront focued through an ideal polarizing beam splitter. Incident on the polarizing beam splitter is a shperical wave linearly polarized in the horizontal x-z plane. The transmission axis of a polarizing beam splitter depends on ray angle of incidence and is aligned with the p direction at the beam splitting interface. The variation of p direction with angle of incidence is illustrated in Figure 2. The incident polarization direction is shown in plot 3a, and the variation of linear polarization across the transmited spherical wave is shown plot 3b. Variation of p direction with angle of incidence introduces apodization and spatially varying linear polarization into uniformly polarized spherical wavefronts.

Figure 4 A ideal polarizing beam splitter is situated in collimated space between conjugate planes. In this situation a polarizing beam splitter introduces intenstity non-uniformity and polarization variation into the image. Light from each object point is collimated and is incident at the polarizing beam splitter at different angle. The variation of p direction with angle of incidence (described in Figure 2) introduces polarization direction variation in the image plane.

Figure 5 Configuration of the Imaging Polarimeter used to measure four polarizing beam splitters at 849nm over a $\pm 10°$ field of view. The source is a 849nm laser diode. The dashed line shows the path of the chief ray. The stop of the system is imaged on to the CCD detector and is at the lens located just after the polarizing beam splitter under test. The polarizing beam splitter is characterized as a function of angle of incidence by computing figures of merit on a pixel by pixel basis.

Figure 6 Angular Performance of a Melles-Griot 830 nm polarizing beam splitter measured at 850 nm. The plots on the left are for horizontally polarized incident light, the plots on the right are for vertically polarized incident light.

(a) Transmission efficiency ($\hat{h} \rightarrow \hat{h}$) (b) Reflection efficiency ($\hat{v} \rightarrow \hat{v}$)
(c) Reflection Leakage ($\hat{h} \rightarrow \hat{h} + \hat{v}$) (d) Transmission Leakage ($\hat{v} \rightarrow \hat{v} + \hat{h}$)
(e) Transmission Couplance ($\hat{h} \rightarrow \hat{v}$) (f) Reflection Couplance ($\hat{v} \rightarrow \hat{h}$)

(a) (b) (c) (d) (e) (f)

Figure 7 Angular Performance of a Newport broad band polarizing beam splitter measured at 850 nm. The plots on the left are for horizontally polarized incident light, the plots on the right are for vertically polarized incident light. The plots are:

(a) Transmission efficiency ($\hat{h} \rightarrow \hat{h}$) (b) Reflection efficiency ($\hat{v} \rightarrow \hat{v}$)
(c) Reflection Leakage ($\hat{h} \rightarrow \hat{h} + \hat{v}$) (d) Transmission Leakage ($\hat{v} \rightarrow \hat{v} + \hat{h}$)
(e) Transmission Couplance ($\hat{h} \rightarrow \hat{v}$) (f) Reflection Couplance ($\hat{v} \rightarrow \hat{h}$)

(a) (b) (c) (d) (e) (f)

Figure 8 Angular Performance of a CVI polarizing beam splitter measured at 850 nm. The plots on the left are for horizontally polarized incident light, the plots on the right are for vertically polarized incident light. The plots are:

(a) Transmission efficiency ($\hat{h} \rightarrow \hat{h}$) (b) Reflection efficiency ($\hat{v} \rightarrow \hat{v}$)
(c) Reflection Leakage ($\hat{h} \rightarrow \hat{h} + \hat{v}$) (d) Transmission Leakage ($\hat{v} \rightarrow \hat{v} + \hat{h}$)
(e) Transmission Couplance ($\hat{h} \rightarrow \hat{v}$) (f) Reflection Couplance ($\hat{v} \rightarrow \hat{h}$)

(a) (b) (c) (d) (e) (f)

Figure 9 Angular Performance of a polarizing beam splitter desinged at AT&T Bell Labs to operate over 7° field of view. Measurements made at 850 nm. The plots on the left are for horizontally polarized incident light, the plots on the right are for vertically polarized incident light. The plots are:

(a) Transmission efficiency ($\hat{h} \rightarrow \hat{h}$) (b) Reflection efficiency ($\hat{v} \rightarrow \hat{v}$)
(c) Reflection Leakage ($\hat{h} \rightarrow \hat{h} + \hat{v}$) (d) Transmission Leakage ($\hat{v} \rightarrow \hat{v} + \hat{h}$)
(e) Transmission Couplance ($\hat{h} \rightarrow \hat{v}$) (f) Reflection Couplance ($\hat{v} \rightarrow \hat{h}$)

(a) (b) (c) (d) (e) (f)

Figure of Merit	Corresponding Mueller matrix expression	Corresponding amplitude coefficient expression
Transmission efficiency $TE(\alpha,\beta)$	$\frac{1}{2}(m^t_{11}+m^t_{12}+m^t_{21}+m^t_{22})$	$\rho^2_{p,t}\cos^4\beta+\rho^2_{s,t}\sin^4\beta+2\rho_{o,t}\rho_{s,t}\sin^2\beta\cos^2\beta\cos\delta_t$
Transmission leakage $TL(\alpha,\beta)$	$\frac{1}{2}(m^t_{11}-m^t_{12})$	$\frac{1}{2}(\rho^2_{p,t}\cos^2\beta+\rho^2_{s,t}\sin^2\beta)$
Transmission couplance $TC(\alpha,\beta)$	$\frac{1}{2}(m^t_{11}+m^t_{12}-m^t_{21}-m^t_{22})$	$\sin^2\beta\cos^2\beta(\rho^2_{p,t}+\rho^2_{s,t}-2\rho_{p,t}\rho_{s,t}\cos\delta_t)$
Reflection efficiency $RE(\alpha,\beta)$	$\frac{1}{2}(m^r_{11}-m^r_{12}-m^r_{21}+m^r_{22})$	$\rho^2_{s,r}\cos^4\beta+\rho^2_{p,r}\sin^4\beta-2\rho_{s,r}\rho_{p,r}\sin^2\beta\cos^2\beta\cos\delta_r$
Reflection Leakage $RL(\alpha,\beta)$	$\frac{1}{2}(m^t_{11}+m^r_{12})$	$\frac{1}{2}(\rho^2_{s,r}\cos^2\beta+\rho^2_{p,r}\sin^2\beta)$
Reflection couplance $RC(\alpha,\beta)$	$\frac{1}{2}(m^r_{11}-m^r_{12}+m^r_{21}-m^r_{22})$	$\sin^2\beta\cos^2\beta(\rho^2_{s,r}+\rho^2_{p,r}-2\rho_{s,r}\rho_{p,r}\cos\delta_r)$

Table 1: Measured Mueller matrix elements and theoretical values of angular performance parameters of polarizing beam splitters. $\rho(\alpha(0,\phi),\lambda)$ is the real amplitude transmission or reflection coefficient. Subscripts p and s refer to p polarization and s polarization respectively. Superscripts t and r denote transmission and reflection. δ_t and δ_r are the retardance in transmission and reflection respectively. $\alpha(l,m,n)$ is the angle of incidence a ray makes with the beamsplitting interface and $\beta(l,m,n)$ is the orientation of s-p coordinates relative to $\hat{h}-\hat{v}$ coordinates. The functional dependence of $\alpha(l,m,n)$ and $\beta(l,m,n)$ are given in appendix A.

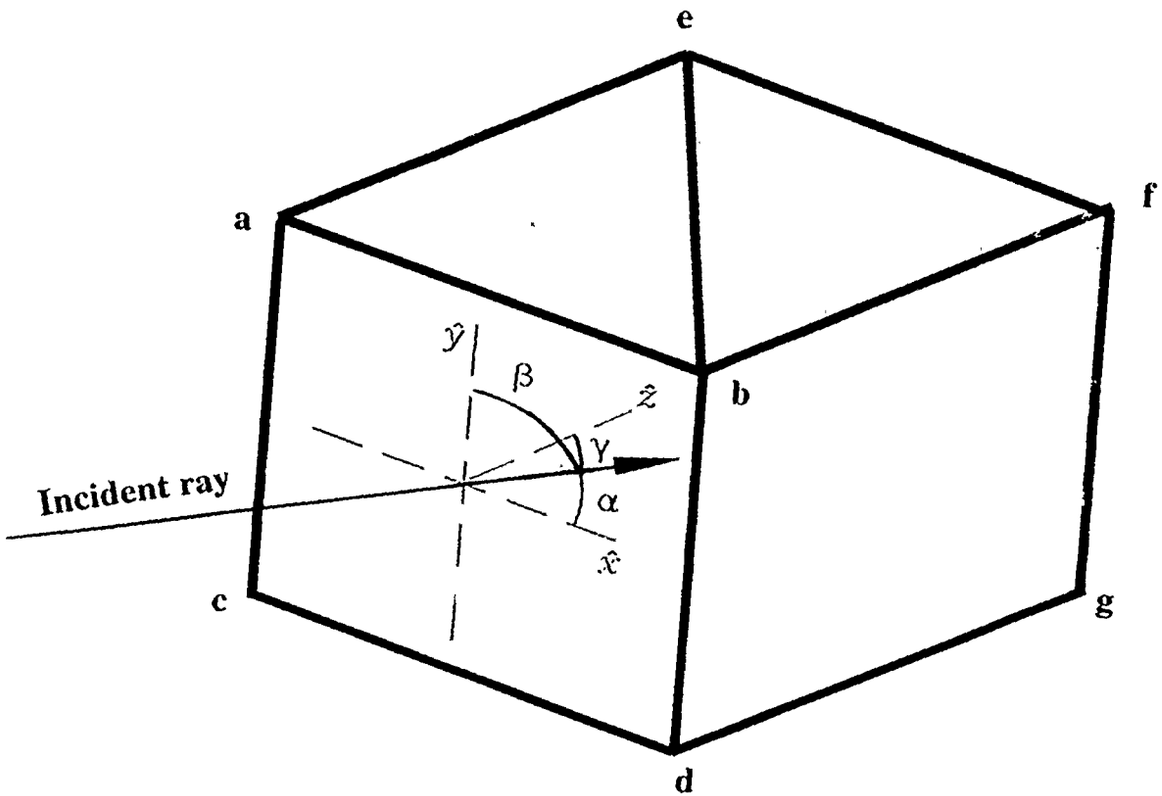

Figure 1

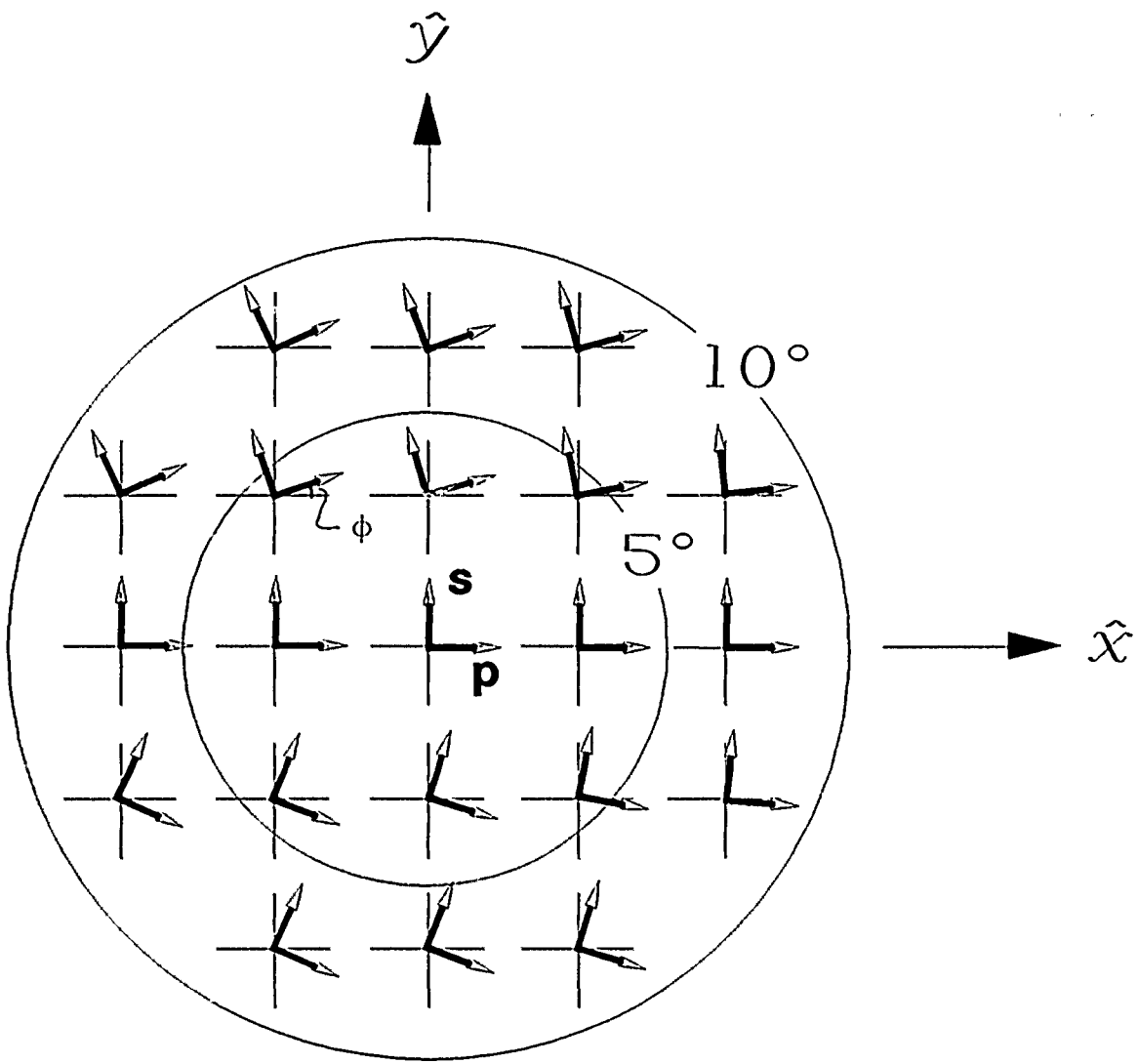

Figure 2

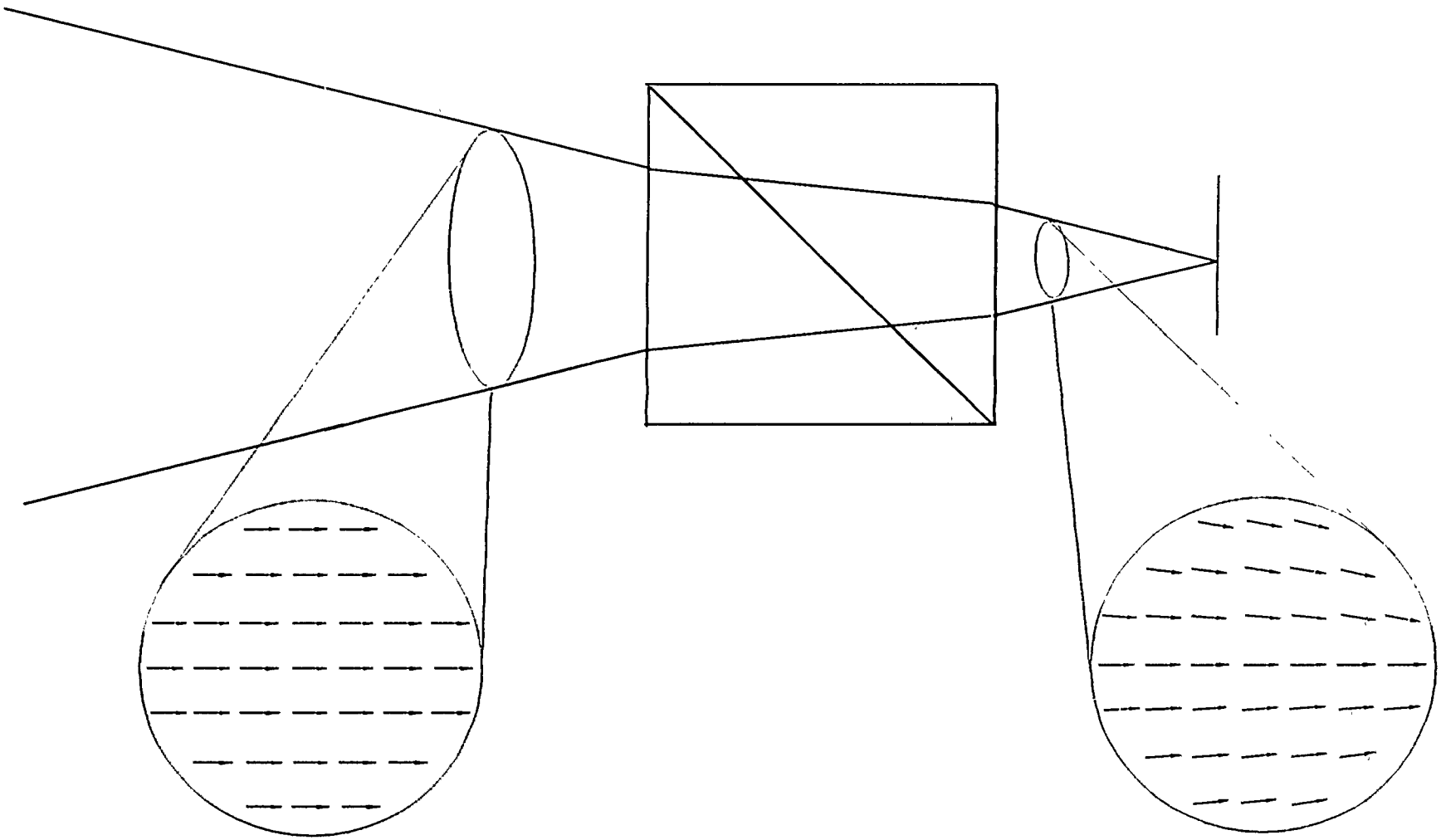

Figure 3

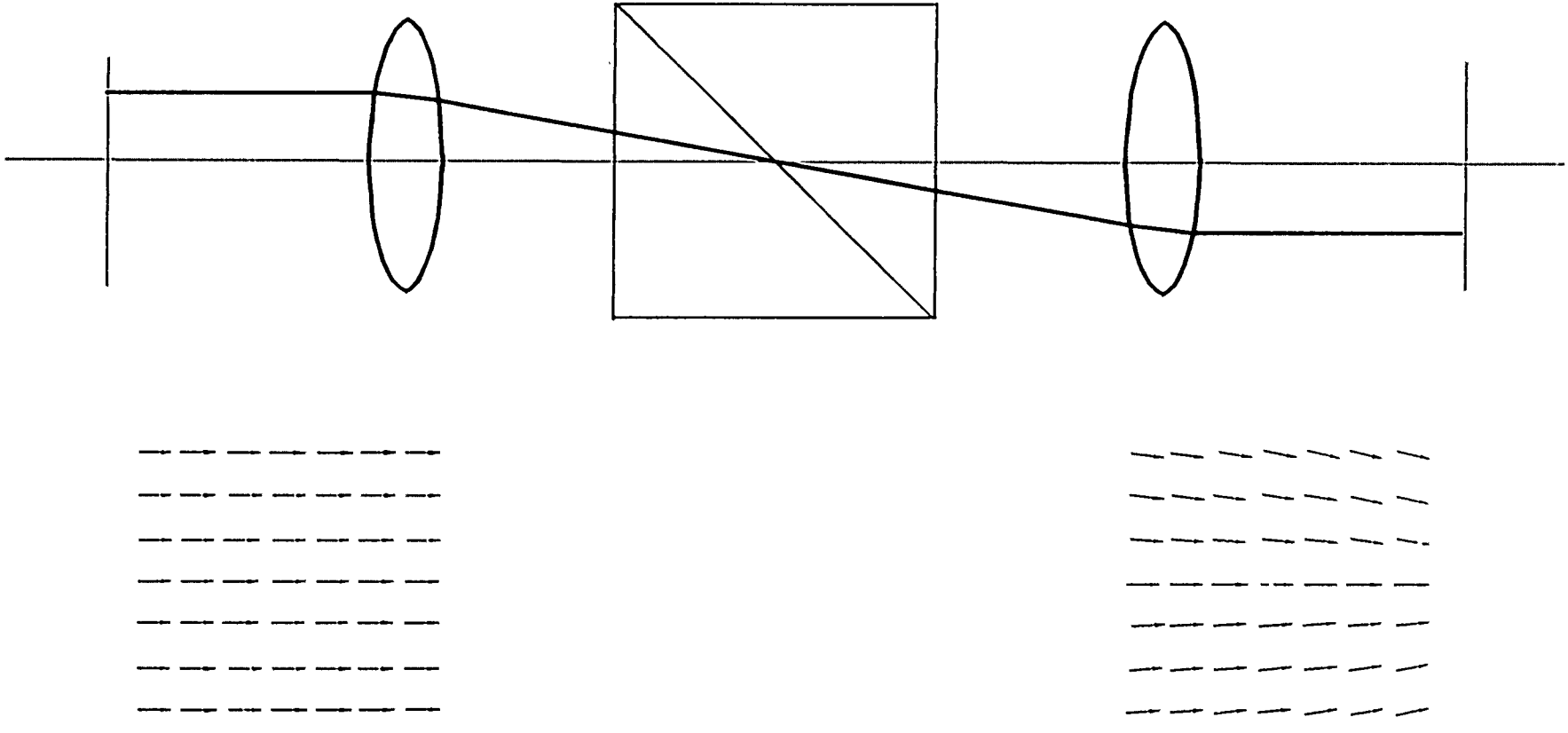

Figure 4

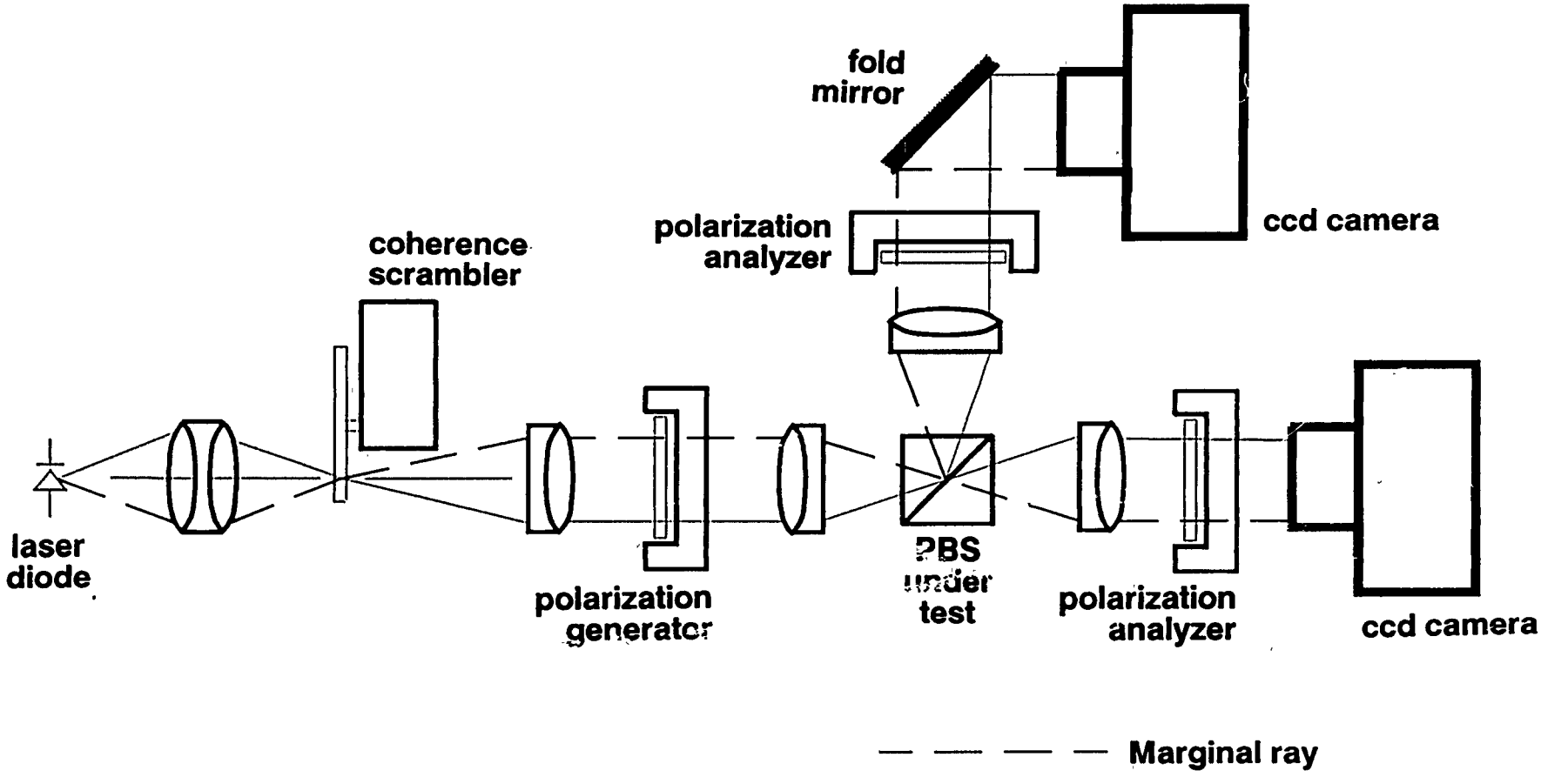
fold
mirror
ccd camera
polarization
analyzer
coherence
scrambler
laser
diode
polarization
generator
PBS
under
test
polarization
analyzer
ccd camera
Marginal ray

Figure 5

MELLES GRIOT 830 nm Polarizing Beam Splitter

Figure 6

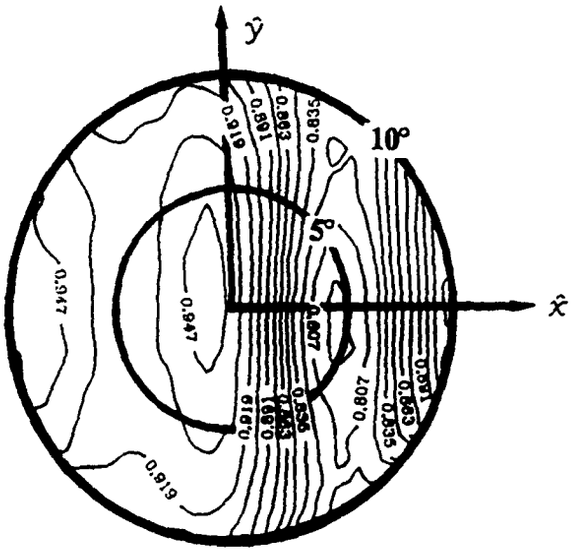

Transmission efficiency ($\hat{h} \rightarrow \hat{h}$)

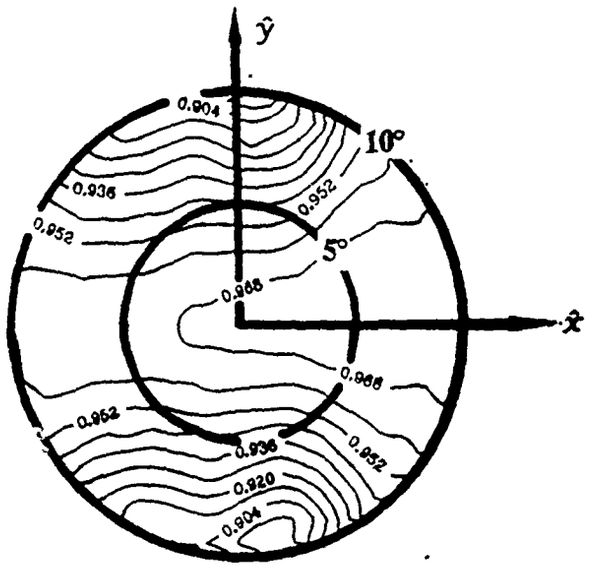

Reflection efficiency ($\hat{v} \rightarrow \hat{v}$)

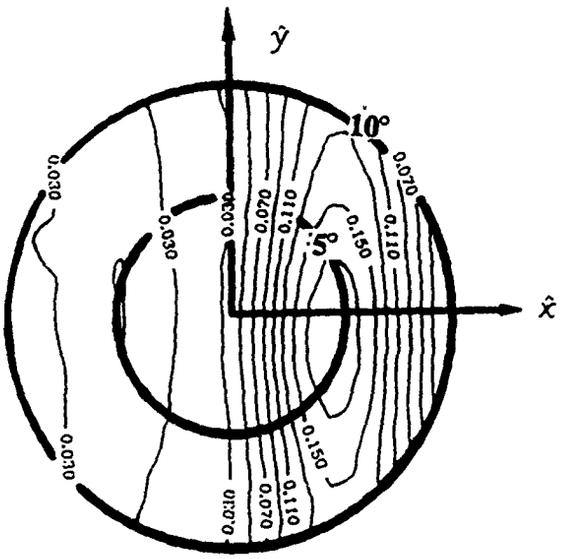

Reflection leakage ($\hat{h} \rightarrow \hat{h} + \hat{v}$)

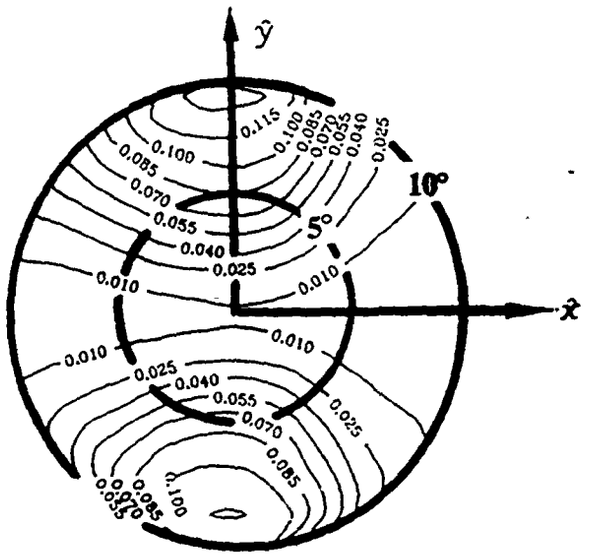

Transmission leakage ($\hat{v} \rightarrow \hat{v} + \hat{h}$)

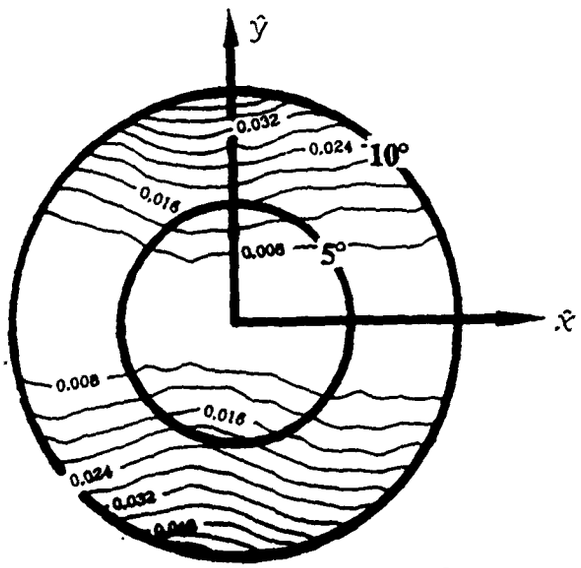

Transmission couplance ($\hat{h} \rightarrow \hat{v}$)

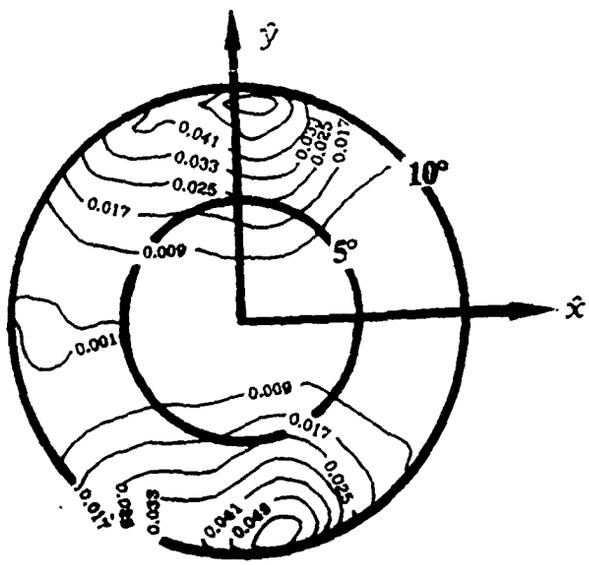

Reflection couplance ($\hat{v} \rightarrow \hat{h}$)

CVI Polarizing Beam Splitter

Figure 7

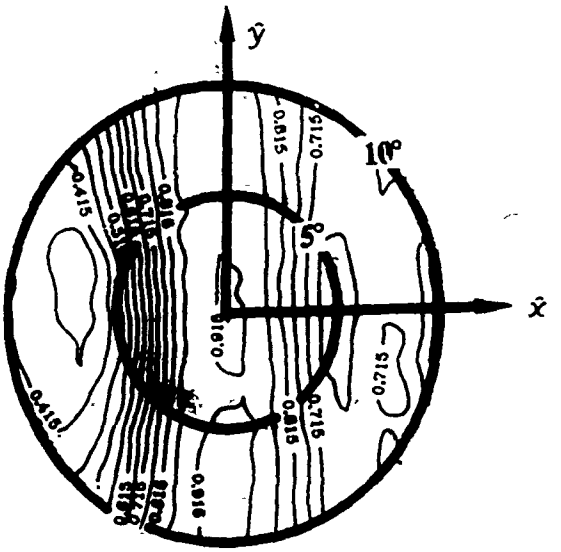

Transmission efficiency ($\hat{h} \rightarrow \hat{h}$)

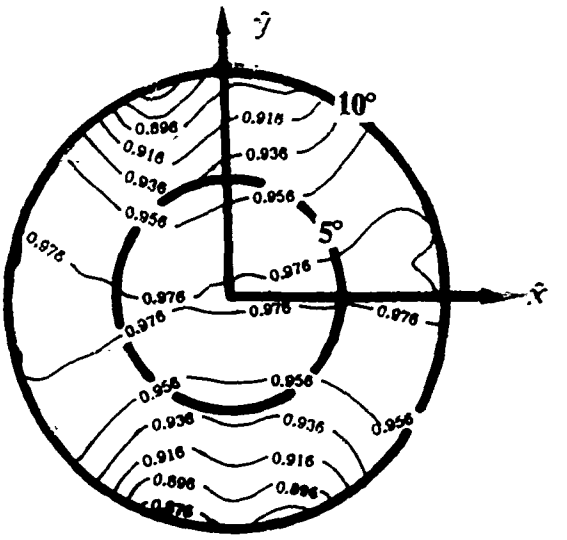

Reflection efficiency ($\hat{v} \rightarrow \hat{v}$)

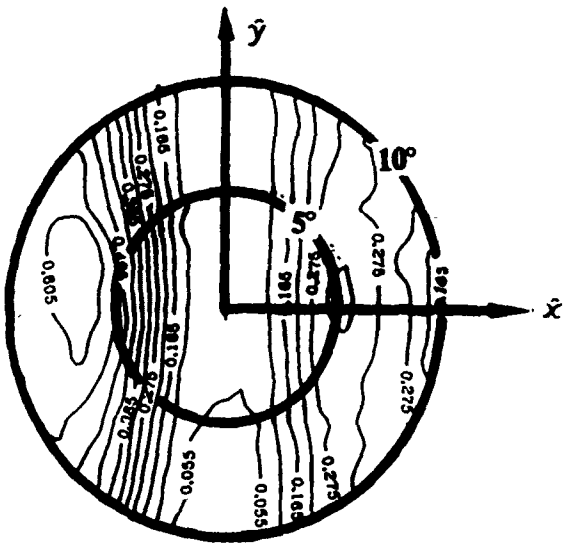

Reflection leakage ($\hat{h} \rightarrow \hat{h} + \hat{v}$)

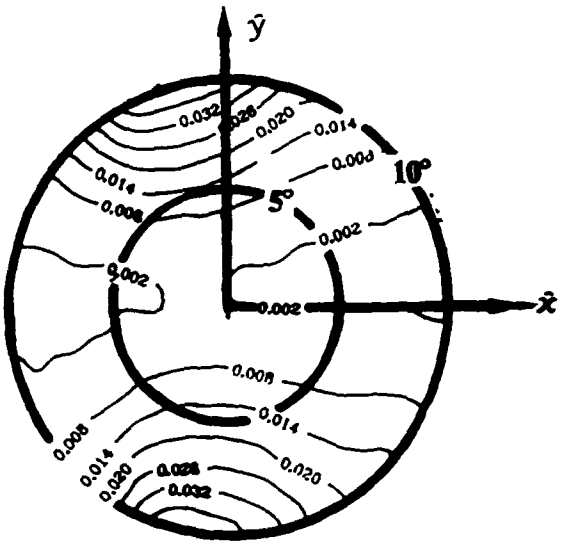

Transmission leakage ($\hat{v} \rightarrow \hat{v} + \hat{h}$)

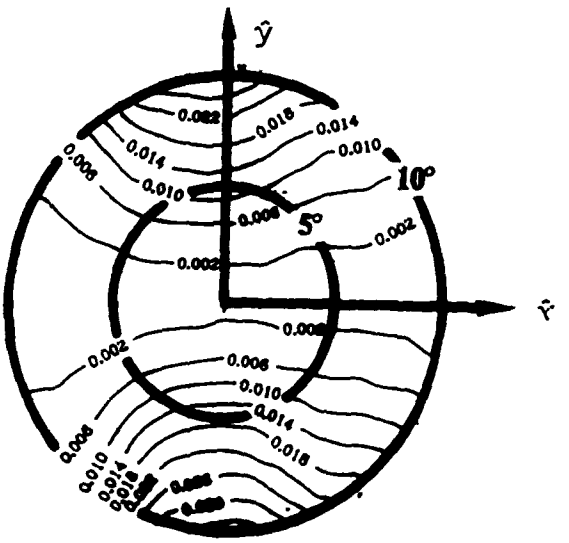

Transmission couplance ($\hat{h} \rightarrow \hat{v}$)

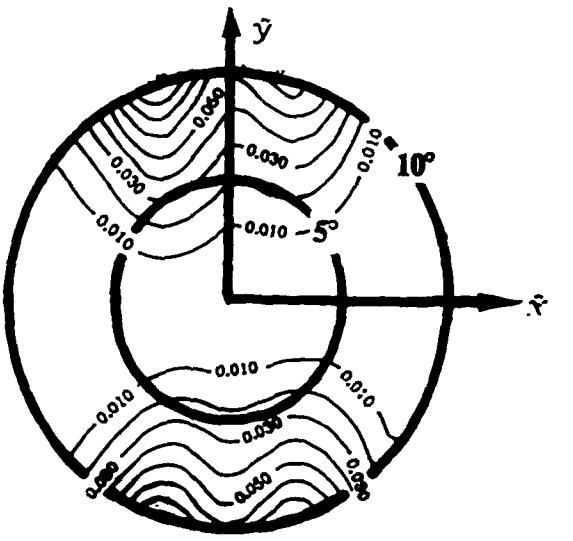

Reflection couplance ($\hat{v} \rightarrow \hat{h}$)

Newport Polarizing Beam Splitter

Figure 8

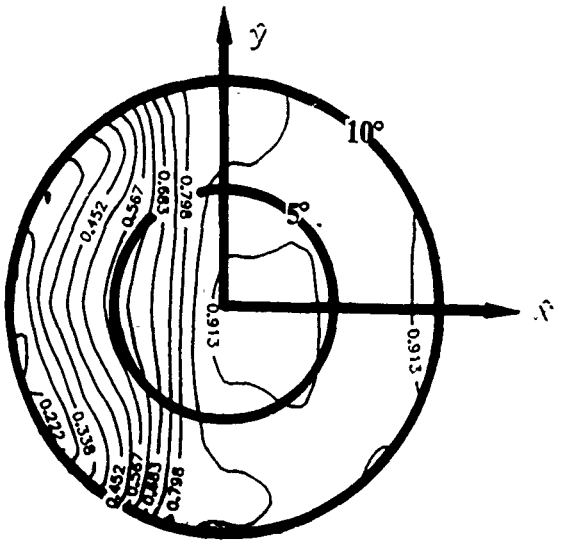

Transmission efficiency ($\hat{h} \rightarrow \hat{h}$)

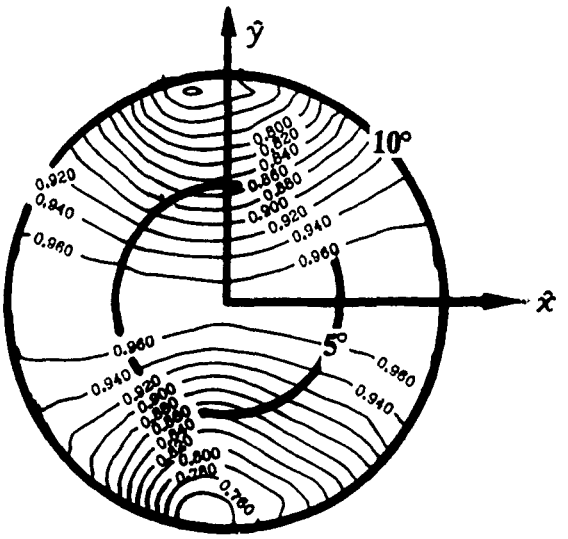

Reflection efficiency ($\hat{v} \rightarrow \hat{v}$)

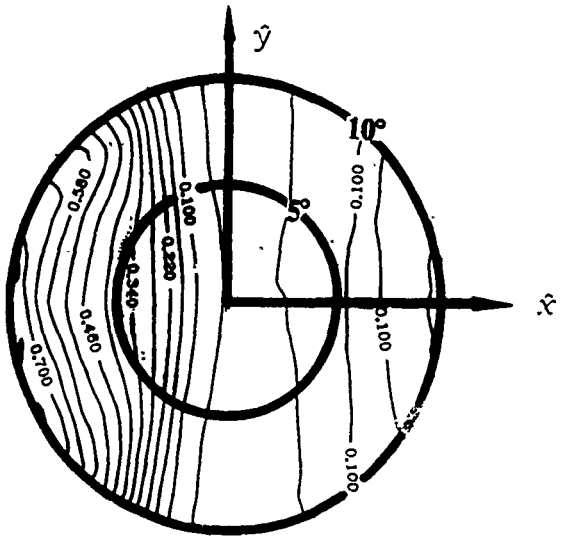

Reflection leakage ($\hat{h} \rightarrow \hat{h} + \hat{v}$)

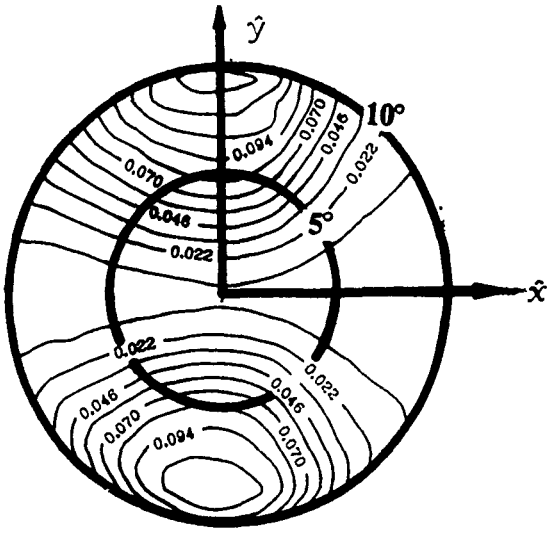

Transmission leakage ($\hat{v} \rightarrow \hat{v} + \hat{h}$)

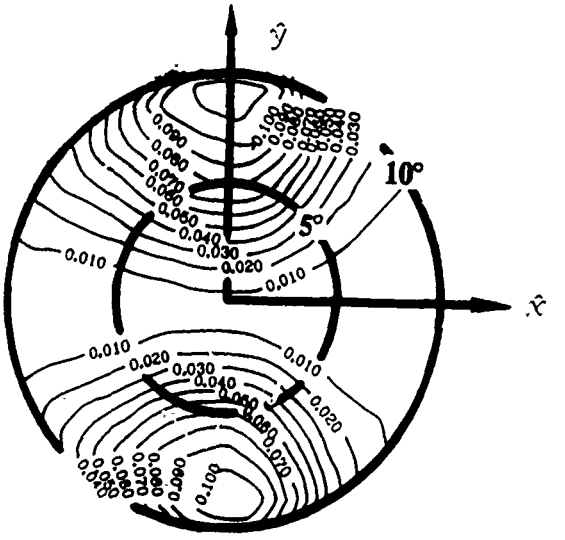

Transmission couplance ($\hat{h} \rightarrow \hat{v}$)

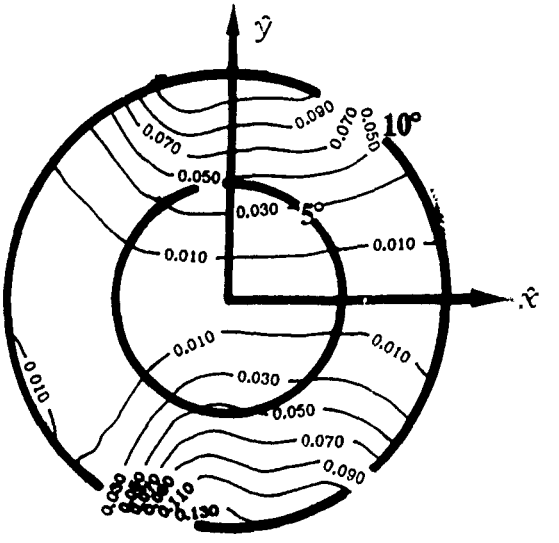

Reflection couplance ($\hat{v} \rightarrow \hat{h}$)

AT&T Polarizing Beam Splitter

Figure 9

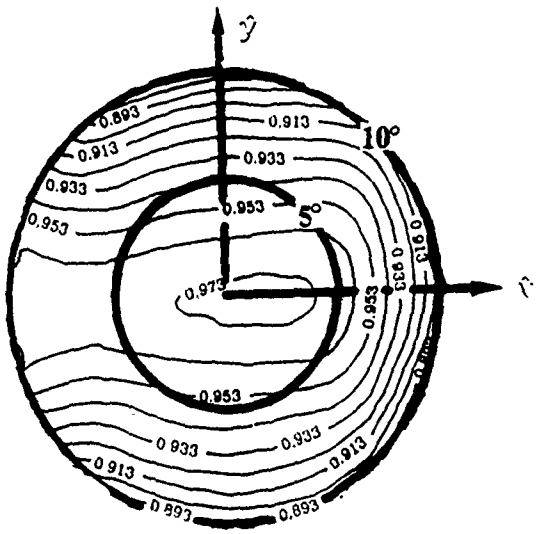

Transmission efficiency ($\hat{h} \rightarrow \hat{h}$)

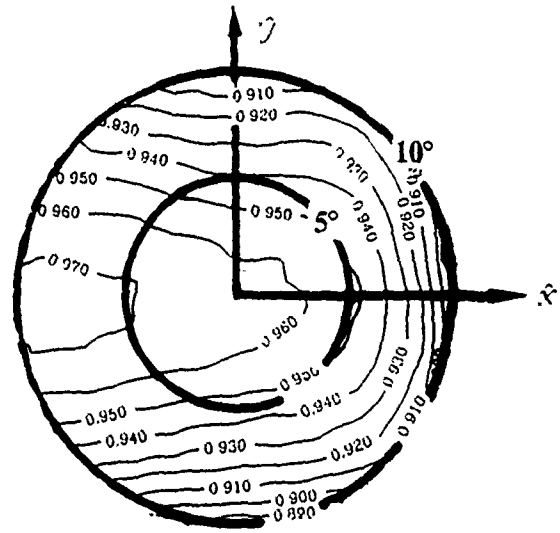

Reflection efficiency ($\hat{v} \rightarrow \hat{v}$)

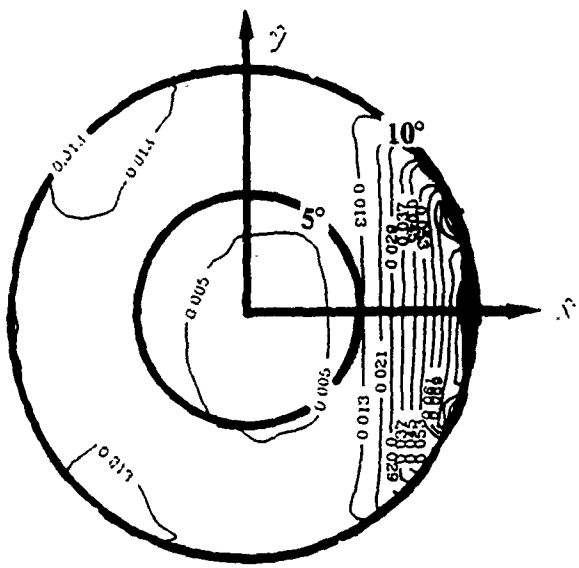

Reflection leakage ($\hat{h} \rightarrow \hat{h} + \hat{v}$)

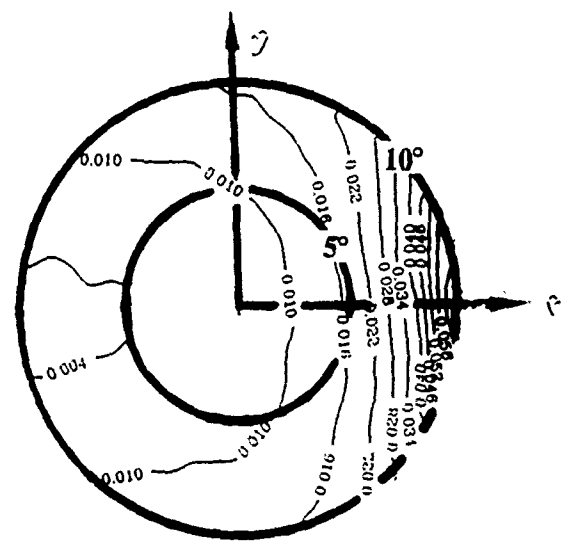

Transmission leakage ($\hat{v} \rightarrow \hat{v} + \hat{h}$)

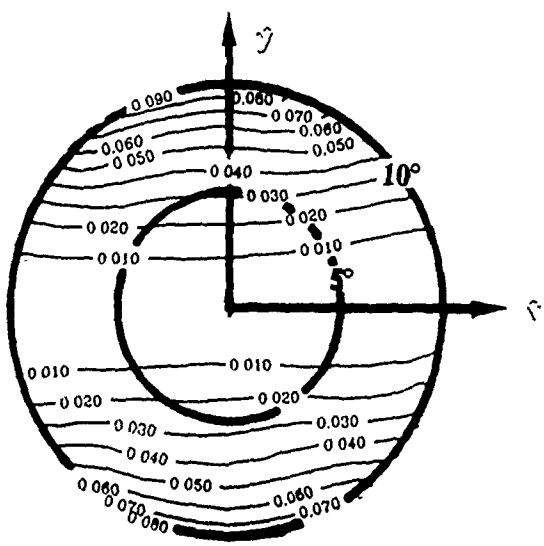

Transmission couplance ($\hat{h} \rightarrow \hat{v}$)

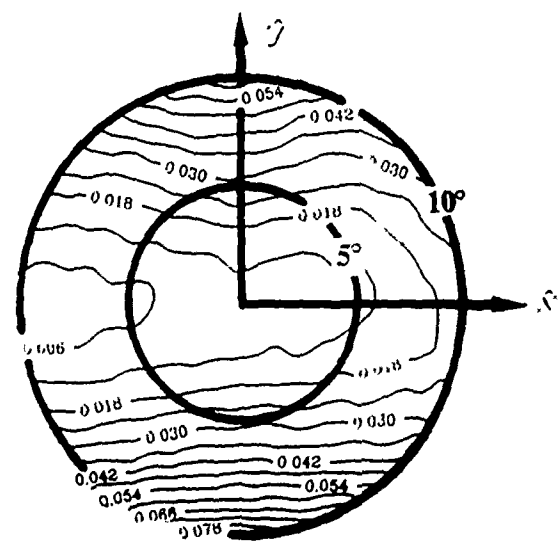

Reflection couplance ($\hat{v} \rightarrow \hat{h}$)